Faculty of Mathematics and Physics
Charles University in Prague

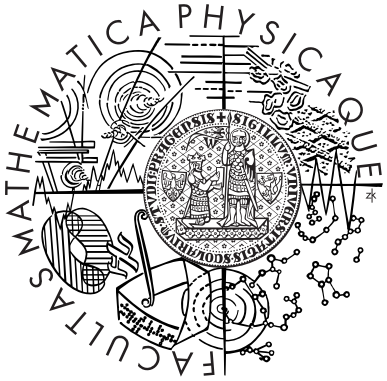

Multi-dimensional radiative transfer in quiescent prominences

RNDr. Stanislav Gunár

Doctoral Thesis

September 2007

Contents

Preface

I dedicate this work
to my parents, to Yarka
and to all of my friends.

This thesis represents an overview of my research work during three and a half year of my doctoral studies at the Faculty of Mathematics and Physics of the Charles University in Prague. The research work was carried out at the Astronomical Institute of the Academy of Sciences of the Czech Republic in Ondřejov under the leadership of Ass. Prof. Petr Heinzel DSc. He posses my sincere thanks for his fine guidance through the deep waters of the radiative transfer, for a plenty of valuable advices he addressed me and for his friendship.
My many thanks belongs also to U. Anzer from the Max-Planck-Institut für Astrophysik in Garching for his leadership, help and endless discussions during my EARA-EST fellowship periods at this institute. I thank B. Schmieder from the Observatiore de Paris, Section de Meudon for her valuable help and advices during our collaboration and hospitality during my stays in Paris. I thank also U. Schühle and L. Teriaca for their help during our collaboration. I thank MEDOC center for observations and B. Schmieder, P. Schwartz, U. Schühle and L. Teriaca for SUMER data reduction.

The research work presented within this thesis was supported by grant No. IAA 3003203 and grant 205/07/1100 of the Grant Agency of the Academy of Sciences of the Czech Republic, ESA PECS project No. 98030 and the research project AVOZ10030501. This work was done in the framework of the EARA-EST programme and the RTN programme (European Solar Magnetism Network, Contract No. HPRN-CT-2002-00313)

I. Introduction

This chapter provides an insight into the physical and spectroscopic properties of the prominence fine structures.

The most frequently used definition of a solar prominence refers to an object extending outwards from the solar surface into the solar corona, which is considerably denser and cooler than the surrounding coronal plasma.
The solar prominences are divided into two main categories: *quiescent prominences* and *active prominences*. Active prominences are usually short-living (hours, days), dynamical features typically occurring above the active regions. In contrast, quiescent prominences are relatively stable features laying mostly outside active regions. Their life-times range from a few days up to several months. The prominences are usually observed above the solar limb, when seen in the projection on the solar disk they are referred to as filaments.
Solar prominences were among the first observed features of the solar atmosphere. Their study has began with invention of the spectrohelioscope in 19^{th} century (Mouradian & Garcia 2007). Although the prominences have been since then a subject of frequent observations and studies, they continuously attract a considerable attention of solar physicists. With the help of new ground-based and space-born observatories we can now resolve the prominence structures on spacial scales reaching down to about hundred km.
This thesis is dedicated to the study of quiescent prominences. Therefore in the following text we refer to the quiescent prominences simply as to prominences.

1.1 Prominence fine structures

Already drawings by Secchi (1877) (one can be found in the textbook of Tandberg-Hanssen (1995)) show that the prominences are not compact objects but consist of many small-scale structures with seemingly random layout. The prominence fine structures have been frequently observed with an increasing resolution. The most recent high-resolution ground-based observations (with instruments like the new SST (*Swedish Solar Telescope* - Scharmer et al. 2003) and DOT (*Dutch Open Telescope* - Rutten et al. 2004)) reveal adetailed morphology of the fine

Figure 1.1: BBSO H-α image of a typical quiescent prominence. The prominence fine structures are well visible with a number of quasi-vertical threads (from Low & Petrie 2005).

structures and their dynamical behavior (in contrast, the large-scale segments of the prominences are rather stable). Similar fine structures are now observed with a comparable resolution also by the *Solar Optical Telescope* (SOT - Suematsu et al. 2007, Tarbell et al. 2007) onboard the Hinode satellite (*Japan Aerospace Exploration Agency* (JAXA) mission with United States and United Kingdom collaboration - see http://solar-b.nao.ac.jp).
The prominence fine structures usually consist of many vertically-oriented threads and knots of cool plasma which are typically a few hundreds km wide. Examples of such small-scale structures with many vertical threads are shown in Figs. 1.1 and 1.2 obtained by the BBSO (*Big Bear Solar Observatory*) and Hinode/SOT. On a larger scale, one can identify a few vertical plasma sheets which, using a lower spatial resolution, would appear as more-or-less homogeneous vertical slabs. Such low-resolution images led modelers to use a vertical 1D slab approximation to a real prominence geometry which neglected the fine-structure nature of the prominences.
Prominence fine structures manifest themselves rather differently in case of the limb observations and in case of disk filaments. Filaments and prominences repre-

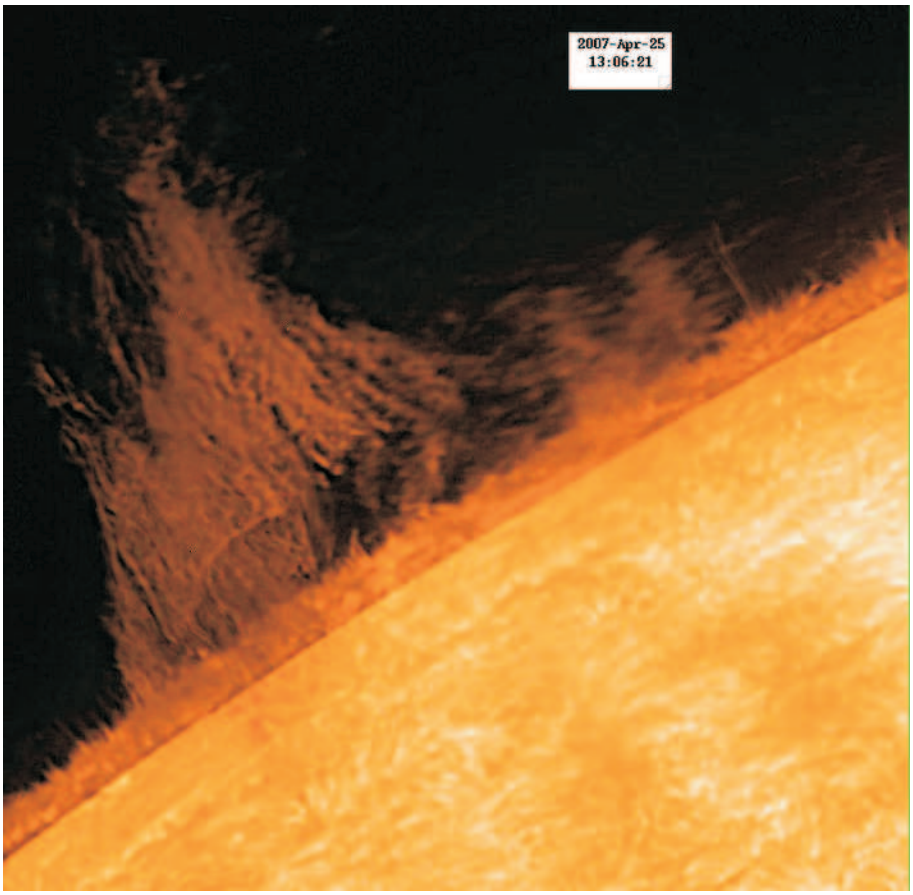

Figure 1.2: Hinode/SOT image of a quiescent prominence obtained in the H-α line centre.

sent the same solar features but seen in different projections. Generally speaking, a prominence seen in emission on limb will appear later or has appeared before as a dark filament in absorbtion on the disk. The filament fine structures usually consist of horizontal thread-like features with different lengths called *fibrils* (see Fig. 1.3 and Engvlod 2004). Thinnest visible fibrils have thicknesses down to the resolution limit of SST or DOT (less than 100 km). Very thin fibrils visible along the spine of the filament are rather short and inclined to the filament axis due to a shear of the magnetic field lines. On the other hand, much longer fibrils can be seen within the barbs or connecting various parts of the filament main body. The fact that densely packed fibrils seen along the spine are rather short compared to a large-scale magnetic arcade in which the prominence/filament sits indicates that these fibrils are the locations of the cool plasma condensations in a dipped magnetic field (Heinzel 2007).

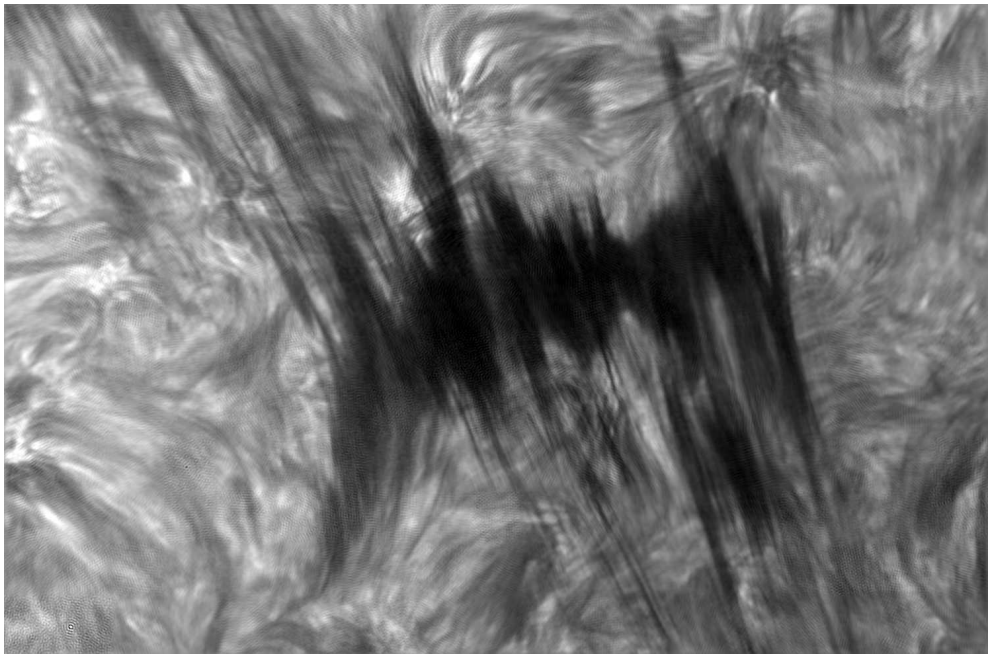

Figure 1.3: High-resolution SST image of a disk filament. Well defined fine structures have the shape of horizontal dark fibrils (courtesy of O. Engvold).

1.2 Physical attributes of the prominence fine structures

The prominence fine structures represent cool plasma condensations located inside the hot solar corona. The prominence plasma contains roughly 90% of hydrogen. Typical temperatures within the central coolest parts of the fine structures are about 6000 to 8500 K (some authors give a lower limit as low as 4300 K - Hirayama 1979). The hydrogen is partially ionized in the central parts of the prominences. The boundary parts of the fine structures seem to exhibit rather rapid rise of the temperature up to coronal values exceeding one million degrees. With such temperatures the hydrogen becomes fully ionized. This boundary region is called the *Prominence-Corona Transition Region* (PCTR). The plasma density in the central cool parts is about two orders of magnitude larger than the coronal density. Thus the presence of the magnetic field is crucial for the support of the dense prominence plasma against the solar gravity. The coronal magnetic field penetrates the whole prominence and keeps it in a quasi-static state. The intensity of the magnetic field within quiescent prominences, according to current determinations, is not very large, ranging from a few Gauss to a few tens of Gauss (Lopez-Ariste & Aulanier 2007). The magnetic fields in active prominences are typically stronger, reaching from tens of Gauss up to a hundred Gauss. Characteristic conditions prevailing in quiescent prominences are summarized in the

	Prominence		PCTR
	Centre	Boundaries	
T_e(K)	4 300 - 8 500	8 000 - 12 000	$10^4 - 10^6$
v_{turb}(km s^{-1})	3 - 8	10 - 20	30
n_e(cm^{-3})	$10^{10} - 10^{11}$	$10^{9,6}$	$10^8 - 3.10^{10}$
p_g(dyn cm^{-2})	0.1 - 1	~ 0.02	~ 0.2
B(gauss)	4 - 20		

Table 1.1: Hvar reference atmosphere of quiescent prominences (Engvold et al. 1990). Here T_e represents the electron temperature, v_{turb} is the turbulent velocity, n_e represents the electron density, p_g is the gas pressure and B is the intensity of the magnetic field.

so-called '*Hvar Reference Atmosphere of the Quiescent Prominences*' (Engvold et al. 1990, see Table 1.1).
Typical lengths of the prominence fine structures are about 5000 to 10 000 km in case of the vertical threads and about 5000 to 20 000 km for horizontal fibrils. The thickness of the prominence/filament fine structures is from 1000 km down to a hundred km or even lower. For a more general description of the prominence physics see the monograph of Tandberg-Hanssen (1995). The prominence fine structures were recently reviewed by Heinzel (2007).

1.3 Spectroscopic attributes of the prominence fine structures

With the use of space-born instruments it is possible to observe the prominence fine structures not only in the visible light, but also at ultraviolet (UV - above 1000 Å) and extreme-ultraviolet (EUV - bellow 1000 Å) wavelengths. The UV and EUV observations provide us with a useful tool for the prominence diagnostics. Among the space instruments the SOHO (*SOlar and Heliospheric Observatory* -

the joint space mission of ESA and NASA: Fleck et al. 1995) was frequently used to observe solar prominences and filaments in UV and EUV spectral bands. The SUMER UV-spectrograph (*Solar Ultraviolet Measurements of Emitted Radiation* - Wilhelm et al. 1995) onboard SOHO posses a unique ability to observe all lines of the hydrogen Lyman series and the Lyman continuum. The observations in the hydrogen Lyman lines and continuum represent an important contribution to the understanding of the structure and physical properties of prominence fine structures. The formation depths of the Lyman lines and their individual parts (line centre, peaks and wings) span the whole structure of the prominence from the centre to the PCTR. Thus such observations provide significant constraints for prominence fine-structure modelling. The use of SUMER for the prominence physics was reviewed by Patsourakos & Vial (2002), the prominence spectroscopy with SUMER was also summarized by Heinzel et al. (2006).

The spectral diagnostics of the prominence fine structures represents a complex problem for a number of reasons. First, prominence fine-structure elements represent rather complicated features from the spectroscopic point of view. They can be optically thick in some wavelengths and thin in others, even within one spectral line (thick in the line core and thin in the wings). In case of the optically thick structures, we can see only the first fine-structure element. However, in case of the optically thin structures, several elements are seen along the line-of-sight and their radiation output is integrated. This situation largely complicates the analysis of the observed spectra because it becomes rather difficult to identify the places of formation of various spectral lines. Second, although the large-scale prominence structures are relatively stable, the fine structures are highly dynamical. Therefore, any multi-wavelength spectroscopic observations have to be carried out simultaneously or at least quasi-simultaneously (i.e. within the time shorter than a typical time of the considerable changes of the fine structures). Another complication arises from the fact that the internal structure of the fine-structure elements is not uniform. The shape of the PCTR depends on the orientation of the magnetic field lines with respect to the line-of-sight due to principally different thermal conductivity along and across the field lines. Therefore, during observations the line-of-sight is passing through different parts of the PCTR in dependence on the magnetic field orientation with respect to the line-of-sight.

The proper analysis of the prominence fine-structure spectral observations requires highly sophisticated numerical models with an adequate theory of the plasma in the magnetic field and complex non-LTE radiative-transfer computations. Because of the complicated spectroscopic nature of the prominence fine structures one should not constrain the fine-structure modelling only to one particular element but rather consider an ensemble of several prominence fine structures.

1.4 Principal aims of the thesis

This thesis is dedicated to the investigation of the multi-dimensional radiative transfer in the prominence fine structures. For this purpose we employ both, the theoretical modelling of the prominence fine structures based on 2D models of Heinzel & Anzer (2001), and the spectroscopic analysis of the observed prominences in order to derive the physical parameters of the prominence fine structures.

The principal aims of the thesis are the following:

- Construction of a 2D prominence fine structure model, on the basis of the 2D models of Heinzel & Anzer (2001), capable to properly reproduce the observed prominence spectrum
- Construction of a grid of 2D models for the study of the model properties and the dependence of the synthetic spectrum on given input parameters
- Construction of multi-thread fine-structure models
- Study of the formation of the Lyman lines and the Lyman continuum in the prominence fine structures
- Spectroscopic analysis of the Lyman lines and the Lyman continuum observed by SOHO/SUMER by detailed fitting of the observed spectra with the synthetic one.
- Analysis of the orientation of the magnetic field in a round-shaped filament observed by SOHO and ground-based observatories.

The results of this thesis were published in the international journals and the conference proceedings. Five of these publications with the most significant results represent a core of the thesis. In the following chapters we present a supplementary text necessary to the understanding of the thesis topic and the summaries of the publications. The publications themselves are included as appendixes A to E.
The thesis is organized as follows. A brief introduction to the prominence observations by SOHO is given in Chapter II. The description of the prominence MHS models is given in Chapter III. Chapter IV. describes the principles of the radiative transfer theory and corresponding numerical methods used for the non-LTE prominence modelling. The summaries of the published results of the thesis are given in Chapter V., in five sections corresponding to the five publications. Chapter VI. presents the conclusions, summarizes the work in progress and gives an overview of the future research plans.

II. SOHO prominence observations

This chapter provides an information about the space-born data used in the thesis.

SOHO, the SOlar and Heliospheric Observatory, is a project of the international cooperation between ESA (*European Space Agency*) and NASA (*National Aeronautics and Space Administration*). It is dedicated to study of the Sun from its deep core to the outer corona and the solar wind. The scientific payload of SOHO consists of twelve state-of-the-art instruments (Fleck et al. 1995): three helioseismology instruments, five instruments for the study of the outer solar atmosphere and corona and finally three experiments for the measurements of the solar wind.
The SOHO spacecraft was launched from the Kennedy Space Center on August 1, 1995 and it is placed in a halo orbit around the Sun-Earth L1 Lagrangian point where it can continuously observe the Sun.

The observational data on prominences and filaments collected by SOHO during more then a decade of the observations represent a major breakthrough in the understanding of the prominence physics. Four scientific instruments onboard SOHO are useful for the study of the solar prominences: SUMER (*Solar Ultraviolet Measurements of Emitted Radiation*) UV and EUV-spectrograph, CDS (*Coronal Diagnostic Spectrometer*) EUV-spectrometer, EIT (*Extreme-ultraviolet Imaging Telescope*) EUV-telescope and MDI (*Michelson Doppler Imager*) providing the magnetograms and the velocity maps. The data sets obtained by these instruments are the most comprehensive data regarding the prominences observed from space. Moreover LASCO (*Large Angle and Spectrometric COronagraph experiment*) provides the white-light coronographic images of related coronal structures and CME's (*Coronal Mass Ejections*).

The SUMER instrument (Wilhelm et al. 1995) is devoted to study of structures and processes occurring from the chromosphere through the transition region to the inner solar corona over a temperature range from less than 10^4 to 2×10^6 K.
SUMER is capable of measuring the profiles and intensities of the UV (above

1000 Å) and EUV (bellow 1000 Å) spectral lines within a broad wavelength range from less than 500 to 1610 Å. Spectral observations of the Sun with short exposure times in UV and EUV spectrum allow us to study essential physical parameters of the solar atmosphere such as the plasma density and temperature, abundances of species, velocity fields, topologies of the plasma structures and their evolution. SUMER is equipped with two photon-counting detectors (A and B). Both detectors have 1024 spectral columns and 360 spatial rows.

The CDS instrument (Harrison et al. 1995) was designed to investigate the structures of the solar atmosphere and their evolution through the detection of the spectral lines within the EUV wavelength range between 150 and 800 Å with high temporal, spatial and spectral resolution. The full wavelength range of CDS cannot be viewed simultaneously. Therefore, the CDS observations are restricted to the selection of the prime emission lines within the given wavelength range.

The EIT EUV-telescope (Delaboudiniére et al. 1995) provides the full-disk images of the transition region and the inner solar corona up to 1.5 solar radius above the solar limb. The selection of four emission lines He II (304 Å), Fe IX (171 Å), Fe XII (195 Å) and Fe XV (284 Å) spans the solar atmosphere from the transition region to the inner corona and thus provides sensitive temperature diagnostics in the temperature range from 6×10^4 K to 3×10^6 K. EIT has 45×45 arcmin field of view with approximately 5-arcsec spatial resolution. The full disk images obtained by EIT provide the connection between the structures observed on the disk and those seen above the limb. Time series of images observed simultaneously with SUMER and CDS, which have limited fields of view, help to define the global dynamics of these structures.

The MDI instrument is used by the SOI experiment (*Solar Oscillations Investigation* - Scherrer et al. 1995) for the studying the solar oscillations. The MDI is also used for photospheric observations of the solar magnetic fields and the surface motions. The instrument images the Sun on a 1024×1024 CCD camera through a series of increasingly narrow spectral filters.

SOHO represents an extremely successful and durable mission. It was originally designed for a nominal lifetime of two years. In 1997 the mission was extended until 2003 because of its spectacular success. In 2002, a second extension to another four years was granted which allowed SOHO to cover a complete 11-year solar cycle. Now, at the end of 2007, SOHO is still operational and the mission is extended up to 2010.
The most critical moments of the SOHO mission occurred on June 25, 1998, when the communication with the spacecraft was lost due to a system failure

and SOHO kept orbiting the L1 Sun-Earth Lagrangian point in an emergency mode while teams of scientists and engineers on the ground were working on its recovery (for the full account of the SOHO recovery see Vandenbussche 2006). Only after three months of the work and preparations SOHO was finally brought back to normal operating mode on Sept. 25, 1998. Two of the three gyroscopes have failed during the breakdown of the spacecraft but all of the twelve scientific instruments were brought back to the operational state. However, on Dec. 21, 1998 the last onboard gyroscope failed. After that, new on-board software that no longer relies on gyroscopes was installed in Feb. 1999 which made SOHO the first three-axis stabilized spacecraft operated without gyroscopes.
The scientific results obtained with SOHO were summariezed during the SOHO-17 Workshop which celebrated 10 years by the SOHO mission (ESA SP-617, 2006).

2.1 Observational data used within the thesis

The SUMER spectrograph represents the SOHO instrument with a large impact on our understanding of the prominence fine structures. During a decade of observations SUMER collected a considerable amount of the spectroscopic data on prominences. A review of the impact of the SUMER observations on the physics of the solar prominences and their fine structures is given by Patsourakos & Vial (2002). The spectroscopic analyses of prominences using the SUMER observations were summarized by Heinzel et al. (2006).
A unique ability of SUMER to observe the whole hydrogen Lyman line series and the Lyman continuum represents an important constraint on the modelling of the prominence fine structures. The Lyman lines and continuum formation depths span the whole body of the prominence fine structure from its centre to the PCTR (Heinzel et al. 2005, Gunár et al. 2007a). Thus the Lyman lines and continuum observations represent a useful diagnostic tool for the spectroscopic analysis of the prominence fine structures. Some of the Lyman series spectral data and their analysis can be found in Schmieder et al. (1998, 1999a, 2003, 2007). Parenti et al. (2004, 2005) produced an atlas of the prominence UV and EUV spectrum observed by SUMER. Heinzel et al. (2001) published the Lyman line data for three different prominences. However, the Lyman-α line was observed using the attenuator and thus its profile is significantly distorted.
In recent years the SUMER spectrograph have obtained several observations of the Lyman-α line outside the attenuator. These observations are very unique because the previous Lyman-α data obtained by e.g. OSO-8 exhibit an additional absorbtion in the centre of the line due to the presence of the geocorona (Vial 1982a, Schmieder et al. 1999b). Lyman-α observed directly, without the attenuator, can damage the SUMER detectors because of its extreme intensity. However, due to the progressive deterioration of the detector A direct Lyman-α

observations were allowed. Such observations represent a considerable constraint on the prominence fine structure modelling because the Lyman-α line is optically thick and therefore the Lyman-α profiles are not affected by the multi-thread nature of the prominence fine structures. This was shown by Gunár et al. (2007b) who analyzed the set of the Lyman lines from the Lyman-α to the Lyman-7 line observed by SUMER on May 25, 2005, during the MEDOC coordinated campaign between the SOHO and the ground-based instruments (MEDOC campaign No. 15, May 16 to 29, 2005). Another set of the direct Lyman-α observations used within this thesis is represented by the Lyman-α 85" $\times$ 50" raster obtained by SUMER on Apr. 18, 2005. The spectroscopic analysis of this Lyman-α raster was performed by Gunár et al. (2006).

A considerable number of the prominence observations by SUMER was obtained within the *Joint Observing Programmes* (JOP) between various SOHO instruments and other space-born (e.g. TRACE, Hinode) and ground-based (e.g. THEMIS, SST, DOT, Ondřejov) observatories (see http:// sohowww.nascom.nasa.gov/soc/JOPs). A number of JOP observations was coordinated from the *Multi Experiment Data and Operation Centre* (MEDOC) at the IAS (*Institut d'Astrophysique Spatiale*) in Orsay, France (http://www.ias.u-psud.fr/medoc), where S. Gunár has also participated.

III. Prominence modelling

The chapter describes the prominence modelling from the 1D slab models to the 2D models of prominence fine structures.

Although the existence of the prominence fine structures was already known, prominences were modeled for decades as one-dimensional vertically standing slabs.
The study of the prominence spectroscopic properties requires prominence models with consistently implemented interaction of the cool dense prominence plasma with the supporting magnetic field. In case of the modelling the prominence as a whole one can use a static approach because of the stable nature of the prominences on the large scales. The first description of the *magnetohydrostatic* (MHS) equilibrium of the prominences was suggested by Kippenhahn & Schlüter (KS - 1957). These authors proposed relatively simple 1D models to describe the whole prominence in the form of a vertical slab supported by a dipped magnetic field. We describe the KS model in the following section.
The spectroscopic analysis of the prominences also requires the radiative transfer computations. The multi-level non-LTE radiative transfer solving within the MHS prominence models of the KS-type was first considered by Heasley & Mihalas (1976). Similar 1D prominence models were published also by Anzer & Heinzel (1999), who considered an empirical PCTR instead of solving the energy balance. All such 1D slab models of the whole prominence neglect the fact, that the prominences are not homogenous but consist of the variety of fine structures. However, very narrow 1D slab models can also represent a kind of the prominence fine structures.
Figure 5.2 shows that the prominence fine structures consist of many vertically standing thread-like features. Such vertical threads can be represented by 2D models considering the thread vertically infinite and homogeneous, while its horizontal cross-section is obtained from the 2D MHS equilibrium of the KS-type, coupled with the 2D computation of the non-LTE radiative transfer. This approach was first used be Heinzel & Anzer (2001). The present thesis is based on these 2D prominence fine-structure models and thus we give here a detail description of the 2D MHS equilibrium (Sect. 3.2) and of the numerical methods used for the solving of the 2D radiative transfer (Sects. **??** and **??**).

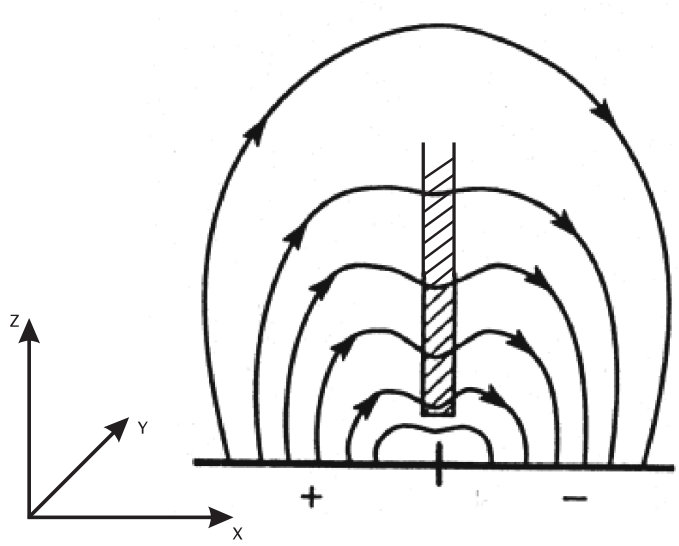

Figure 3.1: Sketch of the Kippenhahn-Schlüter 1D slab model.

3.1 The Kippenhahn-Schlüter 1D MHS model

The model of Kippenhahn & Schlüter (1957) deals with a simple magnetic arcade configuration (N-polarity) and describes well the basic properties of the interaction of the cool dense prominence plasma with the magnetic field. The prominence takes the form of the infinite slab oriented vertically with respect to the solar surface. The slab has finite geometrical thickness D. The coronal magnetic field penetrates the slab and thus supports the prominence plasma by the Lorentz force acting against the gravity.
For the description of the KS MHS equilibrium we use a Cartesian coordinate system with the x-axis perpendicular to the prominence slab, the y-axis along the slab and the z-axis in vertical direction perpendicular to the solar surface (Fig. 3.1). The prominence slab is homogeneous along the y-axis and the z-axis and therefore all quantities are independent of y and z. We assume for simplicity $B_y = 0$, which implies no shear. The equilibrium is then given by the equations

$$\frac{\partial B_x}{\partial x} = 0 \;\Rightarrow\; B_x = \text{constant} \tag{3.1}$$

$$-\frac{\partial p}{\partial x} - \frac{1}{4\pi} B_z \frac{\partial B_z}{\partial x} = 0 \tag{3.2}$$

$$\frac{1}{4\pi} B_x \frac{\partial B_z}{\partial x} - \rho g = 0\,. \tag{3.3}$$

The solution of the above set of equations can be found in e.g. Heinzel & Anzer (2005).
The MHS equilibrium equations become considerably simpler by using of the

column-mass coordinate m instead of the geometrical coordinate x. The column-mass coordinate m is defined by the relation $dm = -\rho dx$ with $m = 0$ at one surface of the prominence slab and $m = M$ at the other. Equations (3.2 and 3.3) then take the form

$$\frac{dp}{dm} + \frac{1}{4\pi} B_z \frac{dB_z}{dm} = 0 \tag{3.4}$$

$$\frac{1}{4\pi} B_x \frac{dB_z}{dm} + g = 0 \ . \tag{3.5}$$

These equations can be now easily integrated and have the following solution:

$$B_z(m) = -4\pi g m \frac{1}{B_x} + \text{const} \ ,$$

where the value of the constant can be obtained from the condition in the middle of the slab

$$B_z(M/2) = 0 \quad \Rightarrow \quad \text{const} = 4\pi \text{g} \frac{1}{\text{B}_\text{x}} \frac{\text{M}}{2}$$

and then

$$B_z(m) = 4\pi g \frac{1}{B_x} \left(\frac{M}{2} - m \right) \ . \tag{3.6}$$

Using the above expression for $B_z(m)$ we obtain

$$\frac{dp}{dm} = 4\pi g^2 \frac{1}{B_x^2} \left(\frac{M}{2} - m \right) \tag{3.7}$$

and by integration

$$p(m) = 4\pi g^2 \frac{1}{B_x^2} \left(\frac{M}{2} m - \frac{m^2}{2} \right) + \text{const}$$

$$p(m) = 4 p_c \frac{m}{M} \left(1 - \frac{m}{M} \right) + p_0 \ , \tag{3.8}$$

where p_0 is the coronal pressure at the slab surface. This equation was first derived by Heasley & Mihalas (1976) and it does not depend on the temperature T and therefore it can be used for any temperature structure.
We can now define the magnetic field intensity at the surface of the slab as B_{z1} which then gives for the total column-mass

$$M = \frac{B_x B_{z1}}{2\pi g} \ . \tag{3.9}$$

Using this formula, we obtain for the pressure at the center of the slab $m = M/2$

$$p_{\text{cen}} = p_\text{c} + p_0 \ , \tag{3.10}$$

where p_c represents the magnetic pressure

$$p_c = \frac{\pi g^2}{B_x^2}\frac{M^2}{2} = \frac{B_{z1}^2}{8\pi} \ . \tag{3.11}$$

The evaluation of the total geometrical thickness of the prominence slab needs the following integration

$$D = \int_0^M \frac{dm}{\rho} \ . \tag{3.12}$$

The MHS equilibrium equations based upon the column-mass coordinate m are rather simple, but in order to obtain the real spatial structure of the density and other quantities as functions of x one has to integrate the expression $dm = -\rho dx$. The integration depends on the structure of the temperature and ionization degree and in almost all cases it can be done only numerically.
The Kippenhahn-Schlüter model was derived for the N-polarity magnetic field configuration. Bommier & Leroy (1998) showed that a large majority of quiescent prominences has actually an inverse (I) polarity configuration (the coronal field lines penetrating the prominence have the opposite orientation as the field obtained inside the prominence). The I-polarity configuration was studied theoretically by Kuperus & Raadu (1974) and observationally discovered by Leroy et al. (1984). However, the MHS equilibrium equations presented above are also applicable locally for both field configurations.

3.2 2D fine-structure thread models

Although very narrow one-dimensional slab models can be used as a certain kind of first approach to the prominence fine-structure modelling, they are limited by a number of reasons. First, the elements of the prominence fine structures represent quite complicated features from the spectroscopic point of view. They can be optically thick in some wavelengths and thin in others, even within one spectral line (thick in the line core and thin in the wings). Thus the total outgoing radiation can be a sum of the outgoing radiations of several fine structures. Therefore, one should consider more than one fine-structure element within the modelling of the prominence fine structures. However, the internal structure and the distributions of the fine-structure elements within the prominence are not uniform, therefore the line-of-sight intersects each fine-structure element in different positions with rather different physical conditions. The 1D slab models cannot be used for the modelling of such a multi-element ensemble, because they are uniform in two directions. Second, during the observations, the line-of-sight is not always perpendicular to the surface of the fine-structure elements and therefore is passing through different parts of the PCTR (Prominence-Corona Transition Region). The shape of the PCTR depends on the orientation of the magnetic field lines with respect to the line-of-sight. The fact that this aspect can play an

important role in interpreting the observed spectra was established by a detailed analysis of the SOHO/SUMER spectra of two quiescent prominences (Heinzel et al. 2001). In one case a strong emission without any self-reversal was detected in the hydrogen Lyman lines higher than the Lyman-α. The other prominence exhibited a similar brightness in the Lyman spectrum but all lines up to the Lyman-8 were strongly reversed. Such situation can be explained by assuming considerably different shapes of the PCTR along the line-of-sight during each observation. In correspondence with the different plasma thermal conductivities along and across the magnetic field, the PCTR is expected to be more extended along the field lines with gently rising temperature from the cool centre to the boundaries compared to a thin transition region across the field with very steep temperature gradient.
The considerable difference of the Lyman line profiles observed along and across the magnetic field lines was theoretically confirmed by Heinzel et al. (2005). The authors have computed a grid of 18 2D prominence fine-structure models, developed by Heinzel & Anzer (2001), with empirical PCTR. This extended study shows that the synthetic Lyman line profiles obtained along the line-of-sight oriented across the magnetic field lines exhibit the self-reversal shape up to the Lyman-8. The synthetic profiles higher than the Lyman-β observed along the field lines have only emission shapes. The summary of Heinzel et al. (2005) is given in Sect. 4.1.
The sensitivity of the Lyman-line profiles to the orientation of the magnetic field with respect to the line-of-sight has been also proven recently by Schmieder et al. (2007) who studied a '*round-shape filament*' approaching the solar limb and consecutively showing its different parts above the limb having different orientations of the field lines with respect to the observers line-of-sight. The details of this study are given in Sect. 4.4.

The 2D fine-structure thread models by Heinzel & Anzer (2001) were developed to represent the vertical prominence fine-structure threads. The thicknesses of such vertical threads are of the order of the resolution limit of ground-based observatories (reaching today about hundred km). These vertical structures are believed to consist of many local magnetic dips caused by the weight of the cool plasma. Such local dips propagate vertically to form narrow vertical plasma threads. Such a scenario was first proposed by Poland & Mariska (1988).
In order to prescribe these vertical fine-structure threads by 2D models, Heinzel & Anzer (2001) considered them vertically infinite and homogenous with all quantities varying along their horizontal cross-section. For the description of such 2D threads we use a Cartesian coordinate system with the z-axis in vertical direction perpendicular to the solar surface and the $x-y$ horizontal plane. The direction of the x-axis is along the magnetic field lines, the y-axis is pointing across the magnetic field. Generally the magnetic field in prominences has a strong shear component (e.g. Bommier et al. 1994), but the prominence fine-structure threads

are formed along the field lines and therefore one can take $B_y = 0$. The equations of the 1D MHS equilibrium of the KS type described in previous section can be generalized into 2D by allowing all quantities to vary also in the y-direction. The total pressure will be then given by

$$p_{\rm T} = p + \frac{B_x^2(y) + B_z^2(y)}{8\pi} \ , \tag{3.13}$$

where p is the sum of the gas and the turbulent pressure. For the case of 1D slabs this total pressure is independent of x and since there is no magnetic tension force in the x-direction this will lead to the equilibrium in the x-direction. In case of the 2D vertical threads the pressure equilibrium in the y-direction is also required. This means that $p_{\rm T}$ has to be uniform in the whole $x - y$ plane. The requirement for vertical equilibrium then leads to the generalization of Eq. (3.8) to the form

$$p(m, y) = 4p_{\rm c}(y)\frac{m}{M(y)}\left(1 - \frac{m}{M(y)}\right) + p_0 \tag{3.14}$$

with the magnetic pressure $p_{\rm c}$ defined as

$$p_{\rm c}(y) = \frac{B_{z1}^2(y)}{8\pi} \tag{3.15}$$

and with the total column-mass integrated along the x-direction given by

$$M(y) = \frac{B_x(y)B_{z1}(y)}{2\pi g} \ . \tag{3.16}$$

Here p_0 is the boundary coronal pressure, g is the gravitational acceleration at the solar surface, $B_x y$ the horizontal magnetic field (constant along a given field line) and $B_{z1}(y)$ the vertical field at the boundary of the thread. Again the column-mass coordinate m is used instead of the geometrical x coordinate. The use of $m - y$ coordinate system for the equilibrium calculations makes the equilibrium equations independent of the assumed temperature profile. Since $p_{\rm T}$ is constant everywhere we now obtain the relation

$$\frac{B_x^2(y) + B_{z1}^2(y)}{8\pi} + p_0 = \frac{B_{x0}^2}{8\pi} + p_0 \tag{3.17}$$

which is equivalent to

$$B_{z1}^2(y) = B_{x0}^2 - B_x^2(y) \ . \tag{3.18}$$

Here B_{x0} is the horizontal magnetic field which exists in the region between individual threads. $B_x y$ can be eliminated using Eqs. (3.16) and (3.18)

$$\frac{B_{z1}^2(y)}{8\pi} = \frac{1}{2}\left(\frac{B_{x0}^2}{8\pi} - \sqrt{\left(\frac{B_{x0}^2}{8\pi}\right)^2 - \frac{M^2(y)g^2}{4}}\right) \ . \tag{3.19}$$

Substituting of Eq. (3.19) into Eq. (3.15) and consequently into Eq. (3.14) results in an expression for $p(m, y)$ completely determined by the choice of the function $M(y)$ and the free parameters p_0 and B_{x0}.
Note that Eq. (3.19) represents one particular solution valid only when the magnetic dip is shallower than 45° (i.e. for $B_x(y) > B_{z1}(y)$ considering only positive values of the field components). Configurations with $B_x(y) < B_{z1}(y)$ require more complex mass distributions.

The transition region between the cool plasma of the prominence thread and the hot coronal plasma is given empirically, rather than by solving of the energy-balance problem. Due to the different plasma thermal conductivities along and across the magnetic field lines, the temperature profile of the PCTR is more extended along the field with gently rising temperature compared to the narrow transition region across the field with a very steep temperature gradient. Such a PCTR temperature structure can be described by an empirical formula with

$$T(m, y) = T_{\rm cen}(y) + [T_{\rm tr} - T_{\rm cen}(y)] \left\{ 1 - 4\frac{m}{M(y)} \left[1 - \frac{m}{M(y)} \right] \right\}^{\gamma_1} , \qquad (3.20)$$

where the temperature at the boundary $T_{\rm tr}$ is taken as constant and the exponent γ_1 has to be chosen properly. The central temperature $T_{\rm cen}$ is specified as

$$\begin{aligned} T_{\rm cen}(y) &= T_{\rm tr} - (T_{\rm tr} - T_0) \left(1 - \left| \frac{y}{\delta} \right|^{\gamma_2} \right) , \quad \text{for} \quad |y| \le \delta \qquad (3.21) \\ T_{\rm cen}(y) &= T_{\rm tr} , \quad \text{for} \quad |y| > \delta \end{aligned}$$

and the total column-mass integrated along the x-direction $M(y)$ is given by

$$\begin{aligned} M(y) &= M_0 \left(1 - \left| \frac{y}{\delta} \right|^{\gamma_3} \right) , \quad \text{for} \quad |y| \le \delta \qquad (3.22) \\ M(y) &= 0 , \quad \text{for} \quad |y| > \delta \ . \end{aligned}$$

M_0 is the maximum column density, T_0 the minimum central temperature, 2δ represents the width of the prominence fine-structure thread and γ_2 and γ_3 are free exponents.
The above set of equations completely describe the thread structure as a function of m and y. In order to obtain the geometrical structure of the thread as a function of x and y, a transformation of the mass coordinate m to the spatial coordinate x is needed. Such a transformation requires the following integration

$$x = \int_{M(y)/2}^{m} \frac{1}{\rho} dm' \qquad (3.23)$$

for each value of y (ρ is the density). The boundaries of the thread are obtained by setting $m = 0$ and $m = M(y)$.

For the above integration the relation between p and ρ is needed. The pressure in the thread is given by

$$p = p_{\rm g} + p_{\rm t} \ , \tag{3.24}$$

where the turbulent pressure $p_{\rm t}$ has the form

$$p_{\rm t} = \frac{1}{2}\rho v_{\rm t}^2 \ . \tag{3.25}$$

Here v_t is the turbulent velocity which is taken here as a constant fraction of the local sound velocity $c_{\rm s}$

$$v_{\rm t} = \epsilon c_{\rm s} \ , \tag{3.26}$$

where $c_{\rm s}$ is given by

$$c_{\rm s}^2 = \gamma \frac{kT}{\overline{m}} \ , \tag{3.27}$$

where γ is the ratio of specific heats.
With this assumption we then get

$$p = \rho kT \frac{1 + 1/2\gamma\epsilon^2}{\overline{m}} \ . \tag{3.28}$$

The mean molecular mass $\overline{m}$ is given by

$$\overline{m} = \frac{1 + 4\alpha}{1 + \alpha + i} m_{\rm H} \ , \tag{3.29}$$

where α is the ratio of helium to hydrogen particle densities, i the local ionization degree of hydrogen and $m_{\rm H}$ is the mass of the hydrogen atom.

The MHS equilibrium in 2D is expressed using the column-mass coordinate m and the spatial coordinate y, while the 2D radiative transfer computations have to be performed on the Cartesian $x - y$ mesh. The transformation between m and x coordinates requires the integration (Eq. 3.23) depending on the density and thus on the local ionization degree. For the ionization degree i one can take a simple initial estimate

$$i = 1 - (1 - i_{\rm c}) \left(\frac{T_{\rm tr} - T}{T_{\rm tr} - T_{\rm cen}} \right)^2 \ , \tag{3.30}$$

where the ionization degree at the centre of the thread is $i_{\rm c} = 0.3$, as suggested from the results of Anzer & Heinzel 1999. On the obtained $x - y$ mesh, the 2D radiative transfer problem is solved (a detail description of the techniques used to compute the 2D radiative transfer is given in the Sects. **??** and **??**) and a new structure of the ionization degree is obtained. However, the new ionization degree structure differs from the initial estimate and thus also the $x - y$ mesh is either expanded or compressed along the x-direction. Therefore an iterative approach is

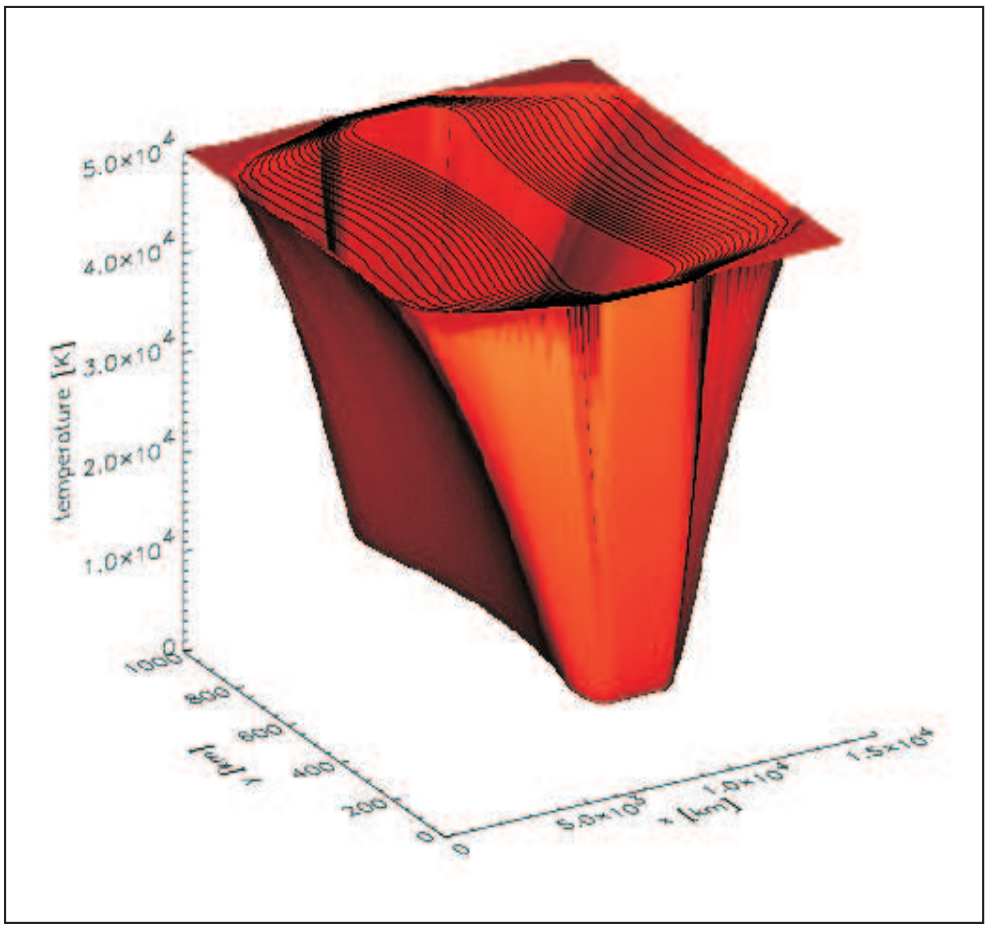

Figure 3.2: Temperature structure of the prominence vertical thread.

needed in order to obtain a final $x-y$ mesh with conversed 2D radiative transfer computations. The details of such adaptive mesh technique are given in Heinzel & Anzer (2003).

The examples of the temperature and density structure variation on the $x-y$ horizontal plane obtained by 2D thread modelling are shown in Figs. 3.2 and 3.3. The overplotted contours represents the iso-lines of the temperature and the density. Note, that the x and y axis are not drawn to the scale. The y dimension of the thread is 1000 km while the x dimension reaches 15 000 km. The iso-contours of the temperature clearly shows different temperature gradients along and across the magnetic field. The temperature along the field is rising gradually from the center of the thread to the boundaries while the temperature across the magnetic field exhibits a very steep gradient given by the reduced thermal conductivity of the prominence plasma across the magnetic field lines.

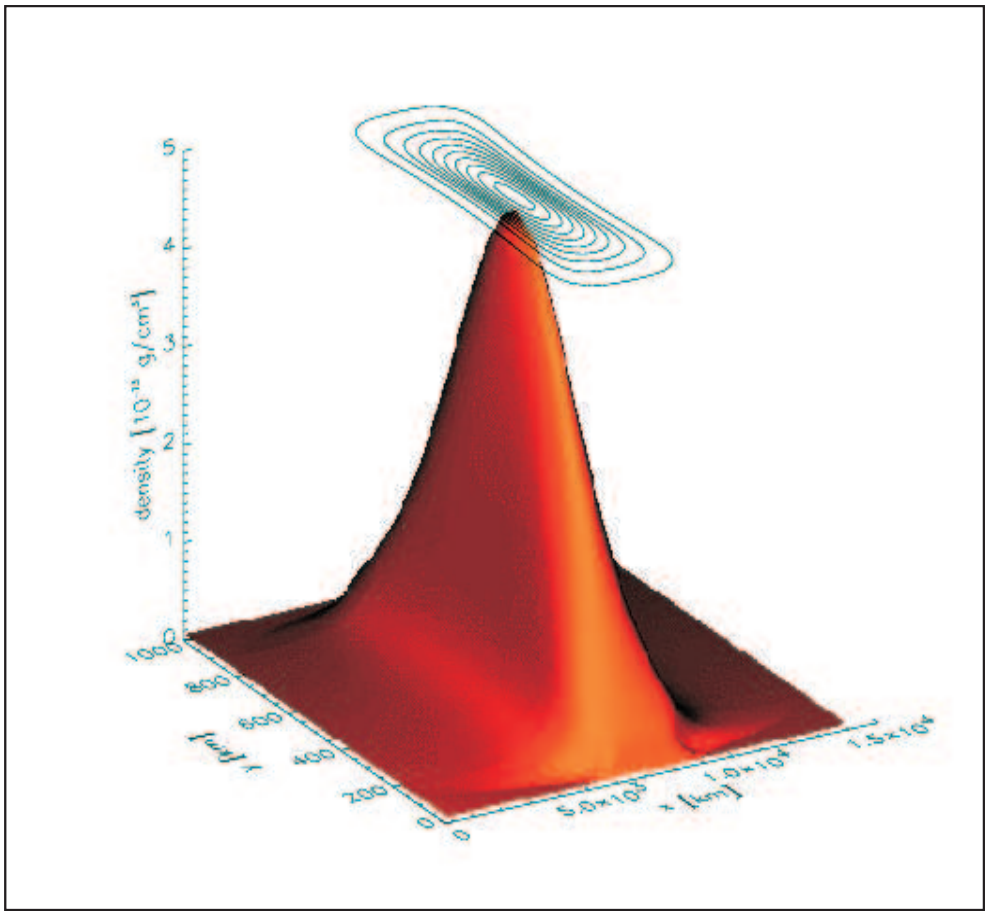

Figure 3.3: Density structure of the prominence vertical thread.

IV. Radiative transfer

An insight into the theory of non-LTE radiative transfer and corresponding numerical techniques is given.

The radiation from astrophysical objects carries a vast amount of information about these objects. Therefore the understanding of processes of origin and transfer of the radiation and the development of appropriate numerical methods represents a matter of considerable importance.
The goal of the prominence modelling is to construct theoretical models of a prominence atmosphere and to predict corresponding synthetic spectrum. The obtained synthetic spectrum compared to the observed one can be used to verify the validity of the prominence models. In case the prominence model produces a realistic synthetic spectrum, one can obtain the parameters of the prominence plasma such as the temperature, density, ionization degree, etc.
The numerical methods used in the prominence non-LTE modelling have to correspond with the nature of the used atmosphere models. The more realistic models of the prominence atmosphere are available, the more sophisticated radiative transfer methods are required. The non-LTE radiative transfer problem cannot be treated analytically and therefore the prominence modelling requires numerical solutions. We give in this chapter a brief insight into the various numerical radiative-transfer methods with the emphasis on the methods used in the 2D prominence fine-structure modelling performed in this thesis. For a more complete overview of the radiative transfer theory the reader is referred to the textbooks such as Mihalas (1978) and Mihalas & Weibel-Mihalas (1999) or the lecture-notes of Hubeny (1997) and Rutten (2003).

4.1 The radiative transfer equation

We present here the basic definitions of the radiation intensity and related quantities and give a phenomenological derivation of the radiative transfer equation. The following expressions are taken from the lecture-notes of Hubeny (1997).

Let us first start with the definition of the *specific intensity* of radiation $I(\mathbf{r}, \mathbf{n}, \nu, t)$,

at a position $\mathbf{r}$, in a direction $\mathbf{n}$ ($\mathbf{n}$ is a unit verctor), with a frequency ν and at a time t. The energy transported by the radiation within a frequency range $(\nu, \nu + \mathrm{d}\nu)$, through an area $\mathrm{d}S$, into a spatial angle $\mathrm{d}\omega$, within a time interval $\mathrm{d}t$ is given by

$$\mathrm{d}E = I(\mathbf{r}, \mathbf{n}, \nu, t)\ \mathrm{d}S\ \cos\theta\ \mathrm{d}\omega\ \mathrm{d}\nu\ \mathrm{d}t\ . \tag{4.1}$$

Here θ is the angle between the direction of propagation $\mathbf{n}$ and the normal to $\mathrm{d}S$. The units of the specific intensity I are erg $\mathrm{cm}^{-2}\mathrm{sec}^{-1}\mathrm{sr}^{-1}\mathrm{Hz}^{-1}$.
Variations of the specific intensity due to radiative interactions with the matter are described by the *radiative transfer equation*. The processes of the matter interaction with the radiation field are described by the absorption and emission coefficients.

The *absorption coefficient* describes an amount of the energy removed from the radiation field by its interaction with the matter. An element of the material with a length $\mathrm{d}s$ and a cross-section area $\mathrm{d}S$ removes from a beam $\mathrm{d}\omega$ of the radiation I the energy

$$\mathrm{d}E = \chi(\mathbf{r}, \mathbf{n}, \nu, t)\ I(\mathbf{r}, \mathbf{n}, \nu, t)\ \mathrm{d}s\ \mathrm{d}S\ \mathrm{d}\omega\ \mathrm{d}\nu\ \mathrm{d}t\ . \tag{4.2}$$

The dimension of the absorption coefficient χ is cm^{-1} and therefore $1/\chi$ describes a characteristic distance a photon can travel before it is absorbed (*photon mean free path*).

The *emission coefficient* describes an amount of the energy released by the matter into the radiation field. An element of the material with a length $\mathrm{d}s$ and a cross-section area $\mathrm{d}S$ releases the energy

$$\mathrm{d}E = \eta(\mathbf{r}, \mathbf{n}, \nu, t)\ \mathrm{d}s\ \mathrm{d}S\ \mathrm{d}\omega\ \mathrm{d}\nu\ \mathrm{d}t\ . \tag{4.3}$$

The units of the emission coefficient are η is erg $\mathrm{cm}^{-3}\mathrm{sec}^{-1}\mathrm{sr}^{-1}\mathrm{Hz}^{-1}$.

With the definitions of the specific intensity and the absorption and emission coefficients we can express the difference between the amount of energy entering an element of the material with a length $\mathrm{d}s$ and a cross-section area $\mathrm{d}S$ at position $\mathbf{r}$ and time t and the amount of energy emerging from the same element at position $\mathbf{r} + \Delta\mathbf{r}$ at time $t + \Delta t$ in the form

$$\begin{aligned}[I(\mathbf{r} + \Delta\mathbf{r}, \mathbf{n}, \nu, t + \Delta t) - I(\mathbf{r}, \mathbf{n}, \nu, t)]\ \mathrm{d}S\ \mathrm{d}\omega\ \mathrm{d}\nu\ \mathrm{d}t = \\ [\eta(\mathbf{r}, \mathbf{n}, \nu, t) - \chi(\mathbf{r}, \mathbf{n}, \nu, t) I(\mathbf{r}, \mathbf{n}, \nu, t)]\ \mathrm{d}s\ \mathrm{d}S\ \mathrm{d}\omega\ \mathrm{d}\nu\ \mathrm{d}t\ .\end{aligned} \tag{4.4}$$

The difference of the specific intensities on the left hand side can be expressed as

$$\Delta I = \frac{\partial I}{\partial s}\mathrm{d}s + \frac{\partial I}{\partial t}\mathrm{d}t = \left(\frac{\partial I}{\partial s} + \frac{1}{c}\frac{\partial I}{\partial t}\right)\ \mathrm{d}s\ . \tag{4.5}$$

The derivative $\partial I/\partial s$ can be in general 3D case expressed in terms of an orthogonal coordinate system as

$$\frac{\partial I}{\partial s} = \frac{\partial I}{\partial x}\frac{\partial x}{\partial s} + \frac{\partial I}{\partial y}\frac{\partial y}{\partial s} + \frac{\partial I}{\partial z}\frac{\partial z}{\partial s} = \frac{\partial I}{\partial x}n_x + \frac{\partial I}{\partial y}n_y + \frac{\partial I}{\partial z}n_z \ , \tag{4.6}$$

where (n_x, n_y, n_z) are the components of the unit vector $\mathbf{n}$. The term $c^{-1}(\partial I/\partial t)$ is usually neglected.
In the case of a static one-dimensional (1D) planar atmosphere (e.g. 1D prominence slab model) has Eq. 4.6 the form

$$\frac{\partial I}{\partial s} = \frac{\partial I}{\partial x}n_x \tag{4.7}$$

and with $n_x = (dx/ds) = \cos\theta \equiv \mu$ we obtain a simple 1D radiative transfer equation

$$\mu\frac{\mathrm{d}I(\nu,\mu,x)}{\mathrm{d}x} = \eta(\nu,\mu,x) - I(\nu,\mu,x)\chi(\nu,\mu,x) \ . \tag{4.8}$$

We can now define the elementary optical path as

$$\mathrm{d}\tau_\nu \equiv -\chi_\nu \mathrm{d}x \ . \tag{4.9}$$

Here we drop the explicit indication of the dependence on the geometrical scale x and the angle μ and we write the dependence on the frequency ν as a subscript. Moreover we can define the *source function* as a ratio between the emission and absorption coefficients

$$S_\nu \equiv \frac{\eta_\nu}{\chi_\nu} \ . \tag{4.10}$$

With usage of the above definitions we rewrite the radiative transfer equation into a very simple and well-known form

$$\mu\frac{\mathrm{d}I_\nu}{\mathrm{d}\tau_\nu} = I_\nu - S_\nu \ . \tag{4.11}$$

4.2 LTE vs. non-LTE

The first numerical methods for solving the radiative transfer were severely limited by the computational power of the available computers at the time. Therefore they tended to be as simple as possible and an assumption of the *Local Thermodynamic Equilibrium* (LTE) was frequently used. However, with the development of the computers and consequently with the development of more realistic stellar atmosphere models, the need for implementation of the sophisticated non-LTE radiative transfer methods became obvious.
The assumption of the LTE is based on the employment of the standard thermodynamic relations locally, despite the gradients existing in the atmosphere.

It means that all the particle distribution functions may be evaluated locally, without referring to the surrounding physical conditions. Therefore the LTE is characterized by the following three distributions for the massive particles and by the source function equal S_ν to the Planckian distribution function.
The *Maxwellian velocity distribution* of particles

$$f(\mathbf{v})\mathrm{d}\mathbf{v} = (m/2\pi kT)^{3/2} \exp(-mv^2/2kT)\mathrm{d}\mathbf{v} \ , \tag{4.12}$$

where m represents the mass of the particle and k the Boltzmann constant.
The *Boltzmann excitation equation*

$$(n_j/n_i) = (g_j/g_i) \exp[-(E_j - E_i)/kT] \ , \tag{4.13}$$

where g_i is the statistical weight of the level i and E_i is the level energy. For hydrogen $g_i = 2i^2$.
The *Saha ionization equation*

$$\frac{N_I}{N_{I+1}} = n_\mathrm{e} \frac{U_I}{U_{I+1}} C T^{-3/2} \exp(\chi_I/kT) \ , \tag{4.14}$$

where N_I represents the total number density of ionization stage I. U is the partition function defined as $U = \sum_1^\infty g_i \exp(-E_i/kT)$. χ_I is the ionization potential of ion I and C is a constant given as $C = (h^2/2\pi mk)^{3/2}$.
The same temperature T in LTE applies to all kinds of particles and distributions.

In LTE the source function S_ν is equal to the *Planck function*

$$B(\nu, T) = \frac{2h\nu^3}{c^2} \frac{1}{\exp(h\nu/kT) - 1} \ . \tag{4.15}$$

Microscopically, the assumption of LTE means that all atomic processes are in detailed balance.

In the non-LTE case, atomic level-populations differ from the equilibrium state given by the Boltzman (Eq. 4.13) and the Saha (Eq. 4.14) equations. Therefore in order to obtain the populations of the atomic levels one has to employ the statistical equilibrium equations. In case of the *statistical equilibrium*, the radiation field (in all directions and frequencies) and the level populations do not vary with the time. Thus the equations of the statistical equilibrium have the general form (Heinzel & Anzer 2005)

$$\frac{\mathrm{d}n_i}{\mathrm{d}t} = \sum_{j\neq i}^{N} n_j(R_{ji} + C_{ji}) - n_i \sum_{j\neq i}^{N} (R_{ij} + C_{ij}) \tag{4.16}$$

$$\frac{\mathrm{d}n_i}{\mathrm{d}t} = \frac{\partial n_i}{\partial t} + \frac{\partial n_i v}{\partial s} \ ,$$

where n_i represents the population of level i, N is the total number of levels including the continuum and v is the macroscopic velocity of a plasma flow. R_{ij} and R_{ji} represent the radiative rates and C_{ij} and C_{ji} are the collisional rates. We do not give the explicit definitions of the radiative and collisional rates within this thesis, but we refer the reader to the according literature (e.g. Mihalas 1978).

The solar prominences are structures with rather low plasma densities. This implies that the assumption of LTE for the prominence modelling is not realistic and the non-LTE approach to the prominence modelling is necessary. The source function of most of prominence emission lines is dominated by scattering.

In the following sections we give descriptions of the numerical methods used for solving the radiative transfer problem in the 2D prominence fine-structure models of Heinzel & Anzer (2001). The results of this thesis are based on the prominence fine-structure modelling using this kind of models.

4.3 Classical Lambda Iterations

The classical approach to the finding of the source function are the *Lambda Iterations* (LI). This technique is based on the use of the *Lambda operator* (Λ_ν). We do not give the exact definition of the Λ_ν operator here because it is easy to find in any textbook considering the radiative transfer theory.
The *angle-averaged mean intensity* of radiation J_ν (the first moment of the radiation intensity) can be expressed as an action of the Λ_ν operator on the source function

$$J_\nu(\tau_\nu) = \Lambda_\nu[S_\nu(t)] \ . \tag{4.17}$$

The two-level line source function in complete redistribution is defined as

$$S_\nu = (1-\epsilon)\overline{J} + \epsilon B_\nu \ , \tag{4.18}$$

where B_ν is the Planck function and $\overline{J} \equiv \int \phi_\nu J_\nu \mathrm{d}\nu$ is called the *frequency-averaged mean intensity*. Here, ϕ_ν is the line absorption profile. ϵ represents the destruction probability, i.e. the probability that an absorbed photon is destroyed by a collisional de-excitation process rather than being re-emitted.
By substitution of the Λ_ν operator into Eq. (4.18) we obtain for the source function the formula

$$S_\nu = (1-\epsilon)\Lambda_\nu[S_\nu] + \epsilon B_\nu \ , \tag{4.19}$$

which directly shows, that S_ν has to be know non-locally in order to find S_ν locally.
Equation (4.19) can be solved numerically using the classical LI scheme

$$S_\nu^{(n+1)} = (1-\epsilon)\Lambda_\nu[S_\nu^{(n)}] + \epsilon B_\nu \ , \tag{4.20}$$

starting with the first guess for $S_\nu^{(1)}$, e.g. $S_\nu^{(1)} = B_\nu$.
The problem of this relatively simple iterative scheme is that the LI method converges very slowly at large optical depths (Mihalas 1978). The reason of the slow convergence of the LI method is that it solves the non-local radiative transfer equation (Eq. 4.22) and the local population equation (Eq. 4.18) sequentially. Thus it transfers the old $S_\nu^{(n)}$ to the new $S_\nu^{(n+1)}$ using the corrections which propagate as much as photons do. Therefore at large optical depths the correction is as small as the mean free path of the photons. For this reason, extremely high number of iterations ($10^3 - 10^8$ for strong scattering cases (Rutten 2003)) are needed in order to obtain correct results. However, the classical LI method remains useful for situations dealing with small optical depths, where photons can travel far and therefore the corrections to the source function are sufficient.

4.4 Accelerated Lambda Iterations

The technique of the convergence acceleration of the LI method is based on the splitting of the Λ_ν operator and on the introduction of the *Approximate Lambda Operator* (ALO) Λ_ν^* (Cannon 1973).
The Λ_ν^* operator should be a simple one because of the requirement of the inverse $(\Lambda_\nu^*)^{-1}$ operator and therefore the need of the numerical matrix inversions. On the other hand, Λ_ν^* has to be sufficiently close to the exact Λ_ν operator in order to obtain fast enough convergence rate of the iteration process. Such contradictory requirements cause considerable difficulties in the construction of the optimal Λ_ν^* operator.

The operator splitting technique can be written in the form

$$\Lambda_\nu = \Lambda_\nu^* + (\Lambda_\nu - \Lambda_\nu^*) \ . \tag{4.21}$$

Then for the angle-averaged mean intensity J_ν we obtain

$$J_\nu = \Lambda_\nu^*[S_\nu] + (\Lambda_\nu - \Lambda_\nu^*)[S_\nu] \tag{4.22}$$

and using the definition of the two-level line source function (Eq. 4.18) we obtain an iteration scheme

$$S_\nu^{(n+1)} = (1-\epsilon)\Lambda_\nu^*[S_\nu^{(n+1)}] + (1-\epsilon)(\Lambda_\nu - \Lambda_\nu^*)[S_\nu^{(n)}] + \epsilon B_\nu \ . \tag{4.23}$$

Reshuffling of the above expression gives

$$S_\nu^{(n+1)} = [1 - (1-\epsilon)\Lambda_\nu^*]^{-1} \left[S_\nu^{\rm FS} - (1-\epsilon)\Lambda_\nu^*)[S_\nu^{(n)}]\right] \ , \tag{4.24}$$

where $S_\nu^{\rm FS} \equiv (1-\epsilon)\Lambda_\nu[S_\nu^{(n)}] + \epsilon B_\nu$ is the formal solution (Eq. 4.19) obtained with the exact Λ_ν operator from the known source function $S_\nu^{(n)}$. The important

advantage of Eq. (4.24) is that only the approximate operator Λ^*_ν is inverted instead of the full Λ_ν operator. Therefore a proper choice of the Λ^*_ν operator lowers the requirements of CPU-time. The fact that the convergence rate at the large depths is much faster using operator splitting technique than using the classical LI gives this method the name *Accelerated Lambda Iterations* (ALI).

The main problem of the ALI method lays in the proper choice of the Approximate Lambda Operator Λ^*_ν. This should be simple to construct and easy to invert on one hand and should contain the basic physical properties of the exact Λ_ν operator on the other hand. We present here several choices of the approximate Λ^*_ν operator with emphasis on the one used within the radiative transfer computations in the prominence fine-structure models of Heinzel & Anzer (2001).

Core saturation operator. The construction of this Λ^*_ν operator is based on the fact, that the photons from the line centers with very short mean free paths are contributing most to the slow convergence of the classical LI (Rybicki 1971) and they are also the photons that carry least information about the non-local conditions. Thus the Λ^*_ν operator is constructed by the choice of the saturation limit (γ parameter) and takes into account only the wing photons that carry most of the non-local information (Scharmer 1981)

$$\Lambda^*_\nu[S_\nu(\tau_\nu)] = S_\nu(\tau_\nu) \qquad \text{or} \qquad \Lambda^*_\nu = 1 \qquad \text{for} \qquad \tau_\nu \geq \gamma \; . \tag{4.25}$$

The disadvantage of this Λ^*_ν operator is that the somewhat arbitrary choice of the parameter γ affects the convergence rate and the optimum value of γ is hard to determine.

The *Scharmer operator* represents an alternative choice of the approximate Λ^*_ν operator to the core saturation operator and has the Eddington-Barbier-like character (Scharmer 1981). We do not give the full description of the Scharmer operator here, but we refer the reader to the original work of Scharmer (1981) or to the radiative transfer theory textbooks such as Rutten (2003). The Scharmer Λ^*_ν operator is easy to implement and provides an excellent convergence rate and therefore it is widely used (e.g. Carlsson's (1986) code MULTI). The main disadvantage of the Scharmer Λ^*_ν operator is that although it works perfectly in 1D geometry, its generalization to the multi-dimensional geometry is considerably complicated.

Local operator. Olson et al. (1986) constructed a very simple approximate Λ^*_ν operator (often called the OAB operator) by using only the diagonal of the exact Λ_ν operator matrix. The inversion of such Λ^*_ν operator is then trivial. This represents the main advantage of the OAB operator over the Scharmer operator, together with much easier implementation into multi-dimensional geometries. We do not show here the construction of the local operator in 1D which is rather non-trivial;

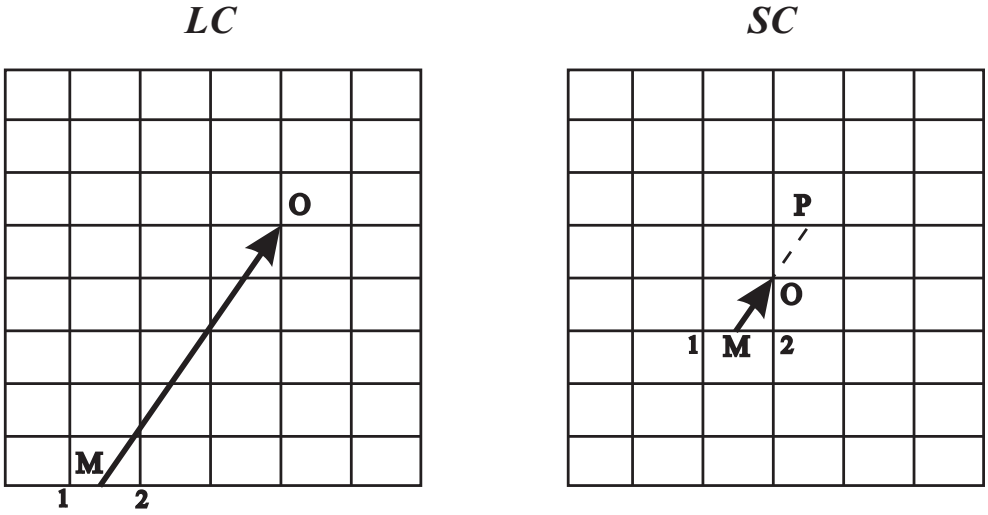

Figure 4.1: Sketch of the long characteristics (on the left) and the short characteristic technique (on the right).

an efficient recipe is given in Appendix B of Rybicki & Hummer (1991). The approach of Auer & Paletou (1994) to the application of the OAB Λ^*_ν operator into the two-dimensional geometry was reproduced during the development of the 2D radiative transfer code for the prominence fine-structure models of Heinzel & Anzer (2001).

4.5 2D multi-level ALI with short characteristics

The 2D prominence models were developed first by Vial (1982) who considered the whole prominence in the form of 2D slab and employed the 2D radiative transfer technique of Mihalas et al. (1978). The 2D models of the whole prominence were then considered by Auer & Paletou (1994) and Paletou (1995). Finally, Heinzel & Anzer (2001) developed 2D models for the prominence fine-structure vertical threads.
In order to solve the non-LTE radiative transfer in the 2D geometry numerically using the ALI method (Eq. 4.24) we need two things. The first is the technique for the efficient solution of the formal transfer problem on the 2D geometrical grid. The second is the choice of the approximate Λ^*_ν operator. Heinzel & Anzer (2001) used the Λ^*_ν operator in the form of the exact diagonal of the Λ_ν.

The radiative transfer equation (4.8) in the 2D geometry has the form

$$\mu\frac{\mathrm{d}I(\nu,\gamma,\mu,x,y)}{\mathrm{d}x}+\gamma\frac{\mathrm{d}I(\nu,\gamma,\mu,x,y)}{\mathrm{d}y}=\eta(\nu,\gamma,\mu,x,y)-I(\nu,\gamma,\mu,x,y)\chi(\nu,\gamma,\mu,x,y)\,, \tag{4.26}$$

where μ and γ represents angle cosines on the x and y-axis, respectively.
The obvious idea for the formal solution of the radiative transfer at all points of the 2D geometrical grid is known as the *Long Characteristics* (LC) method. It involves for each point of the 2D grid the set of rays extending across the entire grid along each specific direction. Such a ray constructed at the grid-point O is shown in Fig. 4.1. The values of the quantities on the grid-cell boundaries along the ray are obtained by interpolation. The intensity in one point of the grid is found by solving the radiative transfer along the entire ray. This proves to be rather inefficient, because the efficiency of solving the 1D radiative transfer along each ray scales as N, where N represents a number of the grid-points along the one axis of a square geometrical grid. Thus the LC method efficiency scales as N^3 times the number of rays.

Kunasz & Auer (1988) demonstrated that the efficiency of the 2D radiative transfer computations dramatically increases with the implementation of the *Short Characteristics* (SC) method instead of the LC. Therefore, instead of constructing the rays spanning the entire geometrical grid, the SC rays are constructed for each grid-point only from the closest grid-cell boundary along the specific direction (see Fig. 4.1). The values of the quantities at the point M are obtained by interpolation between the nearest grid-points. The efficiency of the SC method thus scales as N^2 times the number of rays.
Since the specific intensity is a priori known only on the boundaries of the 2D geometrical grid, the information is propagated using SC from one corner of the grid. In case the intensity I_{M} at the point M is known we can evaluate the unknown intensity in the specific direction (I_{O}) simply by the integration over the grid-cell from M to O

$$I_{\mathrm{O}} = I_{\mathrm{M}} e^{-\Delta\tau_{\mathrm{M}}} + \int_0^{\Delta\tau_{\mathrm{M}}} S(t) e^{-(\Delta\tau_{\mathrm{M}} - t)} \mathrm{d}t \ , \tag{4.27}$$

where $\Delta\tau_{\mathrm{M}}$ represents the optical depth along the segment MO. The same integral can be written also for the segment OP. It is necessary to use parabolic or even higher order interpolation in order to evaluate the previous integral. The linear interpolation would lead to serious errors in the high scattering situations. For the evaluation of the above integral Heinzel & Anzer (2001) used the interpolation scheme developed by Auer & Paletou (1994). The source function $S(t)$ takes the form $S(t) = S_{\mathrm{O}} + c_{\mathrm{M}} t + c_{\mathrm{P}} t^2$ and than the integral part of Eq. (4.27) is given by

$$\int_0^{\Delta\tau_{\mathrm{M}}} S(t) e^{-(\Delta\tau_{\mathrm{M}} - t)} \mathrm{d}t = S_{\mathrm{O}} w_{\mathrm{O}} + c_{\mathrm{M}} w_{\mathrm{M}} + c_{\mathrm{P}} w_{\mathrm{P}} \ . \tag{4.28}$$

The coefficients used in the above formula can be efficiently expressed in the terms of the source functions differences

$$\begin{aligned} c_{\rm M} &= (d_{\rm P}\Delta\tau_{\rm M} + d_{\rm M}\Delta\tau_{\rm P})/(\Delta\tau_{\rm M} + \Delta\tau_{\rm P}) \\ c_{\rm P} &= (d_{\rm P} - d_{\rm M})/(\Delta\tau_{\rm M} + \Delta\tau_{\rm P}) \\ d_{\rm M} &= (S_{\rm O} - S_{\rm M})/\Delta\tau_{\rm M} \\ d_{\rm P} &= (S_{\rm P} - S_{\rm O})/\Delta\tau_{\rm P} \end{aligned} \tag{4.29}$$

and the weights have the form

$$\begin{aligned} w_{\rm O} &= 1 - e^{-\Delta\tau_{\rm M}} \\ w_{\rm M} &= w_{\rm O} - \Delta\tau_{\rm M} e^{-\Delta\tau_{\rm M}} \\ w_{\rm P} &= 2w_{\rm M} - \Delta\tau_{\rm M}^2 e^{-\Delta\tau_{\rm M}} \ . \end{aligned} \tag{4.30}$$

With the specified coefficients (Eqs. 4.29) and weights (Eqs. 4.30) we can evaluate the diagonal of the Λ_ν operator at each grid-point as a sum over all directions of the right hand side of Eq. (4.28) with the coefficients $d_{\rm M}$ and $d_{\rm P}$ defined by setting $S_{\rm O} = 1$ and $S_{\rm M} = S_{\rm P} = 0$.

To obtain the intensity $I_{\rm M}$ at the point M we have to interpolate its value from the value at the grid-points 1 and 2. Such an interpolation depends only on the geometrical grid and the chosen directions of the SC rays. Auer & Paletou (1994) give the detailed description of the algorithm for the interpolation on the 2D geometrical grids. The SC rays should homogenously cover the entire quadrant of the geometrical grid and can be specified by the angle quadrature set.
Heinzel & Anzer (2001) used for the specification of the quadrature set the discrete angle pairs of Carlson (1963) and the linear interpolation method for the interpolations on the 2D geometrical grid.

4.6 Multi-thread models

The elements of the prominence fine structures exhibit complex spectroscopic behaviour. They can be optically thick in some wavelengths and thin in others, even within one spectral line (thick in the line core and thin in the wings). In the optically thin case the observed radiative output represent a sum of radiative output of several fine-structure elements integrated along the line-of-sight. Therefore the consideration of more than one element for the prominence modelling have a considerable effect on the profiles of the synthetic spectral lines.

The important aspect of the multi-element approach to the prominence fine-structure modelling represents the mutual radiative interaction of the fine-structure elements. This was treated by Heinzel (1989) and by Zharkova & Morozhenko (1998) who used a simplified 1D slab prominence models. However, in most

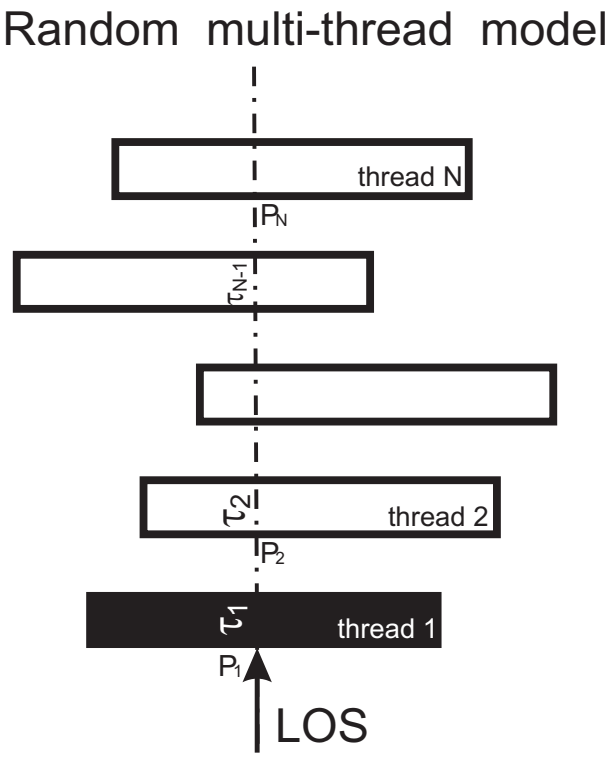

Figure 4.2: Scheme of the model with randomly arranged threads. LOS is the line-of-sight.

other cases was the mutual radiative interaction of the fine-structure elements neglected. Such 1D multi-slab prominence fine-structure models without the radiative interaction between the slabs were considered by Fontenla et al. (1996) and by Heinzel et al. (2001).

The main disadvantage of the 1D multi-slab prominence fine-structure models is that the 1D slabs are uniform along two of their axis and therefore the integrated radiative output of such 1D-slab ensemble does not depend on the position of the line-of-sight. This can be improved by consideration of the 2D thread models instead of the 1D slab prominence models.

The 2D fine-structure thread models of Heinzel & Anzer (2001) exhibits strong variation of the thermodynamic properties (e.g. temperature, density, etc.) within the 2D thread (see Figs. 3.2 and 3.3). As was shown by Heinzel et al. (2005 - Sect. 5.1), the emerging intensity from such 2D thread models also strongly varies when viewed across the length of the fine-structure thread. Therefore the total radiative output of an ensemble of such 2D threads is considerably affected by the arrangement of these threads. The effect of different thread arrangements on shapes of the synthetic Lyman line profiles was studied by Gunár et al. (2007b - Sect. 5.5).

The multi-thread models of Gunár et al. (2007b) consists of sets of the 2D promi-

nence fine-structure threads placed perpendicularly to the line-of-sight in random positions (Fig. 4.2). The threads are assumed to be identical and without mutual radiative interaction. The total emerging intensity for a given wavelength can be described by the formula

$$I_{\mathrm{total}} = I_{\mathrm{P_1}} + \exp(-\tau_{\mathrm{P_1}}) \times I_{\mathrm{P_2}} + ... + \exp\left(-\sum_{1}^{N-1} \tau_{\mathrm{P_i}}\right) \times I_{\mathrm{P_N}} \tag{4.31}$$

where $I_{\mathrm{P_1}}$ represents the intensity from the given position on the first thread. The thread i ($i > 1$) is randomly shifted with respect to the first thread, $\mathrm{P_i}$ represents the position along the length of the thread i which is on the same line-of-sight as the given position on the first thread and $I_{\mathrm{P_i}}$ represents the intensity emerging from position $\mathrm{P_i}$. $\tau_{\mathrm{P_1}}$ is the optical depth at the given position along the first thread and $\tau_{\mathrm{P_i}}$ ($i > 1$) represents the optical depth at the position $\mathrm{P_i}$ along the thread i. N represents the total number of the threads.
The summary of results of such random multi-thread modelling is given in Sect. 5.5.

V. Results and publications

This chapter provides the summary of the research work carried out by S. Gunár.

The research work of S. Gunár carried out during his doctoral studies at the Charles University in Prague is presented in this chapter. The majority of this work is already published or accepted for publication in international journals or conference proceedings. Therefore the chapter is designed as an ensemble of the publication summaries with the publications themselves enclosed as Appendixes A to E.

S. Gunár has carried out his research work at the Astronomical Institute of the Academy of Sciences in Ondřejov, under the supervision of Ass. Prof. Petr Heinzel, DSc. The publications presented here were produced in collaboration with U. Anzer (Max-Planck-Institut für Astrophysics, Garching), B. Schmieder (Observatiore de Paris - Section de Meudon) and several other coauthors (P. Schwartz - Asu AV ČR, Ondřejov, L. Teriaca and U. Schühle - Max-Planck-Institut für Sonnensystemforschung, Katlenburg-Lindau).

The presented research work has been devoted to the study of the multi-dimensional radiative transfer in the fine structures of the quiescent prominences.

In the following sections we present, in the chronological order, the principal results of our publications included in the thesis.

5.1 Prominence fine structures in a magnetic equlibrium: II. A grid of two-dimensional models

P. Heinzel, U. Anzer and S. Gunár 2005
Astron. Astrophys., **442**, 331
(HAG - Appendix A)

Based on the 2D vertical-thread models of the prominence fine structures presented in Heinzel & Anzer (2001) a grid of 18 models was constructed. These models represent the prominence fine structures as vertically infinite threads in MHS equilibrium of the Kippenhahn- Schlüter type which was generalized into 2D by Heinzel & Anzer (2001). The detailed description of the MHS equilibrium equations is given in Sect. 3.2.
The 2D radiative transfer is consistently solved together with the MHS equilibrium using the Accelerated Lambda Iteration technique (Auer & Paletou 1994) with the short characteristics method to obtain the formal solution along the individual rays (Sect. 4.5). In order to obtain the higher members of the hydrogen Lyman series the 12-level plus continuum hydrogen model atom (Heinzel et al. 1997) is used instead of the 5-level plus continuum model atom initially used by Heinzel & Anzer (2001). The differences between Lyman line profiles obtained using 5-level and 12-level plus continuum model atom are shown in HAG Figs. 1 and 2. The partial redistribution (PRD) plays an important role for the ionization of the hydrogen and affects the line intensities of the strongest resonance lines. Therefore PRD was considered for the Lyman-α and Lyman-β lines in our modelling.
The geometrical grid describing the variations of the physical quantities on the horizontal $x-y$ cross-section of the fine-structure thread is fixed in the y-direction with a logarithmic spacing and adaptive in the x-direction with a linear spacing. The steps along the x-axis are obtained by transformation from the column-mass m-scale used for the computations of the MHS equilibrium (see Sects. 3.1 and 3.2). This transformation requires the integration (Eq. 3.23) which depends on the local density and therefore on the ionization degree (see Eq. 3.30). The iterative method using the adaptive MHS grid used in HAG was suggested by Heinzel & Anzer (2003) and we give its brief description at the end of Sect. 3.2. Typically 5 iterations are sufficient for the determination of the x-scale of the models specified in HAG.

Grid of models

The grid of 18 prominence fine-structure thread models was constructed in order to describe the dependence of the synthetic profiles on given input parameters. The parameters which varied within the grid are the maximum column density

Models of series $\boldsymbol{A}$ $\gamma_1 = 5$ $\gamma_2 = 30$	Models of series $\boldsymbol{B}$ $\gamma_1 = 10$ $\gamma_2 = 60$	Models of series $\boldsymbol{C}$ $\gamma_1 = 10$ $\gamma_2 = 30$	M_0 [g cm^{-2}]	$B_x(0)$ [Gauss]
$\boldsymbol{A}_1$	$\boldsymbol{B}_1$	$\boldsymbol{C}_1$	2.10^{-4}	8.4
$\boldsymbol{A}_2$	$\boldsymbol{B}_2$	$\boldsymbol{C}_2$	5.10^{-5}	4
$\boldsymbol{A}_3$	$\boldsymbol{B}_3$	$\boldsymbol{C}_3$	2.10^{-5}	2
$\boldsymbol{A}_{3\_1}$	$\boldsymbol{B}_{3\_1}$	$\boldsymbol{C}_{3\_1}$	2.10^{-5}	10
$\boldsymbol{A}_4$	$\boldsymbol{B}_4$	$\boldsymbol{C}_4$	5.10^{-6}	1
$\boldsymbol{A}_{4\_1}$	$\boldsymbol{B}_{4\_1}$	$\boldsymbol{C}_{4\_1}$	5.10^{-6}	5

Table 5.1: Input parameters for the model grid

M_0, the horizontal field in the middle of the thread $B_x(0)$ and the exponents γ_1 and γ_2. The other input parameters (temperatures in the center of the thread T_0 and at its boundary $T_{\rm tr}$, the width of the thread 2δ, the boundary pressure p_0 and the exponent γ_3) are fixed for all models, with the values:

$T_0 = 8000$ K; $T_{\rm tr} = 50000$ K; $2\delta = 1000$ km; $\gamma_3 = 2$; $p_0 = 0.03$ dyn cm^{-2} .

The model grid consists of three series with 6 models for each of them. The series differ only in the value of one of the γ-parameters. The models in each series have different values of M_0 and $B_x(0)$. The full list of the model grid is given in Tab. 5.1.

Dependence on the field orientation

As was suggested already by Heinzel et al. (2001), the shape of the Lyman line profiles strongly depends on the viewing angle with respect to the magnetic field orientation. This corresponds to different shapes of the PCTR.
The synthetic Lyman lines obtained by 2D modelling exhibit a similar behaviour as the observed Lyman line profiles. As shown in HAG, the Lyman-α profiles are rather similar when viewed along and across the magnetic field lines (along the x-axis and the y-axis of the fine-structure thread). However, all the other synthetic Lyman lines are in general much more reversed when viewed across the magnetic field lines than when viewed along the field. This trend becomes more pronounced with higher Lyman lines. In Fig. 5.1 we show the Lyman-β, Lyman-γ and Lyman-6 line half-profiles on the left and the plots of the intensity variation along the x-axis on the right. On the left the full red lines result from averaging along the thickness of the fine-structure threads 2δ (i.e. averaged profiles over the y-dimension), dashed yellow lines represent averaging along the length of the thread (i.e. along the whole x-dimension). Already the Lyman-γ

profile seen along the magnetic field is purely in emission while across the field we obtain reversed profiles. The reversal of the profiles seen across the field is even more visible on the intensity variation plots on the right hand side of Fig. 5.1. We show here the half-profiles obtained across the magnetic field at the different positions along the x-dimension. The half of the length of the thread is shown from the front (first column) and from the rear (second column).

The explanation of the magnetic field orientation effect on the synthetic Lyman line profiles is given in HAG Sect. 5, together with the description of the dependence of the synthetic profiles on the temperature and the density structures. The contribution functions (HAG Sect. 4) are used for the analysis of the formation depths of the Lyman lines.

The results of HAG were presented as a poster on the *11th European Solar Physics Meeting*, Leuven, 2005, and published in the conference proceedings (Gunár et al. 2005a). The 2D prominence fine structure modelling was also presented by S. Gunár on the *14th Annual Conference of Doctoral Students - WDS 2005*, Prague and published in the conference proceedings (Gunár et al. 2005b).

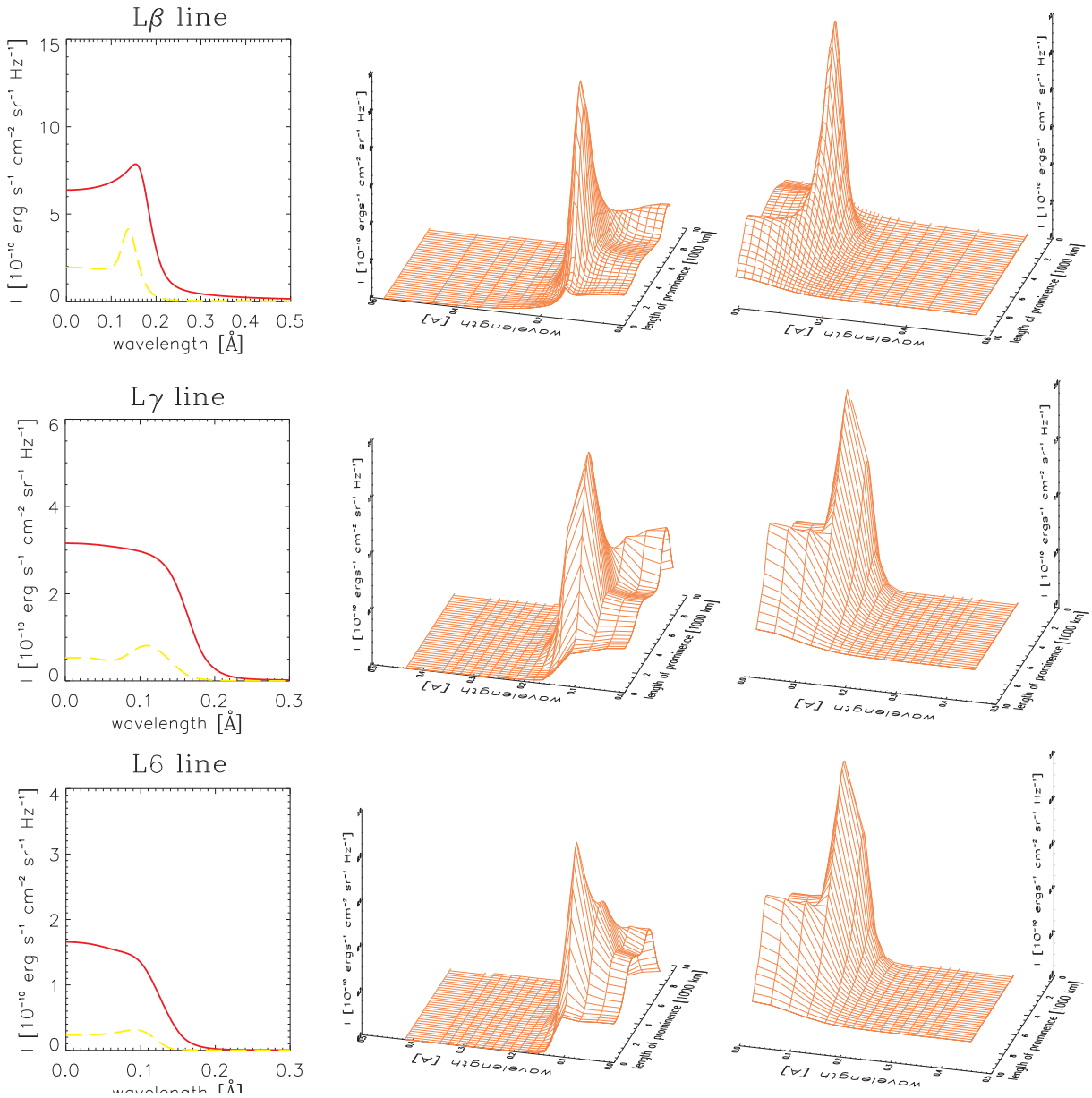

Figure 5.1: On the left hand side are the half-profiles of the Lyman-β, Lyman-γ and Lyman-6 lines. The full red lines are averaged profiles over y-dimension, dashed yellow lines represent averaging along the whole x-dimension). On the right are the intensity variation plots of the half-profiles obtained across the magnetic field at the different positions along the x-dimension. The half of the length of the thread is shown from the front (first column) and from the rear (second column).

5.2 Prominence parameters derived from hydrogen Lyman-α profiles measured by SOHO/SUMER

S. Gunár, L. Teriaca, P. Heinzel and U. Schühle 2006
in *SOHO 17 - 10 Years of SOHO and Beyond*, eds. H. Lacoste, L. Ouwehand, ESA SP-617
(GTHS - Appendix B)

The present section gives the summary of the paper Gunár et al. (2006 - GTHS) published in the proceeding of the *SOHO 17 meeting - 10 Years of SOHO and Beyond*, Giardini-Naxos, Italy, 2006. This work was presented as a poster.

The comparison of the synthetic Lyman-α profiles with the Lyman-α profiles observed by SOHO/SUMER is presented. The direct observations of Lyman-α outside the attenuator were allowed on the SUMER spectrograph only recently. Thus the Lyman-α raster presented here represents a unique opportunity to study the thermodynamical properties of the prominence fine structures using this spectral line. The observed data obtained on Apr. 18, 2005, consist of the 76×50 pixels (85" × 50") raster of the Lyman α (1215.67 Å) and Si III (1206.51 Å) lines. The observed area is centered at the solar coordinates $X = 1001", Y = 200"$ inside a large prominence shown in the He II 304 Å image (Fig. 5.2) from EIT at the day of the observation.
For the analysis of the observed Lyman lines by comparison with the synthetic spectrum obtained by 2D prominence fine-structure modelling it is necessary to use the observed profiles which have symmetrical shapes (our models are purely static). Such profiles occur in the observed raster in small clustered locations (3 to 5 pixels close to each other). Four such small clusters of the symmetrical profiles were selected for the spectroscopical analysis. Within each area 1, 5, 7 and T (T - denotes a bright vertical thread) the individual profiles were averaged and such averaged profiles were used for the comparison with the synthetic Lyman-α profiles. In Fig. 5.3 we show the positions of these areas (1,5,7,T) on the raster image.

As suggested by Heinzel et al. (2001) and shown in Heinzel et al. (2005 - HAG), the orientation of the magnetic field with respect to the line-of-sight has a considerable effect on the shape of the Lyman line profiles. Even though the effect on the Lyman-α line is not so pronounced it is possible to have at least an estimate of the magnetic field orientation in the prominence. Such an independent estimate can be obtained by the analysis of the filament on the disk observed before/after the prominence had appeared on the limb. The study of the ground-based observations of the filament between Apr. 13 to Apr. 18, 2005, showed that the SUMER prominence from Apr. 18, 2005, were observed more-or-less along the

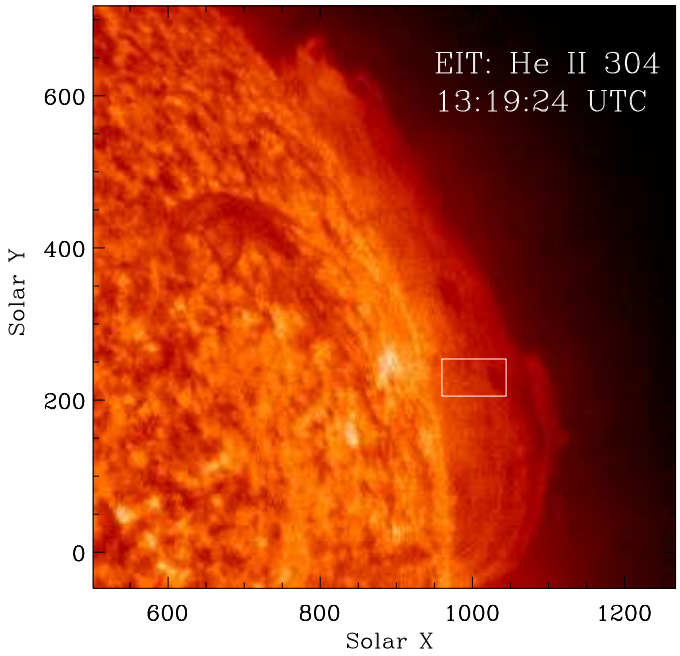

Figure 5.2: Position of the raster in the image from the EIT in the He II 304.

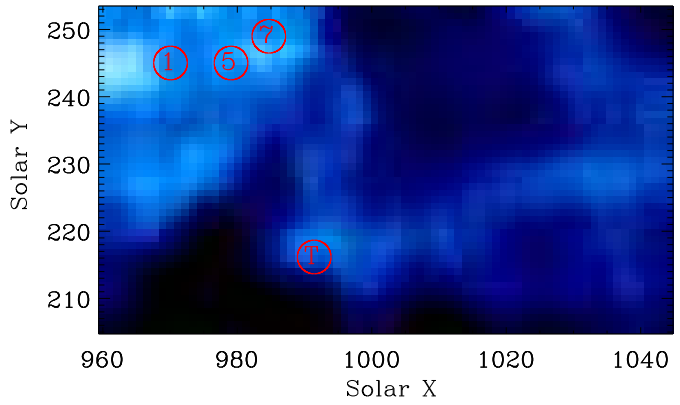

Figure 5.3: Raster image of the 85" × 50" (76× 50 pixels) area centered at solar coordinates $X = 1001", Y = 200"$. Red circles indicate the four areas (1, 5, 7, T) within which small clusters of pixels where chosen to yield the analysed line profiles.

Area	T_0 [K]	M_0 [g cm^{-2}]	$B_x(0)$ [Gauss]	p_0 [dyn cm^{-2}]	v_t [$\times$ c_s]
1	8000	8.10^{-5}	6	0.03	0.8
5	6000	5.10^{-5}	4	0.025	0.8
7	6000	5.10^{-5}	4	0.035	0.8
T	8000	$1.6.10^{-5}$	2	0.03	0.4

Table 5.2: List of the input parameters for each area on the raster.

magnetic field lines.
Such an estimate represents and important constraint on the fitting of the observed Lyman-α profiles by the synthetic ones. The trial-and-error method was used to find the synthetic Lyman-α profiles having the best agreement with the observed profiles. Starting with the grid of 18 fine-structure models presented in HAG and by varying of the input parameters, one 2D model was found for each area of the Lyman-α raster (1, 5, 7, T). The list of the models with the values of the input parameters is given in Table 5.2. Exponents γ_1 and γ_2 are equal to 5 and 30, respectively. The plots of the observed and the synthetic Lyman α line profiles are shown in Fig. 5.4. The orange lines represent the synthetic profiles and the black lines are the observed Lyman α profiles with plotted error bars.

The observed Lyman-α raster was provided by L. Teriaca and U. Schühle from the Max-Planck Institute for Solar System Research, Katlenburg-Lindau, Germany.

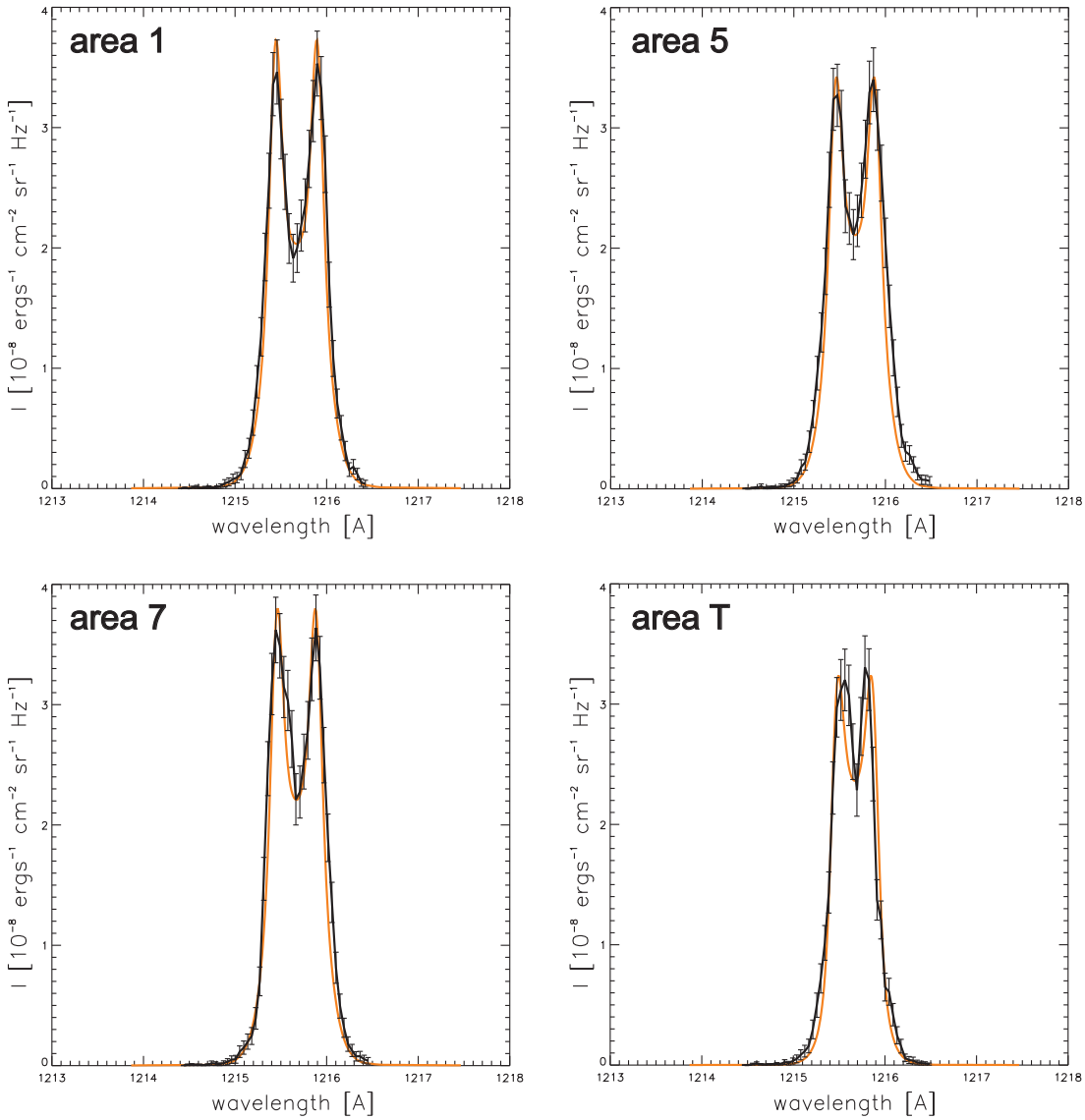

Figure 5.4: Lyman α profiles for each area on the raster (1, 5, 7, T). The orange lines represent the synthetic profiles, the black lines are observed Lyman α profiles with plotted error bars.

5.3 Prominence fine structures in a magnetic equlibrium: III. Lyman continuum in 2D configurations

Gunár, S., Heinzel, P. & Anzer, U. 2007a
Astron. Astrophys. **463**, 737
(GHA - Appendix C)

We present here another paper of the series *Prominence fine structures in a magnetic equilibrium.*

The previous paper of this series (HAG) was focused on the analysis of the Lyman lines and does not include any discussion of the Lyman continuum behaviour. The present paper (GHA) concerns the study of the Lyman continuum formation and its dependence on the varying plasma conditions. This study is again based on the grid of 18 two-dimensional prominence fine-structure models introduced in Heinzel et al. (2005). The MHS equilibrium equations and the methods of 2D radiative transfer computations are described in Sects. 3.2 (MHS) and 4.5 (2D RT).

Effect of different temperature structure

The temperature structure of the 2D prominence threads is characterized by two considerably different parts of the PCTR. Across the magnetic field lines the transition region is very thin with a steep temperature gradient. On the other hand, the temperature along the magnetic field is rising gradually from the cool fine-structure thread center up to the boundaries of the thread. Such different conditions are caused by the difference in the thermal conductivities of the plasma along and across the magnetic field. This has an essential effect on the shape of the Lyman line profiles. As was shown by Heinzel et al. (2005) the synthetic profiles observed across the magnetic field lines exhibit much more reversed shapes than the profiles observed along the field. The temperature profile used in the 2D models developed by Heinzel & Anzer (2001) is given empirically rather than by solution of the energy balance and it is described by the Eqs. (3.20) and (3.21). The temperature gradients are determined by the choice of the exponents γ_1 and γ_2, where γ_2 characterizes the steep gradient across the magnetic field and γ_1 the gradual rise of the temperature along the field.
The contribution functions described in Heinzel et al. (2005), Sect. 4 are used for the determination of the formation depths of the Lyman lines and continuum. As it is clear from Figs. 5.6 and 5.7, the Lyman continuum observed across the field lines is formed in the regions deeper in the fine-structure thread. Therefore the choice of the parameter γ_2, which describes the thin PCTR across the magnetic field does not have any influence on the shape of the Lyman continuum.

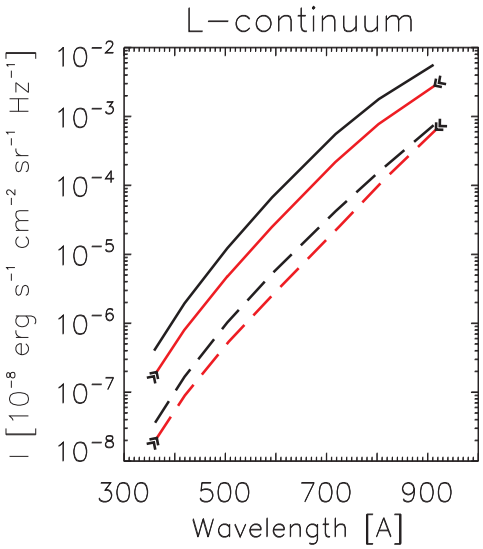

Figure 5.5: Lyman continuum for models $\boldsymbol{A}_1$ and $\boldsymbol{C}_1$. Full lines represent averaged profiles over the width of the thread, dashed lines are mean profiles over the whole length of the thread. Double-arrowed lines belong to the model $\boldsymbol{C}_1$.

On the other hand, the Lyman continuum obtained along the field lines is formed inside the elongated PCTR and thus the choice of the γ_1 exponent has a significant effect on the Lyman continuum profiles. This effect was studied on two models from the grid of the models (Table 5.2) which differ only in the value of the parameter γ_1 ($\boldsymbol{A}_1(\gamma_1 = 5)$ and $\boldsymbol{C}_1(\gamma_1 = 10)$). The Lyman continuum profiles for these two models are shown in Fig. 5.5. Here the full lines represent averaged profiles over the width of the thread (profiles seen along the field lines), the dashed lines are the mean profiles over the whole length of the thread (seen across the field lines). Double-arrowed red lines belong to model $\boldsymbol{C}_1$. The main difference between the Lyman continuum profiles for models $\boldsymbol{A}_1$ and $\boldsymbol{C}_1$ lies in the value of the specific intensity at each wavelength. As shown in Fig. 5.5, the specific intensity for model $\boldsymbol{A}_1$ is almost twice higher than for model $\boldsymbol{C}_1$, while the difference between the two directions of view is almost one order of magnitude. For the detailed interpretation of these calculations using the contribution functions see GHA.

Let us now describe the contribution functions used for the analysis of the Lyman continuum formation depths. We show here two panels of plots of contribution functions for models $\boldsymbol{A}_1$ and $\boldsymbol{C}_1$ for the wavelengths of 911 Å (Fig. 5.6) and 717 Å (Fig. 5.7). Each plot shows the spatial variation of the contribution to the specific intensity for a given wavelength as a function of the geometrical position. The white regions represent major contributions, the black ones are regions with minor contribution. The panel plots for given wavelengths are organized as follows: the first four plots are for model $\boldsymbol{A}_1$, the second four for model $\boldsymbol{C}_1$.

The upper pair of plots represents viewing along the field lines (from the *left side* in the plots, marked as x-direction according the geometry of the thread), the lower pair represents viewing across the field lines (from the *bottom* in the plots, marked as y-direction). On the left-hand side the contribution functions are overplotted with iso-lines of the temperature (contours represent 9000, 10000, 12000, 15000, 20000, 30000, and 40000 K starting at the center of the thread). On the right-hand side are the iso-lines of the density for 0.25, 0.5, 1.0, 1.5, 2.0, and 2.5 10^{-13}g cm^{-3} starting at the boundaries of the thread. The bold red dashed contour represents the level of the optical depth of $\tau = 1$ at the selected wavelength. Note that these figures are not drawn to the true scale (they are squeezed in the x-direction).

Direct comparison of Figs. 5.6 and 5.7 shows that for the wavelengths from 911 Å to 803 Å the contribution to the Lyman continuum mainly comes from the innermost parts of the PCTR and from the cool prominence interior and it is centered around the $\tau = 1$ line. The location of the regions with the maximum contribution strongly depends on the viewing direction with respect to the magnetic field orientation. In the case that the line-of-sight is oriented along the field lines, the Lyman continuum within the wavelength range 911 Å to 803 Å is formed in the extended PCTR with the increase of the temperature described by the exponent γ_1 in the area with the temperatures between 10000 to 15000 K. When seen across the field lines the place of the formation is in the central (coolest) part of the fine-structure thread. At the wavelengths around 718 Å, and even more pronounced at lower wavelengths, the emission basically comes from the hotter parts of the PCTR and the region is spatially much more extended. In these cases the Lyman continuum comes from the regions in front of the $\tau = 1$ line (i.e., optically thin regions).

The investigation of GHA shows that the interpretation of the Lyman continuum in terms of a mean temperature of the contributing region is plausible only for the part of the Lyman continuum spectrum between 911 Å and 800 Å. However, special attention should be devoted to the fact that the value of the mean temperature of the contributing region strongly depends on the angle between the line-of-sight and the magnetic field. From Fig. 5.6 it is clear that the contribution comes from a region with the temperature between 10000 to 15000 K when viewed along the field lines and from regions with the temperature slightly higher than 8000 K when looking perpendicularly to the magnetic field lines. Therefore the temperatures derived by making spectral fits to the observations (e.g. Parenti et al. 2005) will be strongly dependent on the fine structures and the viewing angle. But in all cases the temperature derived on this basis will lead to upper limits for the true central prominence temperature.

This work was performed during S. Gunár EARA-EST fellowship at the Max-Planck-Institut für Astrophysik (from Jan. to Apr. 2006) under the local supervision of U. Anzer. The observed data were provided by S. Parenti, based on the

paper by Parenti et al. (2005).

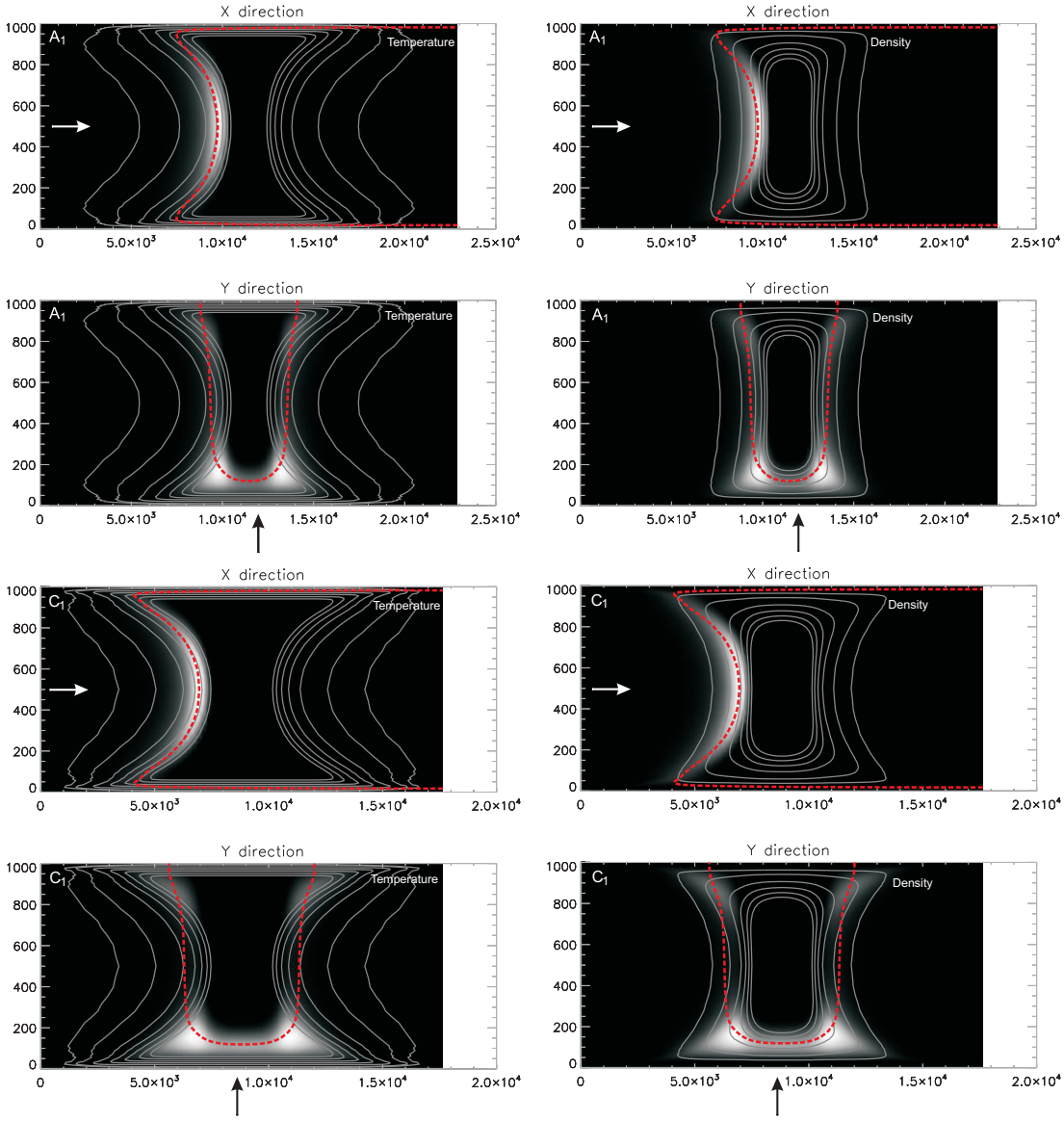

Figure 5.6: Contribution function for the Lyman continuum at the wavelength 911 Å for models $\boldsymbol{A}_1$ (the first four plots) and model $\boldsymbol{C}_1$ (the second four plots). The upper pair of the plots for each model represents the viewing along the field lines (from the *left side*), the lower pair represents the viewing across the field lines (from the *bottom*). On the left-hand side iso-contours of the temperature (9000, 10000, 12000, 15000, 20000, 30000, and 40000 K) and on the right-hand side iso-contours of the density (0.25, 0.5, 1.0, 1.5, 2.0, and 2.5 10^{-13}g cm^{-3}) are shown. The bold red dashed line represents the contour of $\tau(911) = 1$

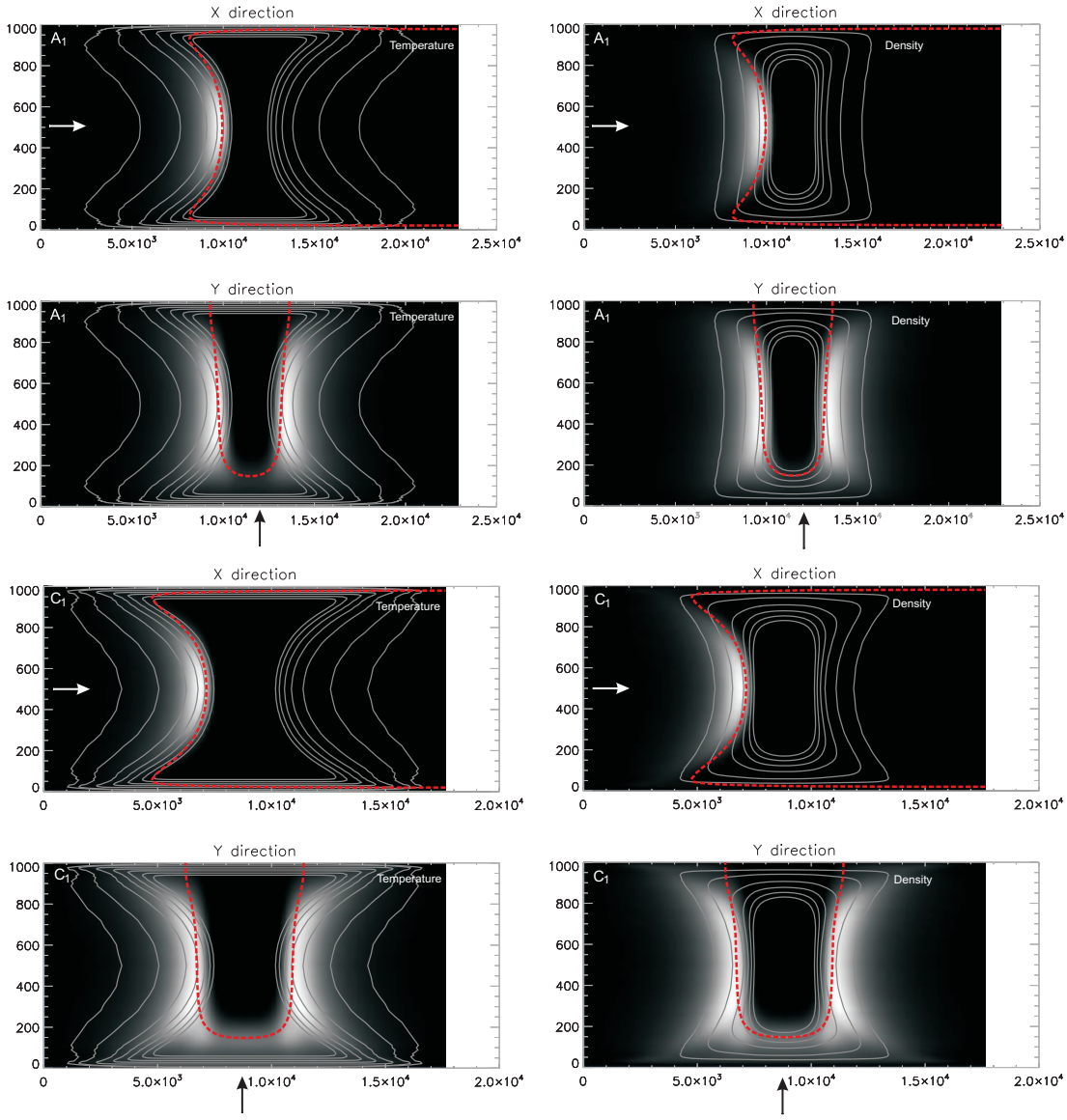

Figure 5.7: Same as in Fig. 5.6 but at the wavelength 717 Å.

5.4 Spectral diagnostics of the magnetic field orientation in a prominence observed with SOHO/SUMER

Schmieder, B., Gunár, S., Heinzel, P. & Anzer, U. 2007
Solar Phys., **241**, 53
(SGHA - Appendix D)

HAG showed the importance of the magnetic field orientation with respect to the line-of-sight for the formation of the Lyman lines originally suggested by Heinzel et al. (2001). To support these results observationally, SGHA focused on the prominence which occurred during three consecutive days as a *round-shape filament* was crossing the limb.
Three prominence observations during JOP 107 on Oct. 15 - 17, 1999, represent three different parts of one round-shape filament with presumably different angles between the magnetic field lines and the line-of-sight. The round shape filament consecutively crossing the limb and the prominence parts observed above the limb are shown in Fig. 5.8. The round shape filament consists of four different sections F1 to F4 indicated in Fig. 5.8 on the second panel in the right column.
Two different methods were used to derive the orientation of the magnetic field in the prominence. The morphological analysis using the observations of the filament and the spectral diagnostics using the comparison of the observed SUMER spectrum with the synthetic spectral lines obtained by 2D fine-structure modelling.
The morphological analysis is based on the study of the magnetic field orientation with respect to the main filament axis by Aulanier and Démoulin (2003). Using the deductions from the observations of the round-shape filament, the prominence observed on Oct. 15 is formed by section F1 and the line-of-sight is more-or-less along the magnetic field (and thus along the x-axis of the 2D thread models). The prominence observed on Oct. 16 consists of sections F2 and F3, but the SUMER observed the section F3 with the magnetic field perpendicular to the line-of-sight and on Oct. 17 the section F4 is observed as a prominence with the line-of-sight along the magnetic field.
The comparison of the observed SUMER spectrum with the synthetic profiles was performed on the basis of the grid of 18 models of Heinzel et al. (2005). The Lyman-δ profiles from the raster obtained by SUMER on Oct. 16 and 17 were qualitatively compared with the synthetic Lyman-δ profiles. The models with the best agreement between the synthetic and the observed profiles were found within the grid of 18 fine-structure models. Figures 5.9 and 5.10 show the observed Lyman-δ rasters on Oct. 16 and 17 together with the profiles averaged along the raster. Figure 5.11 shows the synthetic Lyman-δ profiles for model $\boldsymbol{C}_2$ obtained across the magnetic field lines and for model $\boldsymbol{C}_4$ obtained along the field lines. These results correspond with the morphological analysis of the magnetic

field orientation where the spectrum observed on Oct. 16 belongs to the section F3 and the spectrum observed on Oct. 17 to the section F4. Note that a comparison of the observed and synthetic profiles is only qualitative, no exact fitting was performed. Any quantitative fitting would require much more extensive 2D modelling, involving much larger grid of models which is very time-consuming. This study of the round-shape filament represents a unique opportunity to perform two fundamentally different analyses of the magnetic field orientation in the prominence. The correspondence of the results obtained by different methods supports the idea that the shape of the Lyman lines provides a useful tool for the diagnostics of the magnetic field orientation within the prominence.

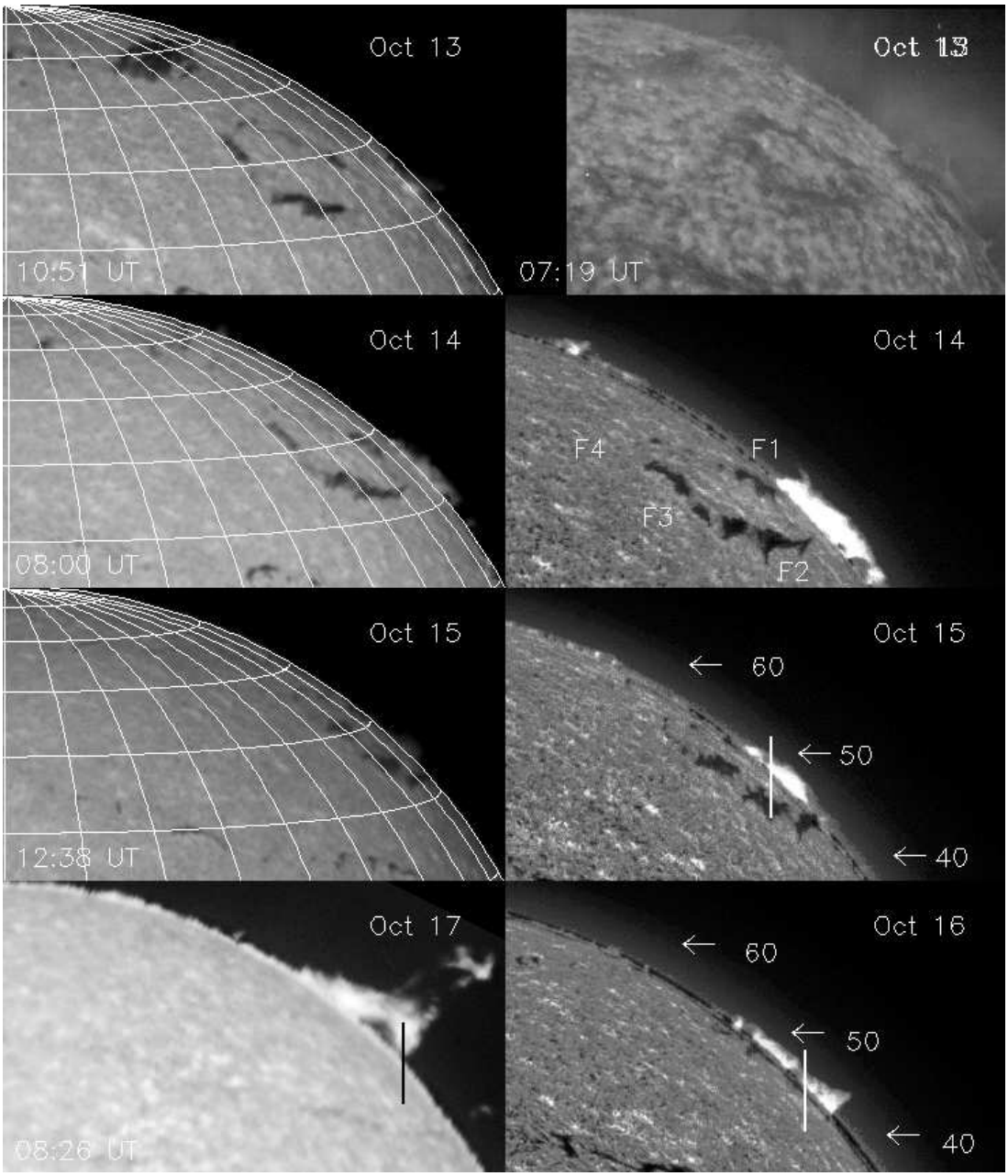

Figure 5.8: The round-shape filament and prominences F1, F2, F3 and F4 on Oct. 13 to 17, 1999. In the left column are Meudon Hα spectroheliograms on Oct, 13, 14 and 15 (rows 1, 2 and 3) with superposed heliographic coordinate grids. In the right column on the top is an observation with the SOHO/EIT at 304 Å at 07:19 UT and next three panels represent the BBSO observations in Hα. In the last row on the left panel is Meudon Hα image on Oct. 17 . The vertical lines indicate the position of the SUMER slit.

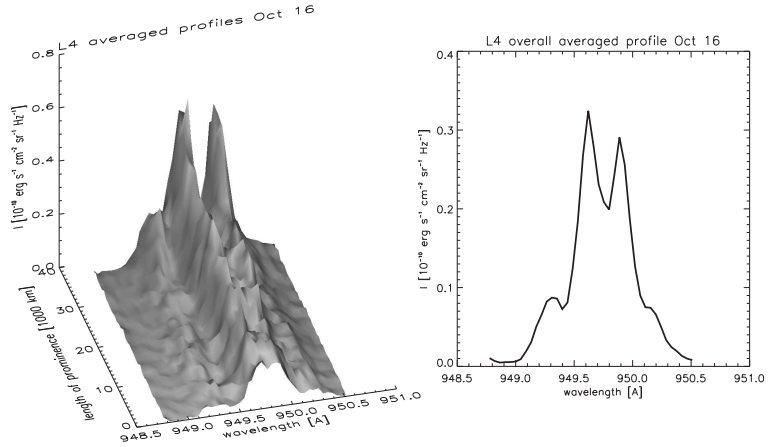

Figure 5.9: Lyman δ observed on Oct. 16. Surface plot on the left shows the line variation along the raster. On the right is the averaged profile along the raster.

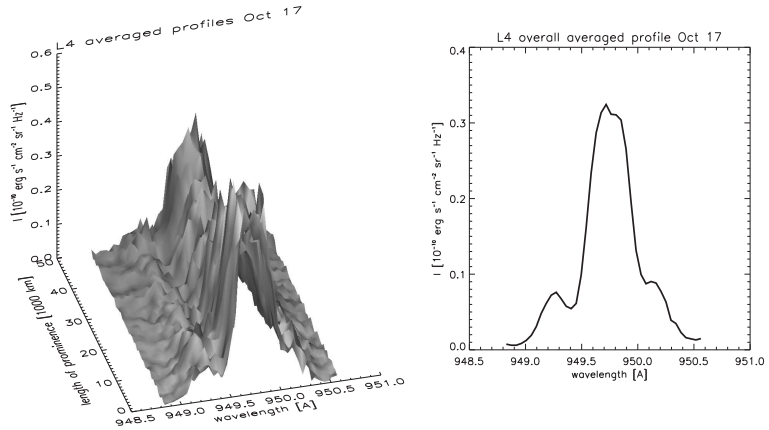

Figure 5.10: Lyman δ observed on Oct. 17. Surface plot on the left shows the line variation along the raster. On the right is the averaged profile along the raster.

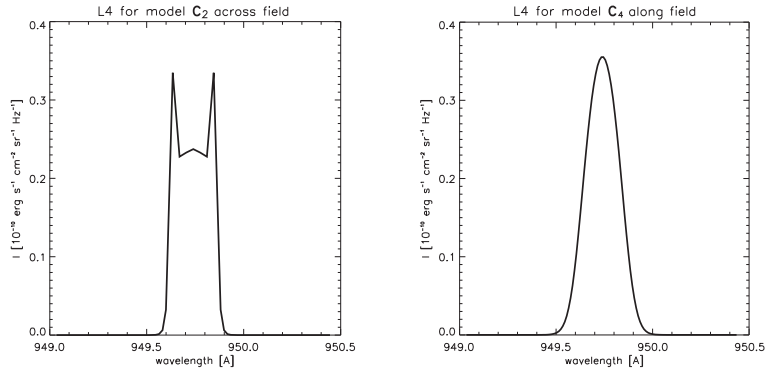

Figure 5.11: Lyman δ profiles of models $\boldsymbol{C}_2$(on the left) and $\boldsymbol{C}_4$(on the right).

5.5 Properties of prominence fine-structure threads derived from SOHO/SUMER hydrogen Lyman lines

Gunár, S., Heinzel, P., Schmieder, B., Schwartz, P. & Anzer, U. 2007b
Astron. Astrophys. **472**, 929
(GHSSA - Appendix E)

We present here the summary of the spectroscopic analysis of the SOHO/SUMER observations using the comparison of the observed hydrogen Lyman lines with the synthetic Lyman line profiles obtained by 2D prominence fine-structure modelling (Gunár et al. 2007b).

First SOHO/SUMER observations of the prominence spectrum in the Lyman-α line outside the attenuator together with higher members of the hydrogen Lyman series are used for the derivation of the prominence fine-structure physical properties. The SUMER spectrum was obtained on May 25, 2005, during the MEDOC coordinated campaign between the SOHO and the ground-based instruments (MEDOC campaign No. 15, May 16 to 29, 2005). The SUMER slit was pointed at the solar coordinates $X = 972$" and $Y = 168$". The observed spectrum used in GHSSA consists of the Lyman-α to Lyman-7 lines with exception of Lyman-5. Their observations were carried out in time steps of approximately two minutes as follows: Lyman-α observations began at 19:10:03 UT, Lyman-β at 19:12:23 UT, Lyman-γ and Lyman-δ at 19:14:32 UT and Lyman-6 to Lyman continuum at 19:16:44 UT. Only symmetrical profiles were selected for the comparison with the synthetic spectrum. Such profiles occur in the observational data in small clustered locations of up to 3 pixels close to each other. The averaging over such an area helps to avoid errors due to the possible presence of the velocity gradients and reduce the noise.
In order to obtain the synthetic spectrum, our 2D prominence fine-structure models were used. The observed Lyman lines exhibit the reversed shapes also for higher lines of the Lyman series and therefore this spectral analysis is focused only on the synthetic profiles obtained across the magnetic field lines. As was shown in Heinzel et al. (2005), the synthetic Lyman line profiles show rather significant shape and intensity variations at different positions along the length of the prominence thread. Therefore special attention should be devoted to the treatment of the profiles emerging from different positions along the x-axis when compared with the observed profiles.
To obtain a model with the best agreement between the observed and synthetic Lyman line profiles we used a trial-and-error approach beginning with the grid of 18 models of Heinzel et al. (2005). Such a model was identified by varying the input parameters and comparing the synthetic profiles, emerging from different positions along the length of the thread, with the observed Lyman line profiles.

The values of the input parameters of the resulting model are: the central (minimum) temperature $T_0 = 7000$ K, maximum column mass in the centre of the thread $M_0 = 1.1 \times 10^{-4}$ g cm^{-2}, horizontal field strength in the middle of the thread $B_x(0) = 6$ Gauss, and the boundary pressure $p_0 = 0.015$ dyn cm^{-2}.
Figure 5.12 shows the comparison of the observed Lyman lines with the synthetic profiles. The full lines with overplotted error bars represent the observed data and the dot-dashed lines represent the synthetic profiles emerging from the indicated positions along the length of the thread. The position along the thread from which the given synthetic profiles emerge is indicated by the number in the title. The position in the centre of the thread has the number 42 and the boundaries of the thread have numbers 0 and 82 (this corresponds to the number of grid points along the x-axis). 2D prominence fine-structure model is capable to plausibly reproduce the observed Lyman-α to Lyman-δ lines but fails to reproduce the higher Lyman lines. Another problem is the width of the synthetic spectral lines which is too small in comparison with the observed ones while the central parts of the lines are in good agreement. Better results can be obtained using the multi-thread modelling (Sect. 4.6).
The multi-thread prominence fine-structure models consist of sets of the 2D threads placed perpendicularly to the line-of-sight in random positions (Fig. 4.2). The threads are assumed to be identical and without any radiative interaction between them. The emerging intensity is integrated along the line of sight. For this study random distributions of ten prominence fine-structure threads were used. Each random arrangement produces different synthetic Lyman line profiles. The resulting profiles are shown in Fig. 5.13 where the full lines with overplotted error bars represent the observed profiles. The gray full lines show one hundred randomly arranged multi-thread models and the dot-dashed lines are the profiles emerging from the first thread only. The position along the first thread is marked in the title of each plot. The area within the gray profiles covers the range of all emerging profiles.
The Lyman-α profile is not much affected by the multi-thread modelling (the resulting emerging profiles from multi-thread models are practically identical with the single-thread profile) and thus it is suitable for the search of the best prominence fine-structure thread model, which can be afterwards used in the multi-thread modelling. The synthetic profiles of the higher lines are wider in the line-wings and therefore in better agreement with the observed profiles. Moreover, also the Lyman-6 and Lyman-7 synthetic profiles are in agreement with observations.
Therefore, the multi-thread approach to the modelling of the prominence fine structures reproduces the observed Lyman line profiles better than the single-thread modelling. This is furthermore supported by the high-resolution observations of the filaments on the disk (Fig. 1.3) with numbers of thin fibrils resembling the fine-structure threads. The possibility to reproduce simultaneously all of the Lyman-α to Lyman-7 lines gives an opportunity to determine in detail the phys-

ical properties of the prominence fine structures.

This work was carried out partially during S. Gunár EARA-EST fellowship at the Max-Planck Institut für Astrophysik (from Jan. to Apr. 2007) under the local supervision of U. Anzer. Preliminary results of GHSSA were presented by S. Gunár during the conference *The Physics of Chromospheric Plasmas*, Coimbra, Portugal, 2006 and published in the conference proceedings (Gunár et al. 2007c).

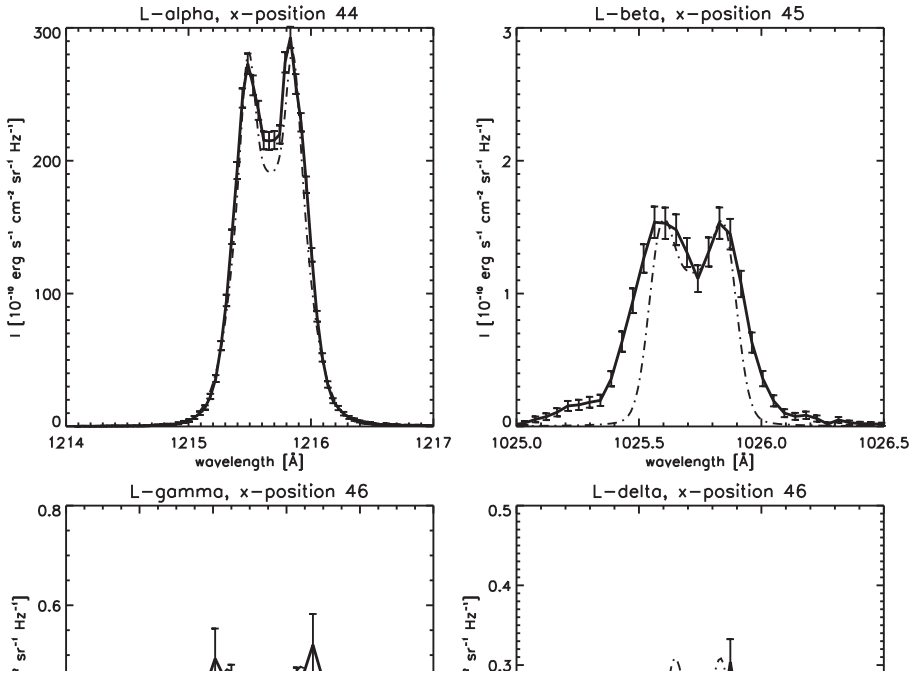

Figure 5.12: Comparison between the synthetic and the observed Lyman-α to Lyman-7 lines. Full lines with overplotted error bars represent the observed data. Dot-dashed lines represent the single-thread synthetic profiles emerging from the indicated position along the thread.

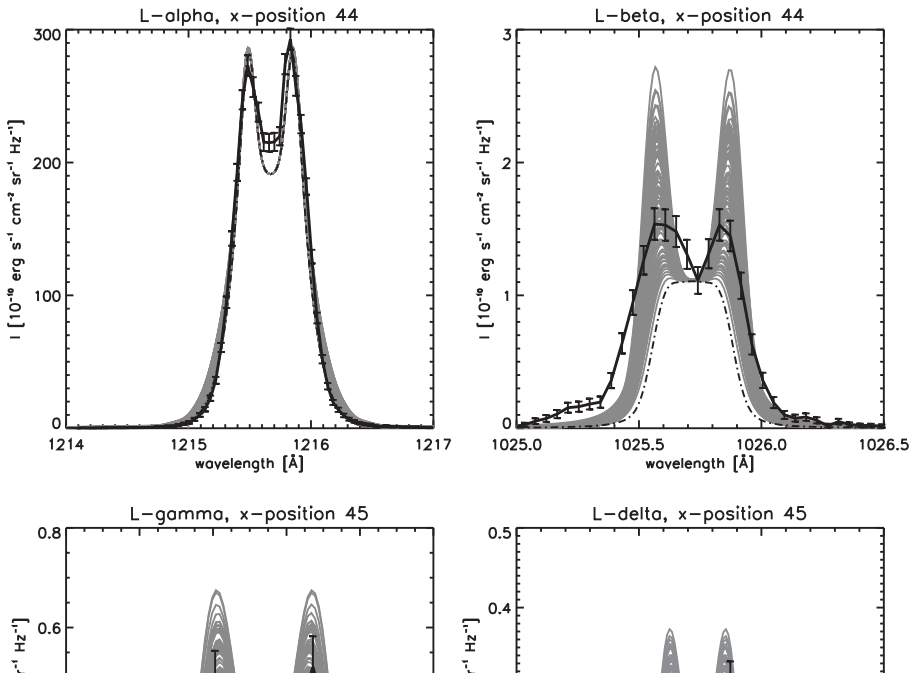

Figure 5.13: Comparison between the synthetic and observed Lyman-α to Lyman-7 lines. Full lines with overplotted error bars represent the observed profiles. Gray full lines belong to one hundred randomly arranged multi-thread models and the dot-dashed lines are the profiles emerging from the first thread from the position which is marked in the title of each plot.

VI. Conclusions

An overview of the research work in progress and future research plans are given.

In previous chapters we have summarized the research work carried out by S. Gunár during his doctoral studies together with the theoretical backgrounds necessary for understanding of the multi-dimensional radiative transfer in the prominence fine structures. The work presented so far has been published in the international journals or in the conference proceedings. In this chapter we give an overview of the ongoing work which has not yet been published and we present our plans of the future research.

The 2D prominence fine-structure models allow us to obtain the synthetic spectra with the line-of-sight oriented along and across the magnetic field lines using a single model. Thus we can study the differences of the line profiles and so analyze the effects of the orientation of the magnetic field in the fine structures of the prominences. With the employment of the multi-thread modelling we are able to reproduce well the observed Lyman lines from the Lyman-α up to such lines as the Lyman-7. Therefore we can derive the properties of the prominence fine structures using the comparison of the observed Lyman line profiles with the synthetic ones.
The next logical step is an effort to model both the prominence and filament fine structures using a single 3D model. The 2D vertical fine-structure thread models of Heinzel & Anzer (2001) and of HAG were used to estimate the Hα contrast of the dark fibrils (Heinzel & Anzer 2006). The vertical threads were artificially cut in height and the Hα contrast was computed from the top of such three-dimensional structures. The resulting dark structures resemble dark fibrils observed on the solar disk (Fig. 1.3). However, such artificial structures are no more in the MHS equilibrium.
In order to obtain the prominence/filament fine-structure models which could be used at the same time for diagnostics of the prominences and filaments and would be in required equilibrium, one has to consider 3D models. But a proper analytical solution for the MHS equilibrium in 3D does not exist. Therefore

we have chosen the 3D MHD (*magnetohydrodynamic*) numerical relaxation technique to obtain 3D prominence/filament fine-structure models in the equilibrium state. An intermediate step towards the fully 3D models in MHD-relaxed state is represented by the 2.5D prominence/filament fine-structure models.

6.1 2.5D models in MHD-relaxed state

The MHD relaxation technique used to obtain a 2.5D model in a static state is based on the work of Bárta & Karlický (2005) who solved numerically the system of the compressible one-fluid MHD equations in the 2D vertical plane. Their code, originally developed for the solution of the magnetic reconnection, was modified for purposes of the prominence fine-structure modelling (Bárta et al. 2007).
The prominence/filament fine structure is represented by a 2D horizontal thread and its projection onto the vertical plane represents a blob of dense and cool plasma surrounded by the hot corona. The plasma blob embedded into the initially horizontal magnetic field starts to fall down due to the gravity force. The internal electric current is induced inside it which generates the restoring Lorenz force. The system starts to oscillate around an equilibrium point, damped by an artificially added numerical viscous term. After several oscillations the system is practically relaxed into the MHS equilibrium. Such a relaxed 2D horizontally infinite thread can be then artificially cut in the direction perpendicular to the plane in which the 2D MHD relaxation was computed. In this way one obtains a 3D element which is in relative MHS equilibrium but due to its rather artificial origin it is rather called a 2.5D model.
The transition region between the cool plasma of the blob and the hot corona has the same characteristics as the temperature structure of the 2D vertical-thread models of Heinzel & Anzer (2001) or HAG. It is more extended along the magnetic field lines with gradually rising temperature and rather thin across the field with a very steep temperature gradient. These empirical temperature profiles are used as the initial conditions for the plasma blob. The temperature profiles after the relaxation process keep relatively similar shapes, with an elongated PCTR along the magnetic field lines and a thin PCTR layers across the field. Figure 6.1 shows the preliminary results of the 2D MHD relaxation (the PCTR layer at the bottom of the plasma blob is slightly more compressed than at top).
The same multi-level ALI technique as used in the 2D case (Sect. 4.5) can be applied also for the treatment of the 3D radiative transfer. The implementation of the 3D radiative transfer computations into the 2.5D prominence fine-structure models represents the nextresearch goal of S. Gunár. It will be performed in collaboration with P. Heinzel and U. Anzer, presumably within a post-doctoral stay at the Max-Planck-Institut für Astrophysik in Garching. Note, that the short characteristics method may prove to be more tedious to implement than the long characteristics (LC), although it is probably faster (some other authors also use

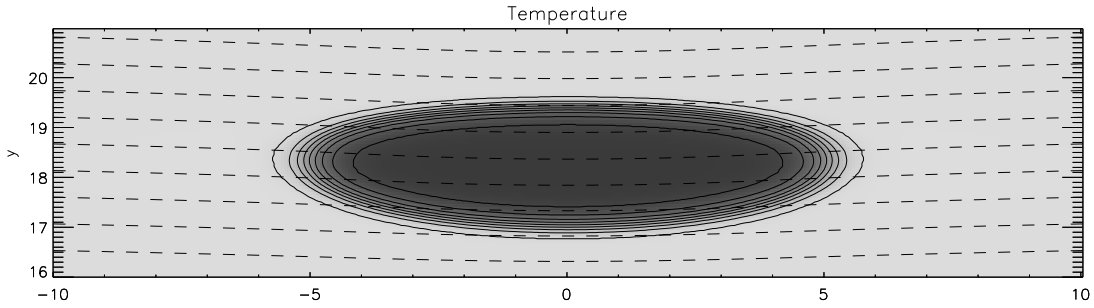

Figure 6.1: The temperature structure of the plasma blob after MHD relaxation. The temperature is drawn in gray scale with the dark parts representing the lowest temperatures. The overplotted contours also represent the temperature. The x and y axis are expressed in dimensionless units related to the initial half-width of the blob. The dashed lines represent the dipped magnetic field lines.

LC for 3D solar-atmospheric modelling). Both techniques will be tested and the most efficient one will be chosen.

6.2 Parallelization

The multi-dimensional prominence fine-structure modelling including the non-LTE radiative transfer computations is highly CPU-time-consuming. Therefore the use of the high-performance multi-CPU computers is necessary for extended modelling. However, in order to perform the computations on the cluster computers such as OCAS (cluster computer of the Astronomical Institute of the Academy of Sciences of Czech Republic in Ondřejov) one needs to parallelize the code using the MPI (*blabla*) in case of the cluster with distributed memory or OBLABLA (*blabla*) in case of the computer with shared memory.
Preliminary steps towards the parallelization of our existing 2D fine-structure code were performed by S. Gunár in collaboration with M. Bárta. The formal SC solver of the original 5-level plus continuum code was parallelized in frequencies using the MPI and the code was tested on eight CPUs of the OCAS cluster. The solution was obtained more than three times faster than using the non-parallelized version of the code. The speed-up factor will be even higher after the parallelization of the additional routines. The parallelization of the 2D code represents a preparation for intended development of the 3D radiative transfer code. The 3D radiative transfer computations are extremely CPU-time-consuming and therefore it is necessary to use the parallelization already at first stages of its development. Moreover, fast solution of even 2D prominence fine-structure models will allow us to compute vast grids of 2D models with different input parameters. This will help us to better optimize the spectroscopic analysis of the observed prominence spectra. Matching of the observed and synthetic spectrum will be

performed by a least-square searching in the already computed grids rather than using a trial-and-error method.

Bibliography

[1] Anzer, U. & Heinzel, P. 1999, *Astron. Astrophys.* **349**, 974

[2] Auer, L.H. & Paletou, F. 1994, *Astron. Astrophys.* **285**, 675

[3] Aulanier, G. & Démoulin, P. 2003, *Astron. Astrophys.* **402**, 769

[4] Bárta, M. & Karlický, M. 2005, *Astrophys. J.* **631**, 612

[5] Bárta, M., Anzer, U., Heinzel, P., & Karlický, M. 2007, in preparation

[6] Bommier, V. & Leroy, J.-L. 1998, in *New Perspectives on Solar Prominences*, eds. D. Webb, D. Rust, B. Schmieder, ASP-150, 434

[7] Cannon, C.J. 1973, *Astrophys. J.* **185**, 621

[8] Carlson, B.G. 1963, in *Methods of Computational Physics*, eds. B. Alder, S. Fernbach & M. Rottenberg, Academic Press, New York

[9] Carlsson, M. 1986, *A Computer Program for Solving Multi-Level Non-LTE Radiative Transfer Problems in Moving or Static Atmospheres*, Report No. **33**, Uppsala Astronomical Observatory

[10] Delaboudiniere, J.-P., Artzner, G.E., Brunaud, J. et al. 1995, *Sol. Phys.* **162**, 291

[11] Engvold, O. 2004, in Multi-Wavelength Investigations of Solar Activity eds. A.V. Stepanov, E.E. Benevolenskaya, A.G. Kosovichev, IAU Symposium **223**, 187

[12] Engvold, O., Hirayama, T., Leroy, J.-L., Priest, E.R. & Tandberg-Hanssen, E. 1990, *Dynamics of Quiescent Prominences*, Proc. IAU Coll. 117, Lecture Notes in Physics 363, Springer-Verlag, Berlin, 294

[13] Fleck, B., Domingo, V. & Poland, A. 1995, *The SOHO mission*, Kluwer Acad. Publ., Dordrecht

[14] Fontenla, J., Rovira, M., Vial, J.-C. & Gouttebroze, P. 1996, *Astrophys. J.* **466**, 496

[15] Gunár, S., Heinzel, P. & Anzer, U. 2005a, in *11th European Solar Physics Meeting*, eds. D. Danesy, S. Poedts, A. De Groof, J. Andries, ESA SP-600

[16] Gunár, S., Heinzel, P. & Anzer, U. 2005b, in *14th Annual Conference of Doctoral Students 2005*, ed. J. Šafránková, **3**, 463

[17] Gunár, S., Heinzel, P. & Anzer, U. 2007a, *Astron. Astrophys.* **463**, 737 (GHA)

[18] Gunár, S., Heinzel, P., Schmieder, B. & Anzer, U. 2007c, in *The Physics of Chromospheric Plasmas*, eds. P. Heinzel, I. Dorotovic, R.J. Rutten, ASP-368, 317

[19] Gunár, S., Teriaca, L., Heinzel, P. & Schühle, U. 2006, in *SOHO 17 - 10 Years of SOHO and Beyond*, eds. H. Lacoste, L. Ouwehand, ESA SP-617 (GTHS)

[20] Gunár, S., Heinzel, P., Schmieder, B., Schwartz, P. & Anzer, U. 2007b, *Astron. Astrophys.* **472**, 929 (GHSSA)

[21] Harrison, R.A., Sawyer, E.C., Carter, M.K. et al. 1995, *Sol. Phys.* **162**, 233

[22] Heasley, J.N. & Mihalas, D. 1976, *Astrophys. J.* **205**, 273

[23] Heinzel, P. 1989, in *Hvar Observatory Bulletin* **13**, 317

[24] Heinzel, P. 2007, in *The Physics of Chromospheric Plasmas*, eds. P. Heinzel, I. Dorotovic, R.J. Rutten, ASP-368, 271

[25] Heinzel, P. & Anzer, U. 2001, *Astron. Astrophys.* **375**, 1082

[26] Heinzel, P. & Anzer, U. 2003, in *Stellar Atmosphere Modelling*, eds. I. Hubeny, D. Mihalas, K. Werner, ASP-288, 441

[27] Heinzel, P. & Anzer, U. 2005, in *Solar Magnetic Phenomena*, eds. A. Hanslmeier, A. Veronig, M. Messerotti, Astrophys. Space Sci. Lib. **320**, Springer, Dordrecht, 115

[28] Heinzel, P. & Anzer, U. 2006, *Astrophys. J.* L**643**, 65

[29] Heinzel, P., Anzer, U. & Gunár, S. 2005, *Astron. Astrophys.*, **442**, 331 (HAG)

[30] Heinzel, P., Schmieder, B. & Vial, J.-C. 1997, in *Fifth SOHO Workshop Proc.*, ed. A. Wilson, ESA SP-404, 427

[31] Heinzel, P., Schmieder, B. & Vial, J. C. 2006, in *SOHO 17 - 10 Years of SOHO and Beyond*, eds. H. Lacoste, L. Ouwehand, ESA SP-617

[32] Heinzel, P., Schmieder, B., Vial, J.C. & Kotrč, P. 2001, *Astron. Astrophys.* **370**, 281

[33] Hirayama, T., Nakagomi, Y. & Okamoto, T. 1979, in *Physics of Solar Prominences*, eds. E. Jensen, P. Maltby, F.Q. Orrall, 48

[34] Hubeny, I. 1997, in *Stellar Atmospheres: Theory and Observations*, Proc. of 9*th* EADN Summer School, Eds. J.-P. De Greve, R. Blomme, H. Hensberge, Lecture Notes in Physics, Berlin, p.1

[35] Kippenhahn, R. & Schlüter, A. 1957, *Z. Astrophys.* **43**, 36

[36] Kunasz, P. & Auer, L.H. 1998, *J. Quant. Spectrosc. Radiat. Transfer* **39**, 67

[37] Kuperus, M. & Raadu, M.A. 1974, *Astron. Astrophys.* **31**, 189

[38] Leroy, J.-L., Bommier, V. & Sahal-Bréchot, S. 1984, *Astron. Astrophys.* **131**, 33

[39] Lopez Ariste, A. & Aulanier, G. 2007, in *The Physics of Chromospheric Plasmas*, eds. P. Heinzel, I. Dorotovic, R.J. Rutten, ASP-368, 291

[40] Low, B.C. & Petrie, G.J.D. 2005, *Astrophys. J.* **626**, 551

[41] Mihalas, D. 1978, *Stellar Atmospheres*, W.H. Freeman, San Francisco

[42] Mihalas, D. & Weibel-Mihalas, B. 1999, *Foundations of Radiation Hydrodynamics*, Dover Publ., New York

[43] Mihalas, D., Auer, L.H. & Mihalas, B.R. 1978, *Astrophys. J.* **220**, 1001

[44] Mouradian, Z. & Garcia, A. 2007, in *The Physics of Chromospheric Plasmas*, eds. P. Heinzel, I. Dorotovic, R.J. Rutten, ASP-368, 3

[45] Olson, G. L., Auer, L. H. & Buchler, J. R 1986, *J. Quant. Spectrosc. Radiat. Transfer* **35**, 431

[46] Paletou, F. 1995, *Astron. Astrophys.* **302**, 587

[47] Parenti, S., Lemaire, P. & Vial, J.-C. 2005, *Astron. Astrophys.* **443**, 685

[48] Parenti, S., Vial, J.-C. & Lemaire, P. 2004, *Solar Phys.* **220**, 61

[49] Patsourakos, S. & Vial, J.-C. 2002, *Solar Phys.* **208**, 253

[50] Poland, A.I. & Mariska, J.T. 1988, in *Dynamics and Structure of Solar Prominences*, Université des Illes Baléares, 133

[51] Rutten, R.J. 2003, in *Radiative Transfer in Stellar Atmpspheres*, Utrecht University lecture notes, 8*th* edition

[52] Rutten, R.J., Hammerschlag, R.H., Bettonvil, F.C.M., et al. 2004, *Astron. Astrophys.* **413**, 1183

[53] Rybicki, G.B. 1971, *J. Quant. Spectrosc. Radiat. Transfer* **11**, 589

[54] Rybicki, G.B. & Hummer, D.G. 1991, *Astron. Astrophys.* **245**, 171

[55] Scharmer, G.B. 1981, *Astrophys. J.* **249**, 720

[56] Scharmer, G.B., Bjelksjo, K., Korhonen, T.K., et al. 2003, in *Innovative Telescopes and Instrumentation for Solar Astrophysics*, eds. S.L. Keil, S.V. Avakyan, SPIE **4853**, 341

[57] Scherrer, P.H., Bogart, R.S., Bush, R.I. et al. 1995, *Solar Phys.* **162**, 129

[58] Schmieder, B., Tziotziou, K. & Heinzel, P. 2003, *Astron. Astrophys.* **401**, 361

[59] Schmieder, S., Gunár, S., Heinzel, P. & Anzer, U. 2007, *Solar Phys.*, **241**, 53 (SGHA)

[60] Schmieder, B., Heinzel, P., Kučera, T. & Vial, J.-C. 1998, *Solar Phys.* **181**, 309

[61] Schmieder, B., Heinzel, P., Vial, J.-C. & Rudawy, P. 1999a, *Solar Phys.* **189**, 109

[62] Schmieder, B., Kučera, T., Heinzel, P. & Vial, J.-C. 1999b, in *8th SOHO Workshop proc.*, eds. J.-C. Vial, B. Kaldeich-Schümann, ESA SP-446, 605

[63] Secchi, A. 1877, *Le Soleil*, Gauthier-Villars, Paris

[64] Suematsu, Y., Ichimoto, K., Katsukawa, Y., et al. 2007, *American Astronomical Society Meeting 210*, **94.02**

[65] Tandberg-Hanssen, E. 1995, *The Nature of Solar Prominences*, Kluwer Acad. Publ., Dordrecht

[66] Tarbell, T.D., Tsuneta, S., et al. 2007, *American Astronomical Society Meeting 210*, **94.01**

[67] Vandenbussche, F.C. 2006, in *SOHO 17 - 10 Years of SOHO and Beyond*, eds. H. Lacoste, L. Ouwehand, ESA SP-617

[68] Vial, J.-C. 1982a, *Astrophys. J.* **253**, 330

[69] Vial, J.-C. 1982b, *Astrophys. J.* **254**, 780

[70] Wilhelm, K., Curdt, W., Marsch, E. et al. 1995, *Solar Phys.* **162**, 189

[71] Zharkova, V.V. & Morozhenko, N.N. 1998, in *XIVth Consultation on Solar Physics, proc.*, eds. B. Rompolt, J. Jakimiec, P. Heinzel, PAICz **88**, 246

Appendix A

Prominence fine structures in a magnetic equlibrium: II. A grid of two-dimensional models

Heinzel, P., Anzer, U. & Gunár, S. 2005
Astron. Astrophys., **442**, 331 (HAG)

Astronomy & Astrophysics manuscript no. aa3360-05
(DOI: will be inserted by hand later)

Prominence fine structures in a magnetic equilibrium

II. A grid of two-dimensional models

P. Heinzel[1,2], U. Anzer[2], and S. Gunár[1,3]

[1] Astronomical Institute, Academy of Sciences of the Czech Republic, 25165 Ondřejov, Czech Republic
e-mail: [pheinzel;gunar]@asu.cas.cz
[2] Max-Planck-Institut für Astrophysik, Karl-Schwarzschild-Strasse 1, 85740 Garching, Germany
e-mail: ula@mpa-garching.mpg.de
[3] Astronomical Institute, Faculty of Mathematics and Physics, Charles University, Prague, Czech Republic

Received 3 May 2005 / Accepted 1 July 2005

Abstract. We construct a grid of 2D vertical-thread models for prominence fine structures which are in magnetohydrostatic (MHS) equilibrium. Such thread models have been described in a previous paper by Heinzel & Anzer (2001), but here we use a modified 2D transfer code with an adaptive MHS grid. Multilevel non-LTE transfer calculations are now performed for a 12-level plus continuum hydrogen model atom, in order to study the behaviour of the Lyman-series lines observed by SOHO/SUMER. Our grid consists of 18 models which cover a range of central column masses, magnetic-field intensities and two parameters characterising the 2D temperature structure of the thread. Since different Lyman lines and their parts (line center, peak, wings) are formed at different places within the thread, the Lyman series may serve as a good diagnostic tool for thermodynamic conditions varying from central cool parts to a prominence-corona transition region. We demonstrate this behaviour for various lines, showing their synthetic profiles as seen from two perpendicular directions along and across the magnetic field lines, respectively, and displaying the respective contribution functions. This study confirms our earlier conclusion that the Lyman line profiles are much more reversed when seen across the field lines, compared to those seen along the lines. The latter can be even unreversed. We also show the geometrical cross-section (shape) of all 18 models. Their thread-like shape with a considerable aspect ratio resembles recent high-resolution Hα images. Finally, we discuss the relation of our thread models to the vertical threads studied by Fontenla et al. (1996).

Key words. Sun: prominences – magnetohydrodynamics (MHD) – radiative transfer – line: profiles

1. Introduction

During almost one decade of observations SOHO (*SOlar and Heliospheric Observatory*) has collected a large amount of UV and EUV data on prominences and filaments. Among them, spectral observations of hydrogen Lyman lines and continuum obtained by the SUMER UV-spectrograph represent an important constraint on prominence modelling. Various examples of such data and their analysis can be found in Schmieder et al. (1998, 1999, 2003) and Heinzel et al. (2001); see also a review of SOHO prominence observations by Patsourakos & Vial (2002). The formation depths of these optically-thick lines span the whole prominence structure and thus the line profiles of the Lyman series can provide us with a reliable diagnostics of prominence/filament thermodynamic conditions. The fact that SUMER is capable of observing the whole Lyman series is quite unique.

In order to interpret properly the Lyman-line profiles, one has to perform rather complex non-LTE radiative transfer computations using sophisticated models. Important steps towards this goal were the following: magnetohydrostatic (MHS) and radiative-transfer models developed by Heasley & Mihalas (1976), first 2D prominence models by Mihalas et al. (1978) and Vial (1982), demonstration of importance of the partial frequency redistribution (PRD) for hydrogen Lyman lines (Heinzel et al. 1987), a grid of 1D models by Gouttebroze et al. (1993), 2D models with PRD (Paletou et al. 1993, Paletou 1995), multi-thread models in energy balance by Fontenla et al. (1996). Recently, Heinzel & Anzer (2001) (hereafter referred to as Paper I) have generalised the 1D MHS models of Heasley & Mihalas (1976) to the 2D case and have given examples of 2D diagnostics of vertical fine-structure threads in MHS equilibrium. Three important aspects play a role in the spectral-line formation: the pressure structure, the temperature variation in the *prominence-corona transition region* (PCTR) and the depth variations of the line source functions. The pressure structure is described by 2D MHS equilibria (for details see also Heinzel & Anzer (2005)). The temperature profile is in principle determined by the energy balance, but here we model it by an ad hoc spatial variation and for the calculation of the source func-

tion we perform the consistent 2D radiative transfer. Moreover, PRD plays an important role for the ionisation of hydrogen and affects the line intensities. The results of Paper I support the conclusions of Heinzel et al. (2001) that when looking *along* the magnetic-field lines the Lyman-line profiles appear as unreversed or only weakly reversed emission profiles, while when looking *across* the field lines, the profiles may exhibit rather strong reversals. This behaviour is due to the temperature structure of the PCTR.

However, so far no detailed quantitative fit of all observed Lyman lines (e.g. those presented for three different prominences in Heinzel et al. (2001)) was achieved. It is the purpose of this paper to make further steps in our understanding of the behaviour of the Lyman spectrum formation. We construct here a grid of 18 fine-structure thread models, which are in 2D MHS equilibrium and have an infinite vertical extension. Selecting a set of input parameters allows us to demonstrate the sensitivity of individual models to various physical conditions. This experience will be used in the future to obtain a quantitative fitting of SOHO/SUMER Lyman spectra.

The paper is organised as follows. Section 2 summarizes the basic physical conditions inside the fine-structure thread and presents our 18 models. Section 3 describes the non-LTE radiative transfer in two dimensions, together with a new MHS adaptive-grid scheme. Section 4 explains how the so-called contribution functions can be used to visualize the line-formation regions. Section 5 gives a detailed discussion of our results obtained for individual models. Section 6 shows how the fine-structure dips can be seen in projection against the disk. Finally, Sect. 7 presents the discussion and the conclusions.

2. MHS models

For our modelling of prominence threads we use the form of vertically infinite 2D threads hanging in a horizontal magnetic field. The exact mathematical formulation of the equations of the MHS equilibrium was published in Paper I, here we give only an overview.

The pressure equation has the form

$$p(m,y) = 4p_{\rm c}(y)\frac{m}{M(y)}\left[1-\frac{m}{M(y)}\right] + p_0\ , \tag{1}$$

with the definition of the magnetic pressure

$$p_{\rm c}(y) = \frac{B_{z1}^2(y)}{8\pi} \tag{2}$$

and with $M(y)$ (the column mass integrated over x-direction) given by

$$M(y) = \frac{B_x(y)B_{z1}(y)}{2\pi g}. \tag{3}$$

Here p_0 is the boundary coronal pressure, $B_x(y)$ is the horizontal field-component (constant along a given field line), $B_{z1}(y)$ is the vertical field-component at the boundary and g the gravitational acceleration at the solar surface. Because of the requirement of MHS equilibrium we have the relation

$$B_{z1}^2(y) = B_{x0}^2 - B_x^2(y)\ . \tag{4}$$

Here B_{x0} is the horizontal field between individual threads. As in Paper I, we use the column-mass coordinate m instead of the cartesian coordinate x, which is more useful in the case of non-uniform temperature and ionisation structure. Then the transformation from the mass coordinate m to the spatial coordinate x requires the following integration

$$x = \int_{M(y)/2}^{m} \frac{1}{\rho}{\rm d}m' \tag{5}$$

at each value of the coordinate y, where ρ is the density.

The temperature profile with an empirically described PCTR first used by Anzer & Heinzel (1999) has the form

$$T(m,y) = T_{\rm cen}(y)+[T_{\rm tr}-T_{\rm cen}(y)]\left\{1-4\frac{m}{M(y)}\left[1-\frac{m}{M(y)}\right]\right\}^{\gamma_1}, \tag{6}$$

where $T_{\rm tr}$ represents the temperature at the boundary and the exponent γ_1 has to be chosen properly. The temperature at $x = 0$, $T_{\rm cen}(y)$, is given by

$$T_{\rm cen}(y) = T_{\rm tr} - (T_{\rm tr}-T_0)\left(1-\left|\frac{y}{\delta}\right|^{\gamma_2}\right), \qquad \text{for} \qquad |y| \le \delta. \tag{7}$$

T_0 is the (minimum) central temperature, 2δ represents the width of the thread in y-direction (perpendicularly to the field lines) and the exponent γ_2 is again a free parameter. The 2D temperature structure is then fully determined by the exponents γ_1 and γ_2.

The shape of synthetic spectral-line profiles obtained by radiative transfer modelling depends on the set of input parameters which describe the MHS equilibrium, the form of temperature structure, and on the incident radiation. The set of input MHS-parameters fully determines the shape of the magnetic dips and will influence the shape of the calculated synthetic profiles. The full description of all input MHS-parameters has been presented in Paper I. The first parameter which is varied in our calculations is the maximum column density M_0 appearing in the mass function $M(y)$

$$M(y) = M_0\left(1-\left|\frac{y}{\delta}\right|^{\gamma_3}\right), \qquad \text{for} \qquad |y| \le \delta. \tag{8}$$

Once we have prescribed M_0 we can use $B_x(0)$ (horizontal field in the middle of the thread) instead of B_{x0} (horizontal field between threads), where the former one represents a measurable quantity for prominences. The values of B_{x0} and $B_x(0)$ are simply related through Eqs. (3) and (4).

In order to describe the dependence of the synthetic profiles on given input parameters we have constructed a grid of 18 prominence models. Within this grid of models we varied M_0, $B_x(0)$ and the exponents γ_1 and γ_2. The other input parameters have been fixed for all our models, with the values:

$T_0 = 8000$ K; $T_{\rm tr} = 50\,000$ K; $2\delta = 1000$ km; $\gamma_3 = 2$; $p_0 = 0.03$ dyn cm^{-2}.

The model grid consists of three series with 6 models for each of them. The series differ only in the value of one of the γ-parameters. The models in each series have different values of M_0 and $B_x(0)$. The full list of our model grid

Table 1. Parameters for the model grid.

Models of series $\boldsymbol{A}$ $\gamma_1 = 5$ $\gamma_2 = 30$	Models of series $\boldsymbol{B}$ $\gamma_1 = 10$ $\gamma_2 = 60$	Models of series $\boldsymbol{C}$ $\gamma_1 = 10$ $\gamma_2 = 30$	M_0 [g cm^{-2}]	$B_x(0)$ [Gauss]
$\boldsymbol{A}_1$	$\boldsymbol{B}_1$	$\boldsymbol{C}_1$	2×10^{-4}	8, 4
$\boldsymbol{A}_2$	$\boldsymbol{B}_2$	$\boldsymbol{C}_2$	5×10^{-5}	4
$\boldsymbol{A}_3$	$\boldsymbol{B}_3$	$\boldsymbol{C}_3$	2×10^{-5}	2
$\boldsymbol{A}_{3\_1}$	$\boldsymbol{B}_{3\_1}$	$\boldsymbol{C}_{3\_1}$	2×10^{-5}	10
$\boldsymbol{A}_4$	$\boldsymbol{B}_4$	$\boldsymbol{C}_4$	5×10^{-6}	1
$\boldsymbol{A}_{4\_1}$	$\boldsymbol{B}_{4\_1}$	$\boldsymbol{C}_{4\_1}$	5×10^{-6}	5

is summarised in Table 1. Geometrically all these models represent structures with a width of 1000 km and their lengths vary between 2000 km and 25 000 km which partially depends on the solution of the radiative-transfer problem (see below). An example of the 2D variation (in the $x - y$ plane) of the temperature, gas pressure and density and of the magnetic structure is shown in Paper I.

3. 2D multilevel radiative transfer

For the solution of the 2D radiative transfer problem we used the Accelerated Lambda Iteration (ALI) technique (Auer & Paletou 1994) with the short characteristics (SC) method to obtain the formal solution along individual rays. A detailed description of the method is given in Paper I.

In contrast to our previous paper we use here a 12-level plus continuum hydrogen model atom (see e.g. Heinzel et al. 1997), in order to obtain higher members of the Lyman series as they are observed by SOHO/SUMER. The 12-level model also ensures a higher accuracy as compared to the 5-level model (at least of lower Lyman lines) because of more precisely computed level populations.

In Figs. 1 and 2 we show averaged profiles of the Lβ and Lδ lines, in order to compare the 5-level and 12-level solutions. Full lines result from averaging along the dip thickness 2δ, dashed lines represent averaging along the whole dip length (i.e. in the x-direction). The difference in intensities is given by the different level populations, while the ionisation is almost the same for the two cases.

3.1. Incident radiation at the thread boundary

Lyman-line profiles of the incident radiation are taken from the SOHO/SUMER disk observations made by Warren et al. (1998). The observed profiles show an asymmetry due to flows in the solar atmosphere, however, for our purposes we used quiet-Sun profiles symmetrised by averaging the red and blue parts. Since Warren et al. (1998) data do not include the Lα line (this line was difficult to detect with SUMER), we still use the same incident profiles as in the previous Paper I. The averaged incident radiation was computed at height of 10 000 km above the solar surface.

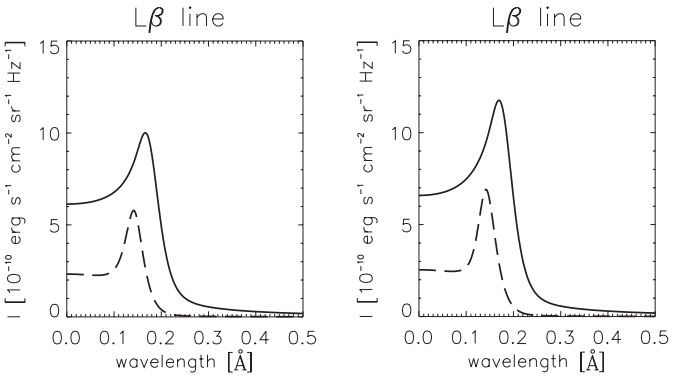

Fig. 1. Lβ profiles for the 5-level model (*left-hand side*) and for the 12-level model (*right-hand side*). Full lines represent averages over y, dashed lines are mean profiles over x.

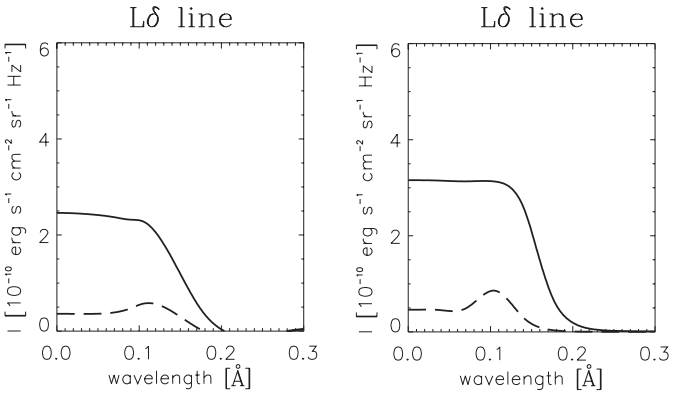

Fig. 2. Lδ profiles for the 5-level model (*left-hand side*) and for the 12-level model (*right-hand side*). Full lines represent averages over y, dashed lines are mean profiles over x.

3.2. Adaptive MHS grid

A new feature of the present models is that we use here an *adaptive* MHS grid. In the y-direction the grid is fixed and we use the logarithmic spacing in order to properly describe a steep PCTR at the boundary. However, in the x-direction, i.e. along the field lines, the geometrical extension of the magnetic dip follows from the MHS equilibrium – for a given field strength, the larger M_0 the deeper the dip will be (and thus the structures are effectively less extended). Moreover, the conversion from the column-mass coordinate m as used to express the MHS equilibrium (Paper I) to geometrical one needed for 2D radiative transfer, depends on the local gas density which in turn depends on the ionisation degree. In Paper I we just used an initial estimate of the ionisation degree (see Eq. (17) in Paper I) and kept the x-grid fixed. In this paper we follow the procedure described in Heinzel & Anzer (2003). After the converged non-LTE solution is obtained for a given 2D model, and thus 2D distribution of the ionisation degree, a new grid is constructed along the field lines which is consistent with the current ionisation degree. Then the 2D transfer is solved again to get a new ionisation degree and this procedure is repeated until the changes between two subsequent grids are negligible. Typically 5 iterations are sufficient. For more details see Heinzel & Anzer (2003)

4. Contribution function

For the analysis of the diagnostic properties of the Lyman lines we need to know the corresponding formation depths. For this purpose we use the contribution function C. This function for the emergent specific intensity is defined by the integral relation

$$I_\nu(0) = \int C_{\rm I}(l){\rm d}l \,, \tag{9}$$

where l is the geometrical length (depth) which we take here either in x or y-direction. In terms of the optical depth τ_ν the contribution function is defined as

$$C_{\rm I}(\tau_\nu) = \ S_\nu(\tau_\nu){\rm e}^{-\tau_\nu} \,. \tag{10}$$

The transformation between optical depth τ_ν and geometrical depth l is given by

$$C_{\rm I}(l){\rm d}l = C_{\rm I}(\tau_\nu){\rm d}\tau_\nu \,. \tag{11}$$

Then the contribution function has the form

$$C_{\rm I}(l) = \ S_\nu(\tau_\nu){\rm e}^{-\tau_\nu}\chi_\nu. \tag{12}$$

Here χ_ν represents the absorbtion coefficient. Since the source function is given by $S_\nu = \eta_\nu/\chi_\nu$, we obtain

$$C_{\rm I}(l) = \ \eta_\nu \, {\rm e}^{-\tau_\nu} \,, \tag{13}$$

with η_ν being the emission coefficient.

The contribution to the specific intensity on the surface from a given point of the geometrical grid depends on the direction of the line-of-sight. In this paper we display the contributions as functions of x and y for two perpendicular directions of view: along x-coordinate (along the field lines) and along y-coordinate (across the field lines). 2D plots of computed contribution functions, for all considered Lyman lines, are available on the web site `http://www.asu.cas.cz/~radtrans`. Examples are shown below for selected models, lines and positions in the line profile (line center, peaks, wings). These plots show the spatial variation of the contribution to the specific intensity as a function of the position in the structure of the prominence ($x - y$ dimensions are in cm). White regions represent places with major contribution to the specific intensity (for a given frequency), black regions indicate minor contributions. The contours in the figures are iso-lines of the temperature structure. Isothermal contours are plotted in steps of 10 000 K. Note that these figures are not drawn to the true scale.

5. Synthetic profiles

In this section we discus the dependence of our synthetic profiles on the values of the input parameters defining individual models, as well as their variation with the viewing direction. All line-profile plots are also available at `http://www.asu.cas.cz/~radtrans`.

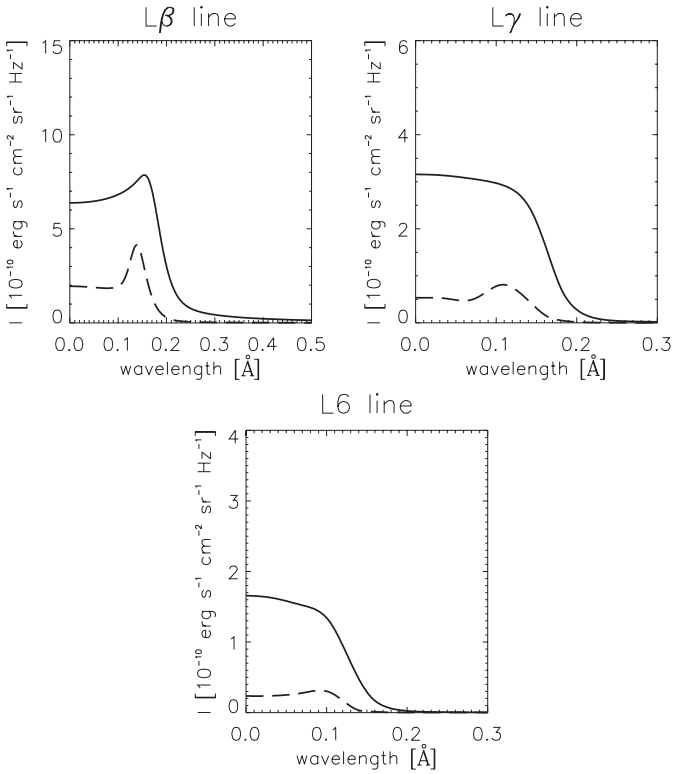

Fig. 3. The profiles of lines Lβ, Lγ and L6. Full lines are y-mean profiles, dashed lines are x-mean profiles.

5.1. Dependence on the field orientation

As was shown in Heinzel et al. (2001), the computed Lyman-line profiles of prominences strongly depend on the viewing angle with respect to the magnetic-field orientation. Paper I contains one example of a synthetic profile computed for a specific model with a 5-level atom. Here we show synthetic profiles obtained for our grid of models using an extended 12-level hydrogen atom.

In Fig. 3 we show Lβ, Lγ and L6 line profiles. Full lines again represent profiles averaged over y, dashed lines are profiles averaged over x. The intensity plots (Fig. 4) show the variation of the line intensity as a function of x and wavelength. Each profile there represents a mean profile averaged locally over 1000 km in x-direction.

The field orientation has a two-fold effect on the Lyman-line shapes. First, the density distribution *along* the field lines is given by the MHS equations, while *across* the field lines the column mass $M(y)$ can vary in a rather arbitrary way because the individual flux tubes are magnetically separated. For the variation of $M(y)$ we use an ad-hoc form described by Eq. (8). Second, along the field lines the temperature variation is supposed to be relatively smooth because of efficient heat conduction - we describe this variation by an empirical formula (6). On the other hand, the heat conduction across the field lines is strongly inhibited and thus we assume a schematic temperature profile (7) which exhibits a rather steep rise at the boundaries.

From our grid of models we conclude that the Lα profiles are rather similar when one looks along the x-axis and when one looks in y-direction. But for all higher lines we see that

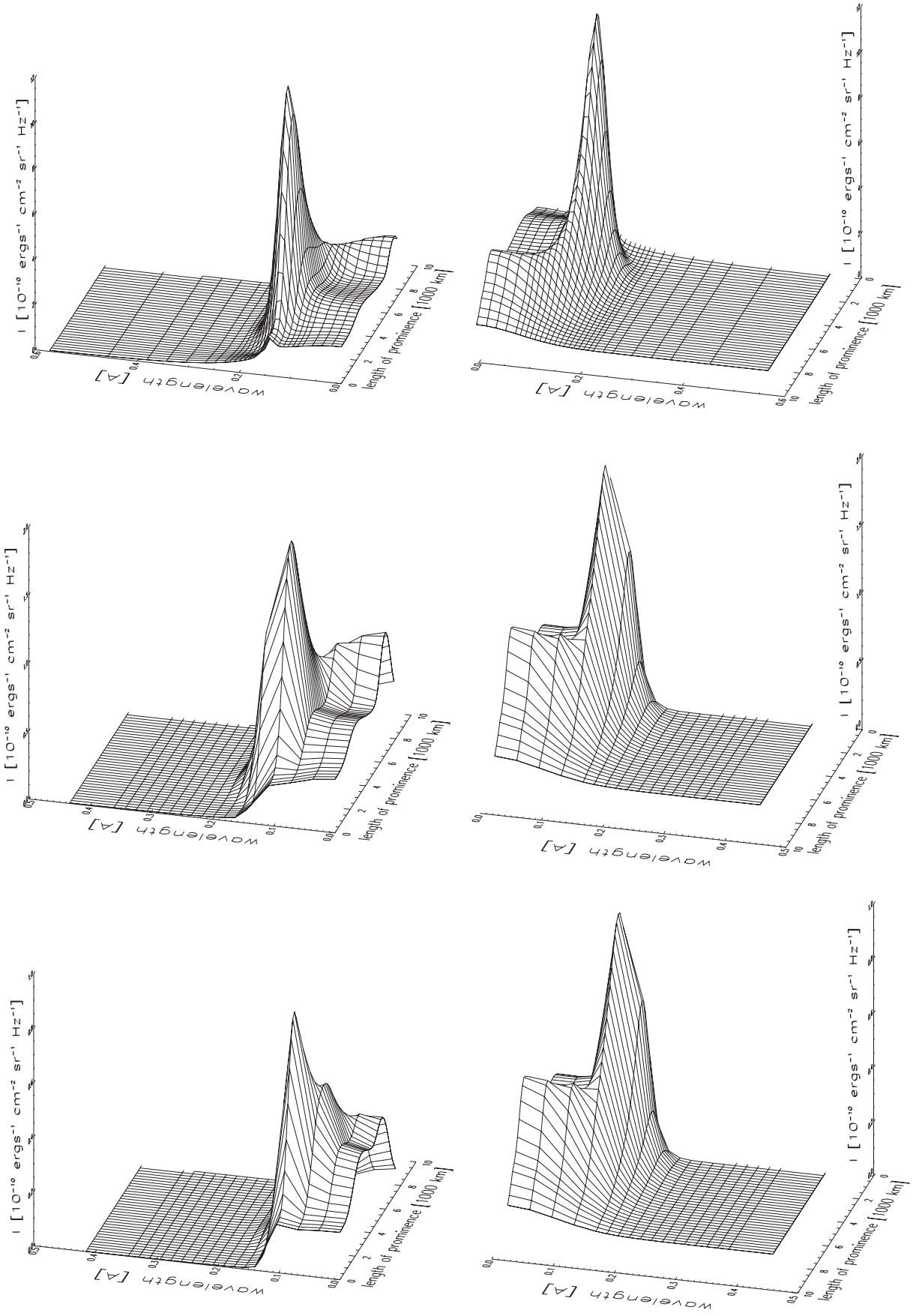

Fig. 4. The intensity plots for the lines of Lβ (*pair of plots at the top*), Lγ (*middle plots*) and L6 (*pair of plots at the bottom*). On the left-hand side the structure is shown from the front, on the right-hand side from the rear.

in general the line profiles are much more reversed when we look along the y-axis (i.e. across the field lines). This trend becomes more pronounced when one goes to higher lines. The x-variation of the line intensity is shown for three different lines in Fig. 3. We can see that in the center of the structure (at $x = 0$) the reversal is not very pronounced, but it strongly increases outside the central parts. Finally, approaching the boundaries where $p \to p_0$, the profiles become unreversed with a central emission peak. This behaviour can be understood as follows. First, we have to realize that the temperature structure across the field lines is rather flat in the inner parts and only very near to the boundaries the temperature steeply increases to values of the surrounding corona - see Eq. (4) and the contours in the plots of the contribution functions). On the other hand, along the field lines (along the x-direction), the central temperature increases much more gradually (Eq. (3)). Let us now assume that looking across the field lines, we see different 'slabs' of thickness of 1000 km, having temperatures gradually increasing from $T_0 = 8000$ K to $T_{\rm tr}$. At the same time, the gas pressure decreases. It was demonstrated already by Gouttebroze et al. (1993) that in the case of isothermal-isobaric finite prominence slabs, the Lyman-line reversals strongly increase when the temperature starts to exceed $8-10 \times 10^3$ K and if also the pressure is sufficiently high. This is exactly what we observe outside the innermost parts of our 2D configurations. This behaviour can be understood by looking at the line source-function variations along the line-of-sight. The slabs are strongly irradiated from the solar surface and if the corresponding radiation temperature is comparable to the slab temperature, the line source function is only weakly decreasing towards the irradiated slab surface. However, by increasing the slab temperature, the source function starts to increase in the slab interior and decreases towards to surface. This naturally produces a strong reversal in Lyman lines, unless the gas pressure is so low that the whole line goes into emission (i.e. when it becomes optically thin).

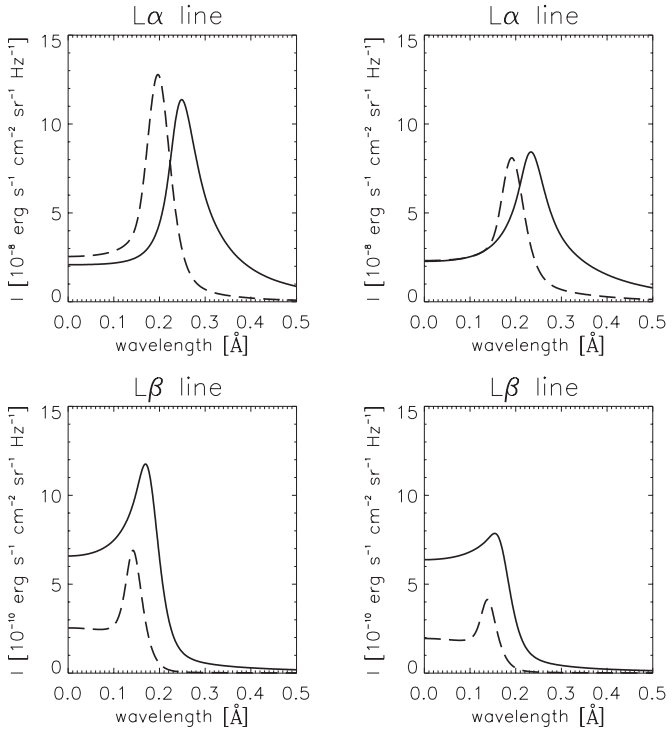

Fig. 5. Profiles of Lα and Lβ for model $\boldsymbol{A}_1$ (*left-hand side*) and $\boldsymbol{C}_1$ (*right-hand side*). Full lines are y-mean profiles, dashed lines are x-mean profiles.

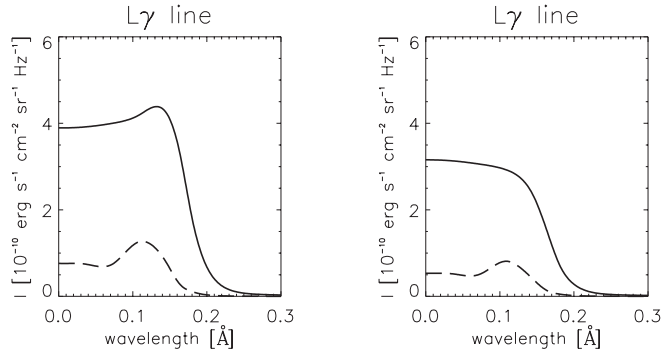

Fig. 6. Profiles of Lγ for model $\boldsymbol{A}_1$ (*left-hand side*) and $\boldsymbol{C}_1$ (*right-hand side*). Full lines are y-mean profiles, dashed lines are x-mean profiles.

5.2. Dependence on the shape of temperature structure

The shape of the temperature structure is fully described by the exponents γ_1 and γ_2. For the discussion of effects of the temperature structure on the line profiles it is useful to compare two models which differ only in one of these parameters.

5.2.1. Effect of the exponent γ_1

Here we compare models $\boldsymbol{A}_1$ and $\boldsymbol{C}_1$ which differ in γ_1 ($\gamma_1 = 5$ for $\boldsymbol{A}_1$ and $\gamma_1 = 10$ for $\boldsymbol{C}_1$). We demonstrate the effect of changes of the exponent γ_1 on various lines.

Lα and Lβ

The center of these spectral lines for both directions of view forms at the boundary of the prominence structure (Fig. 8), in areas with a high temperature rising up to the boundary value of 50 000 K where p goes to coronal pressure p_0. The value of the Lα central intensity is almost the same for both directions of view and for both models. Model $\boldsymbol{A}_1$ gives the higher value of a specific intensity in the line peak (more than 40%) compared to model $\boldsymbol{C}_1$ (Fig. 5). This is due to a higher temperature in the region of the peak formation (Fig. 8). The temperature is higher because we keep the boundary temperature fixed and have a lower temperature gradient close to the boundary for $\boldsymbol{A}_1$, given by the lower value of the parameter γ_1. The wings of spectral lines are mostly optically thin and originate in the center of the thread (Fig. 8), the place with a low temperature, high density and negligible influence of the parameter γ_1.

Lγ

The region of formation of the line center is now deeper inside the structure. This leads to a higher value of the specific intensity in the center of Lγ for $\boldsymbol{A}_1$ (up to 20%) in comparison to $\boldsymbol{C}_1$ (Fig. 6) which is due to higher temperature in the region of origin of the line center (similarly as for Lβ). The mean

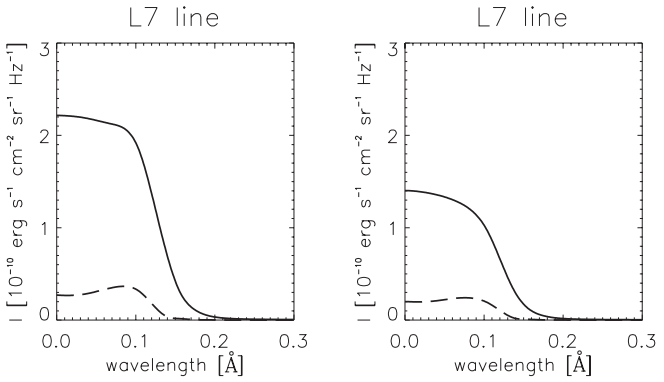

Fig. 7. Profiles of L7 for model $\boldsymbol{A}_1$ (*left-hand side*) and $\boldsymbol{C}_1$ (*right-hand side*). Full lines are y-mean profiles, dashed lines are x-mean profiles.

profile over y for the model $\boldsymbol{A}_1$ has a weak self-reversal, while for $\boldsymbol{C}_1$ the y-averaged profile is in emission (Fig. 6). This is again due to temperature differences. The mean profiles over x for both models still have a self-reversed shape (see discussion in Sect. 5.1), however the value of the specific intensity for $\boldsymbol{A}_1$ is higher by some 20% than for model $\boldsymbol{C}_1$. The line wings are formed in the prominence center with negligible influence of the parameter γ_1.

Lδ - L11
The mean-profiles over y are in emission while the mean profiles over x show self-reversal for both models (Fig. 7). This is again consistent with our interpretation given in Sect. 5.1. The central and peak-intensities of the model $\boldsymbol{A}_1$ are higher by some 40%. The line wings of lines Lδ – L7 originate in the central part with the lowest temperature. The place of origin of the spectral lines L8 – L11 is however shifted into regions with higher temperature which is required for the formation of these high-frequency lines (Fig. 9).

5.2.2. Effect of the exponent γ_2

Now we compare models $\boldsymbol{B}_1$ ($\gamma_2 = 60$) and $\boldsymbol{C}_1$ ($\gamma_2 = 30$).

Lα
The line center originates from the boundary for both models and the values of the central intensity are identical. The place of formation of the peak intensity is shifted into the structure and the value of the specific intensity for model $\boldsymbol{C}_1$ is higher (up to 30%) compared to the model $\boldsymbol{B}_1$ (Fig. 11). It is due to the shape of the temperature structure (Fig. 12). The profiles for both models and for each direction of view have a self-reversal. The line wings, formed in the center of the thread, are not affected by the parameter γ_2.

Lβ
The central intensity is again influenced by the shape of the temperature structure and for $\boldsymbol{C}_1$ is higher by about 20%. The $\boldsymbol{C}_1$ profile has a deeper self reversal while for $\boldsymbol{B}_1$ the self reversal is quite negligible (Fig. 13). This is due to the formation of the peak in model $\boldsymbol{C}_1$ in places with higher temperature than in model $\boldsymbol{B}_1$ (Fig. 14). The line wings again form in the central regions.

Lγ - L11
The mean profiles over y are in emission for both models. For model $\boldsymbol{C}_1$, the x-averaged profiles show a self-reversal, but $\boldsymbol{B}_1$ profiles averaged over x are in emission.

5.2.3. Line-center intensity for the Lyman series

In order to demonstrate how the Lyman series can be used to diagnose the thread structure, we plot in Fig. 10 the contribution functions at the line center of Lα to L10, as viewed along the magnetic-field lines. This clearly shows that higher members of the Lyman series do form deeper and thus their line-center intensity reflects the temperature and density variations through the structure.

Figure 10 shows that the Lα line center is formed at rather high temperatures, around 50 000 K or even more. We have made some test simulations with $T_{\rm tr} = 10^5$ K and for such models the Lα line-center formation region is entirely between 50 000 and 10^5 K. However, the actual mechanism of the line formation at these regions largely depends on the density. At the boundary where the gas pressure reaches values $p_0 = 0.03$ dyn cm^{-2} in our models, the particle number density is almost two orders of magnitude lower than at the central cool regions. Therefore, the scattering of incident radiation can still play a role in determining the line source function, together with collisional excitations. According to our plots of Lα profiles, the central intensity is roughly a factor of two larger than that of the diluted quiet-Sun intensity.

5.3. Effect of the field intensity variation

The value of the magnetic-field intensity has an essential effect on the shape of the prominence structure. We show the effect of field intensity variation for models $\boldsymbol{A}_3$ ($B_x(0) = 2$ Gauss) and $\boldsymbol{A}_{3\_1}$ ($B_x(0) = 10$ Gauss). Due to the lower value of the field intensity the model $\boldsymbol{A}_3$ has a length around 5000 km while model $\boldsymbol{A}_{3\_1}$ is 10 000 km long. Changes of the x-dimension cause different distributions of density inside the prominence structure.

Lα
The line profile for model $\boldsymbol{A}_3$ has a sharp self-reversal shape for both directions of view, different from model $\boldsymbol{A}_{3\_1}$ (Fig. 15). A higher value of the peak intensity (up to 30%) for model $\boldsymbol{A}_3$ is due to the higher temperature in the place of origin of the peak (Fig. 16).

Other spectral lines
The other line profiles are not reversed, for both models and directions of view (when averaged over x-direction). $\boldsymbol{A}_3$ profiles have higher values of the specific intensity due to higher temperatures.

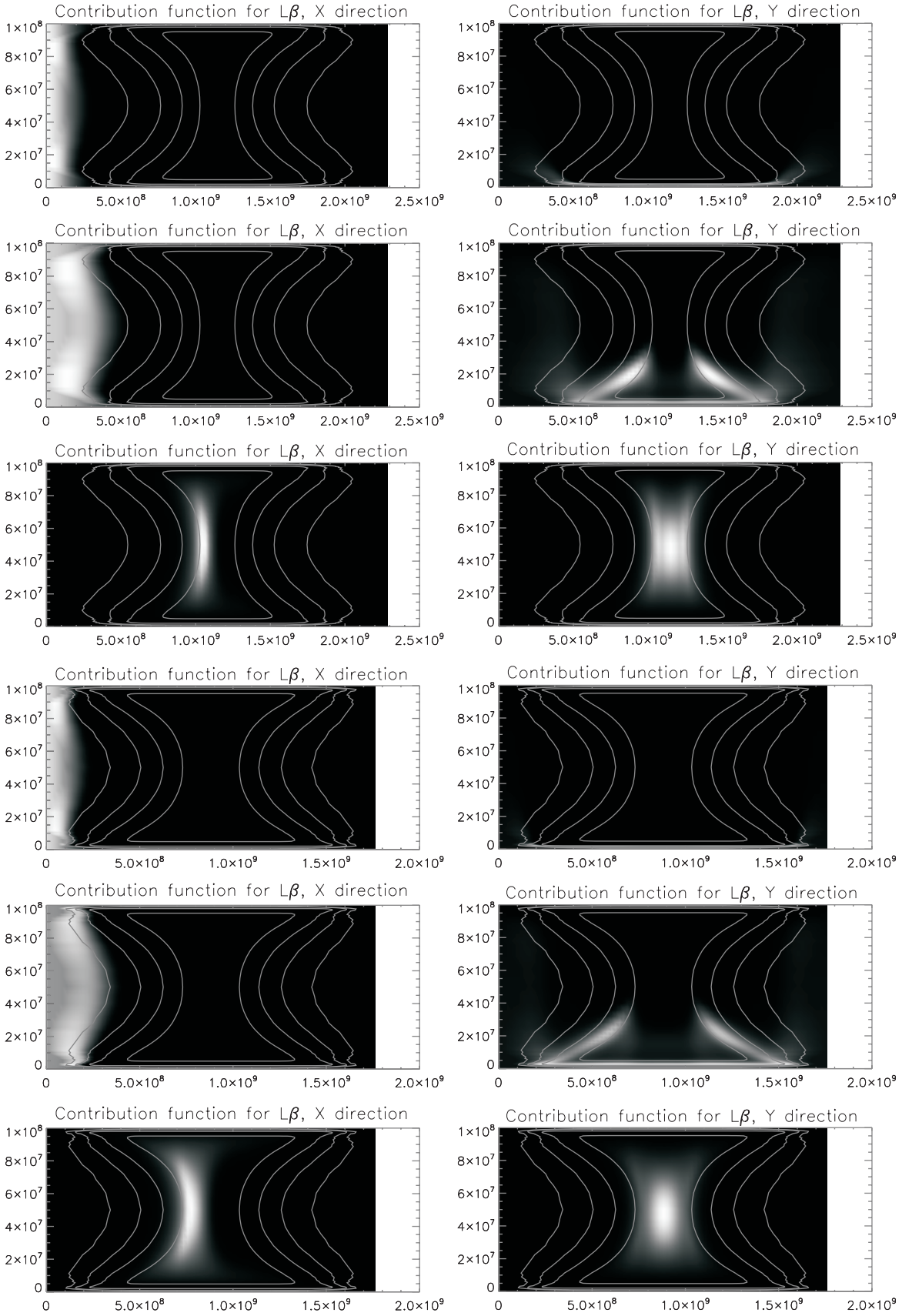

Fig. 8. Lβ contributions as functions of x and y. The first six panels are for model $\boldsymbol{A}_1$, the other six for model $\boldsymbol{C}_1$. On the left-hand side the viewing is in the direction along the x-axis (*from the left side*), on the right-hand side in the y-direction (*from the bottom*). The upper pairs of each model are for the central frequency, the middle pairs are for the peak frequency and the lower ones represent contributions in the line wings. $x - y$ dimensions are in cm.

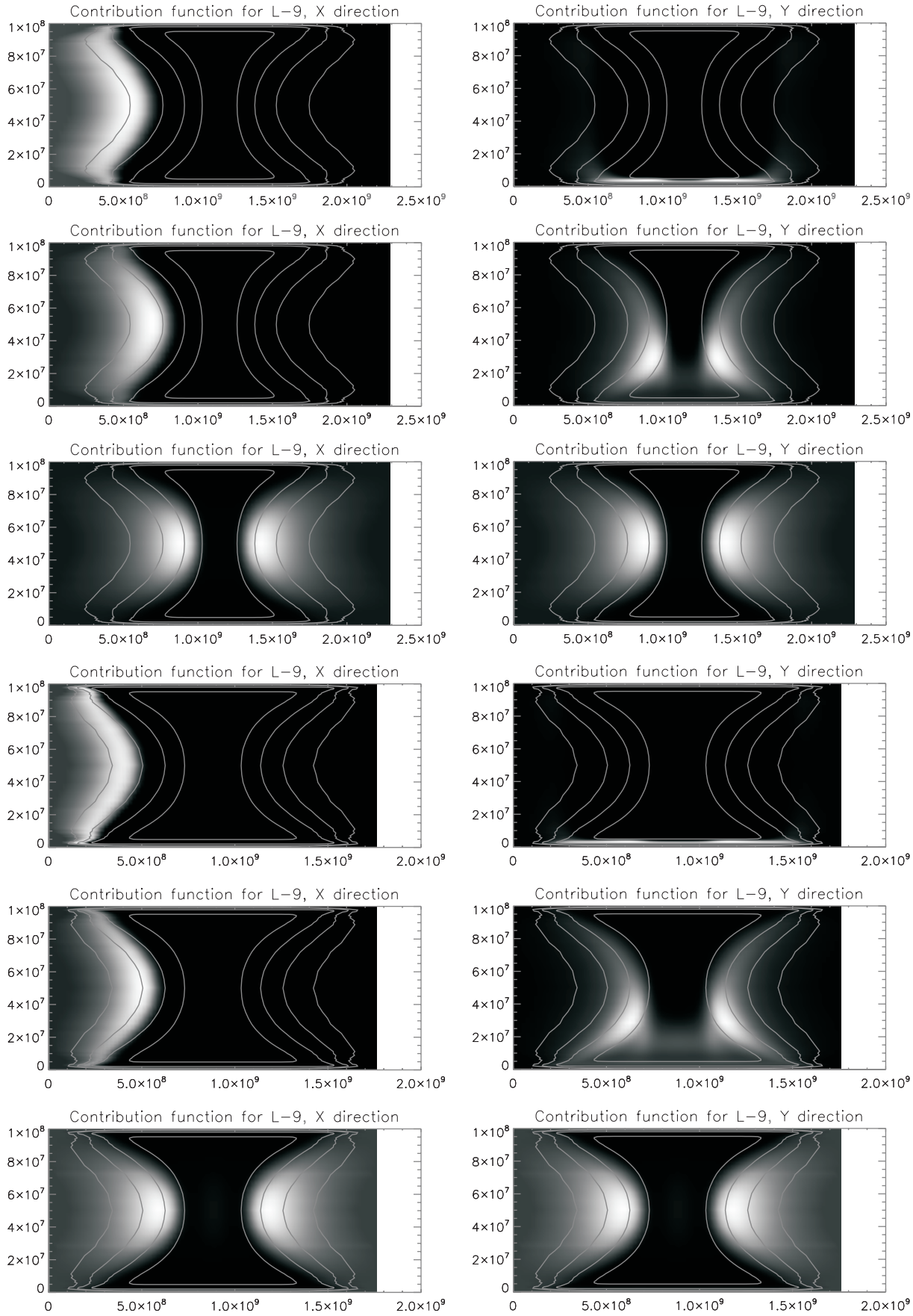

Fig. 9. L9 contributions as functions of x and y. The first six panels are for model $\boldsymbol{A}_1$, the other six for model $\boldsymbol{C}_1$. The figure is arranged in the same way as Fig. 8.

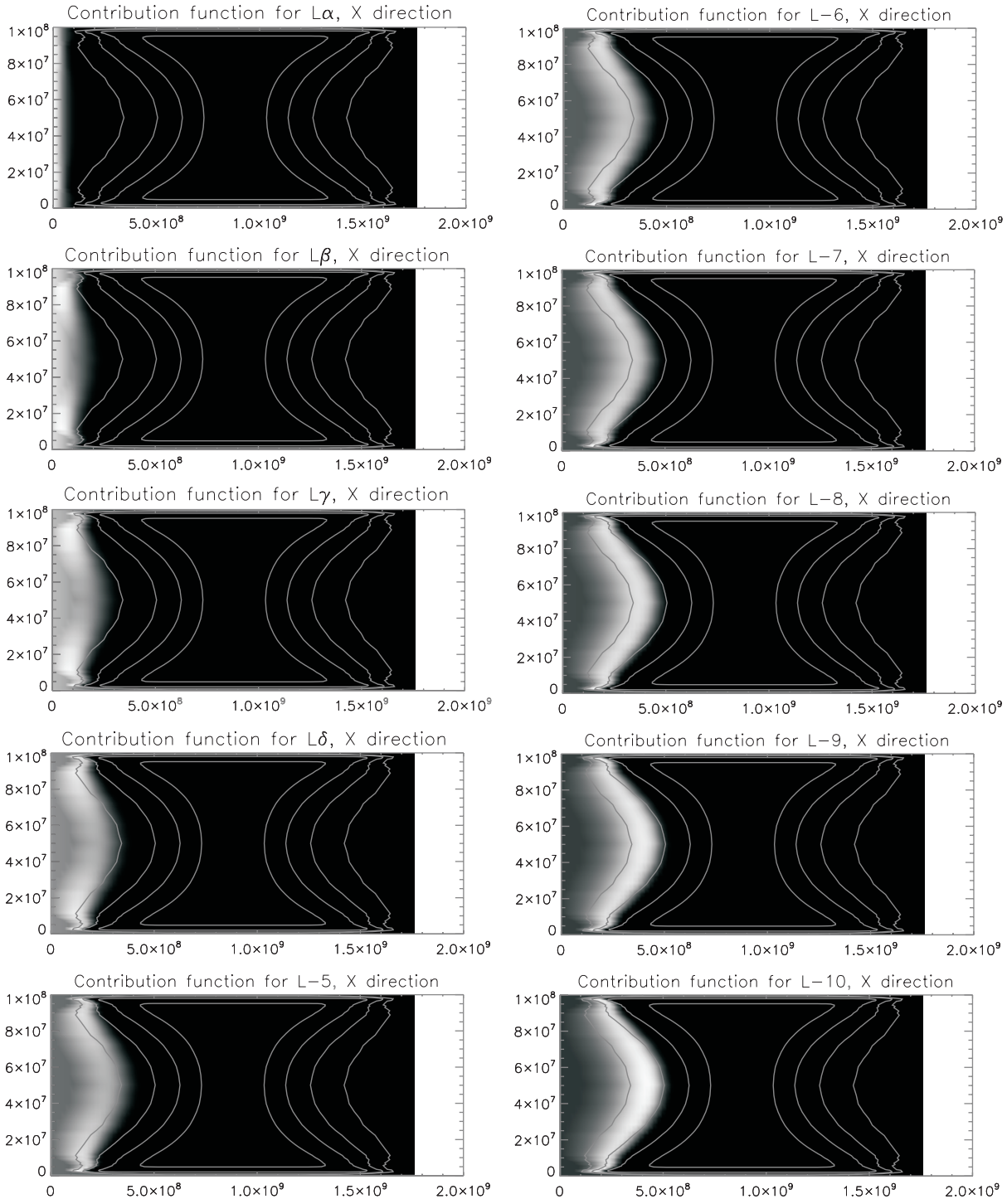

Fig. 10. Depth-variations of the line-center contribution function for the Lyman series (Lα to L10), as viewed along the field lines. The model $\boldsymbol{A}_1$ was used.

6. Geometrical shape of the thread structure

The geometrical shape of the prominence fine structure, i.e. its horizontal cross-section, is determined mainly by the magnetic field strength and the column mass, and to some extent also by the temperature structure. Variations of the input parameters for our 18 models have an essential effect on the magnetic field structure (dip) and therefore lead to different extensions in x-direction. In Fig. 17 the geometrical shape of all models is shown. Each of these models has a fixed width of 1000 km in y-direction. The extension in x-direction (along magnetic field lines) is for each model represented by the length of the black bars.

Now we shall briefly analyse the effect of each input parameter on the geometrical length of the threads. The higher values of $B_x(0)$ give more extended thread structure due to larger magnetic tension force (dips can be less deep). This is clear from

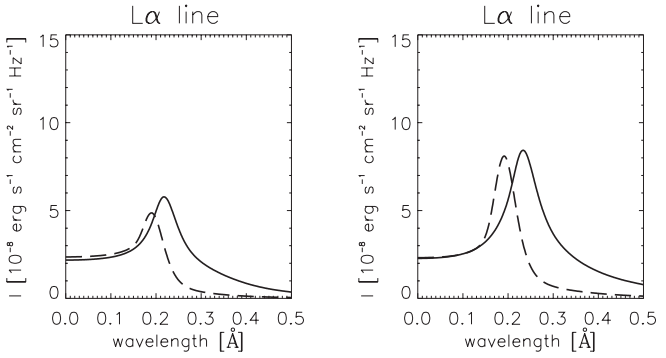

Fig. 11. Profiles of Lα for model $\boldsymbol{B}_1$ (*left-hand side*) and $\boldsymbol{C}_1$ (*right-hand side*). Full lines are y-mean profiles, dashed lines are x-mean profiles.

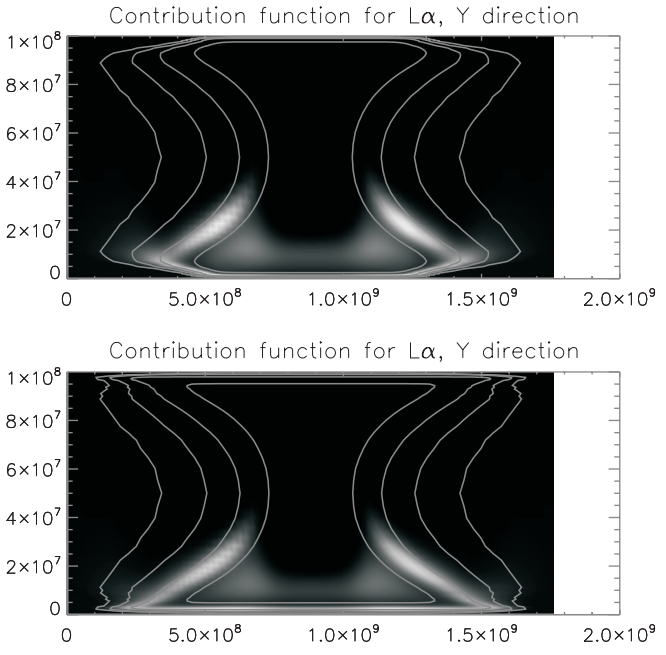

Fig. 12. Lα contribution functions for model $\boldsymbol{B}_1$ (*top*) and $\boldsymbol{C}_1$ (*bottom*), showing the contributions for the peak frequency for observation in y-direction.

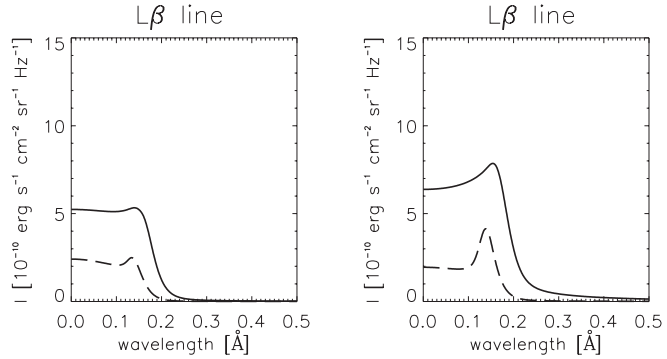

Fig. 13. Profiles of Lβ for model $\boldsymbol{B}_1$ (*left-hand side*) and $\boldsymbol{C}_1$ (*right-hand side*). Full lines are y-mean profiles, dashed lines are x-mean profiles.

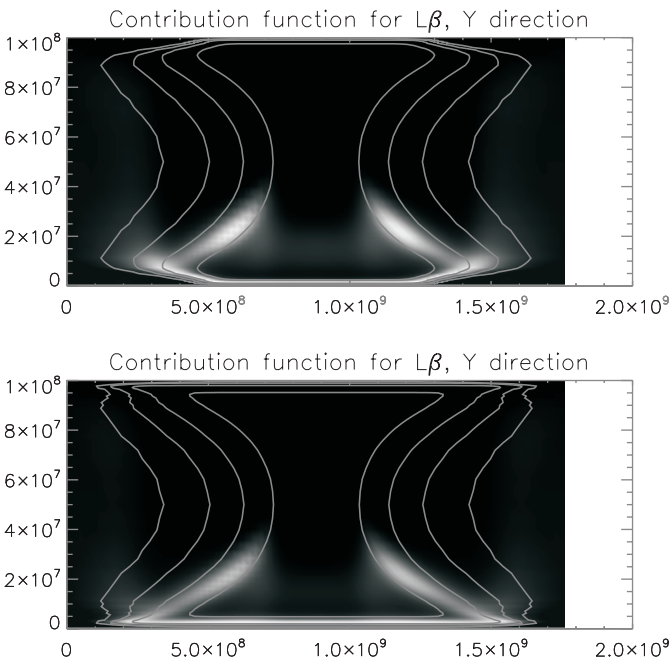

Fig. 14. Lβ contribution functions for model $\boldsymbol{B}_1$ (*top*) and $\boldsymbol{C}_1$ (*bottom*), showing the contributions for the peak frequency for observation in y-direction.

a comparison of the models with labels ***3*** and ***3_1*** and those labelled ***4*** and ***4_1***. Models with labels ***1*** and ***3_1*** have comparable values of $B_x(0)$ but different values of M_0. The larger extension of models ***1*** is due to the larger amount of mass in the structure. The temperature structure described by the γ parameters has also an influence on the density distribution in the thread. The shallower the increase of temperature, the more extended is the structure of the thread.

The actual shape of the structure as it would be projected onto the solar disk is somewhat more complex, but it retains features from Fig. 17. Restricting the thread to a finite vertical extension, one can use the 2D horizontal distribution of the vertical opacity (optical thickness) to compute e.g. the Hα line contrast against the solar disk. For this a simple cloud model with the constant source function can be applied (see e.g. Heinzel & Anzer 2005). The resulting dark fibrils are rather long, their aspect ratio depends on the fixed thickness in y-direction which we took here to be 1000 km. In reality, however, this thickness can be smaller and thus the fibrils could appear long. This situation resembles recent high-resolution (up to about 0.2 arcsec) Hα images obtained either with the new SVST or with DOT on La Palma (see Engvold 2005; or DOT website). We interpret the central parts of *quiescent* filaments as being composed of shorter, densely packed fibrils which are in fact the magnetic dips projected onto the disk – see also Aulanier & Démoulin (1998, 2003). Very long individual fibrils which extend out of the filament body may have different nature, they can correspond to low-lying extended fluxtubes with significant horizontal flows (Engvold 2005).

7. Discussion and conclusions

Let us now comment briefly on the models of Fontenla et al. (1996). These models were aimed, as ours here, to represent the vertical fine-structure threads of quiescent prominences. But in

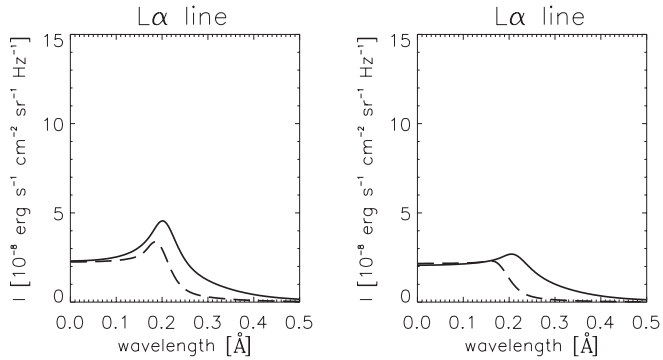

Fig. 15. Profiles of Lα for models A_3 (*left-hand side*) and A_{3_1} (*right-hand side*). Full lines are y-mean profiles, dashed lines are x-mean profiles.

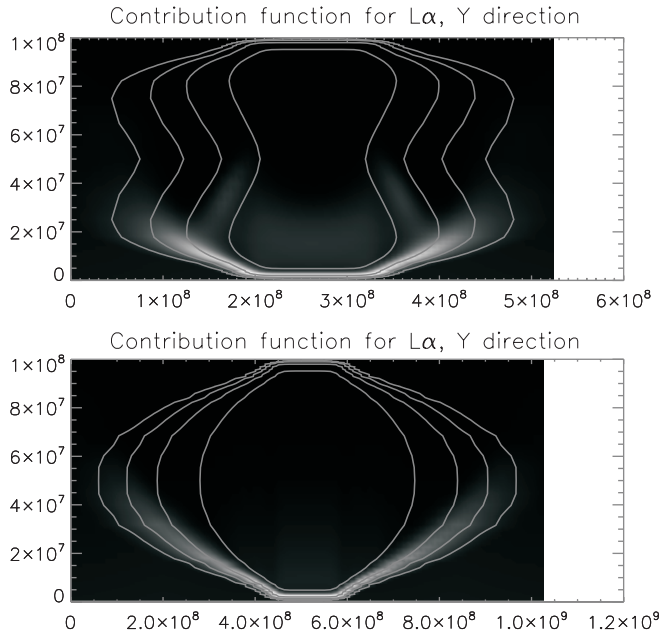

Fig. 16. Lα contribution functions for model A_3 (*top*) and A_{3_1} (*bottom*), showing the contributions for the peak frequency for observation in y-direction.

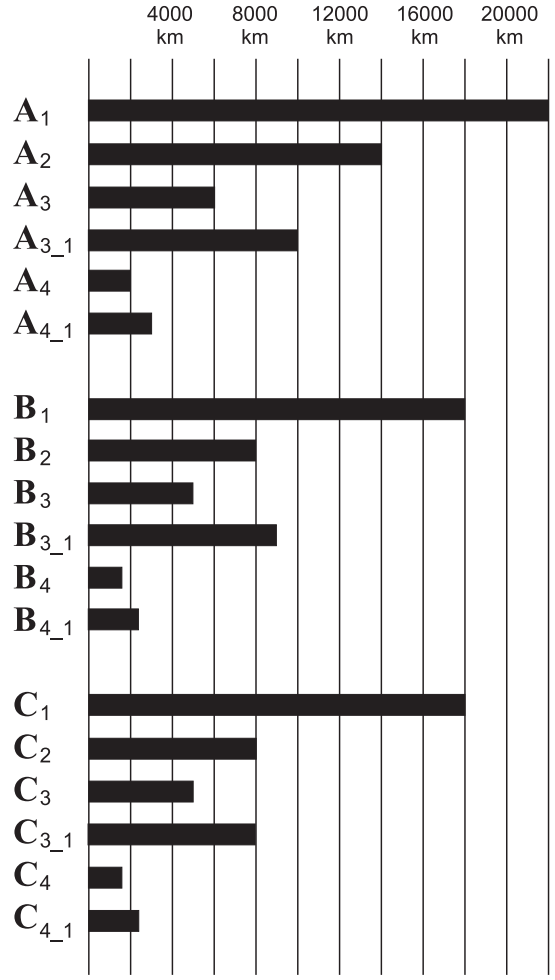

Fig. 17. The geometrical shape of all models. Each bar has a width of 1000 km.

contrast to our models they consider 1D isobaric slab configurations. Their approach is in some respect complementary to ours: they determine the temperature structure in the slab from the condition of energy balance (assuming some kind of heating function and taking the energy transport by ambipolar diffusion into account). But they do not solve the MHS equilibrium equations. In contrast to this we solve the 2D MHS equilibrium, but prescribe ad hoc temperature profiles ignoring the energetics. Also the geometries of the two sets of models are very different: Fontenla et al. (1996) take a very large number of extremely thin slabs (just a few tens km each) which are perpendicular to the magnetic field (see also discussion by Anzer & Heinzel (1999)), while we study individual 2D threads aligned with the magnetic field. Fontenla et al. (1996) considered several 1D slabs (threads) along the line-of-sight and the emergent synthetic intesities were computed for Lyman lines (also using PRD for Lα and Lβ). Comparing this to our 2D models, two problems arise. First, in our MHS scenario, only one thread (dip) is allowed along the given field line, others being formed along nearby lines. This then means that looking strictly along the field lines, we can see only one thread, not a multithread structure. However, our 2D approach allows us to look also across the field lines and then we can see several threads along the line-of-sight. Considering the energy balance in the way similar to Fontenla et al. (1996), in 2D one could compute the ambipolar diffusion along the field lines, but look through several threads perpendicularly. The second problem is that the models of Fontenla et al. (1996) are very narrow along the magnetic field, while ours show a rather long extension in this direction (see Fig. 17). This is a direct consequence of the MHS equilibrium and the empirical temperature structure.

Another comment concerns the assumption that the threads are very extended vertically, in fact we take them as vertically infinite in our 2D approach. The idea comes from Poland & Mariska (1988) who suggested that when a dip is formed locally the field below becomes compressed and that above diluted. Therefore the dip region grows in height, by vertical propagation and thus forms a thread filled by cool plasma. However, the real vertical extension is difficult to estimate. From the observational point-of-view, one should try to derive the vertical extension from high-resolution disk observations of

filaments (see discussion in Sect. 6), from the theoretical side a 3D MHS configuration should be constructed and then used for fully 3D transfer modelling.

We discuss how the magnetic field configuration of a vertical prominence thread can influence the structure of the prominence–corona transition region. As we show, depending on this structure one obtains different line profiles for the series of Lyman lines, namely when looking, respectively, *along* and *across* the magnetic-field lines. Studying these lines can give us important information on the physical conditions in the prominence threads. In the next paper we intend to apply this modelling to sets of Lyman-line profiles observed in prominences by SOHO/SUMER. By searching for the best fit simultaneously to all observed Lyman profiles one should be able to determine in detail the physical structure of prominence threads. However, this may require a more complex modelling based on multi-thread configurations - several threads seen along the line-of-sight which passes across the magnetic-field lines.

Acknowledgements. P.H. acknowledges the support from MPA Garching, U.A. thanks for support of the Ondřejov Observatory. This work was done in the frame of grant No. IAA 3003203 of the Grant Agency of the Academy of Sciences of the Czech Republic, ESA-PECS project No. 98030 and the research project AVOZ10030501. SOHO is a space mission of international cooperation between ESA and NASA. The authors thank to P. Gouttebroze and J.-C. Vial for their valuable comments.

References

Anzer, U., & Heinzel, P. 1999, A&A, 349, 974
Auer, L. H., & Paletou, F. 1994, A&A, 285, 675
Aulanier, G., & Démoulin, P. 1998, A&A, 329, 1125
Aulanier, G., & Démoulin, P. 2003, A&A, 402, 769
Engvold, O. 2005, in Multiwavelength Investigations of Solar Activity, ed. A. V. Stepanov, E. F. Benevolenskaya, & A. G. Kosovichev (Cambridge Univ. Press), Proc. IAU Symp., 223, 187
Fontenla, J. M., Rovira, M., Vial, J.-C., & Gouttebroze, P. 1996, ApJ, 466, 496
Gouttebroze, P., Heinzel, P., & Vial, J.-C. 1993, A&AS, 99, 513
Heinzel, P., & Anzer, U. 2001, A&A, 375, 1082 (Paper I)
Heinzel, P., & Anzer, U. 2003, in Stellar Atmosphere Modeling, ed. I. Hubeny, D. Mihalas, & K. Werner, ASP Conf. Ser., 288, 441
Heinzel, P., & Anzer, U. 2005, in Solar Magnetic Phenomena, ed. A. Hanslmeier, A. Veronig, & M. Messerotti, Astron. Astrophys. Space Sci. Lib., 320 (Dordrecht: Springer), 115
Heinzel, P., Gouttebroze, P., & Vial, J.-C. 1987, A&A, 183, 351
Heinzel, P., Schmieder, B., & Vial, J.-C. 1997, in Proc. Fifth SOHO Workshop, ESA SP-404, 427
Heinzel, P., Schmieder, B., Vial, J. C., & Kotrč, P. 2001, A&A, 370, 281
Heasley, J. N., & Mihalas, D. 1976, ApJ, 205, 273
Mihalas, D., Auer, L. H., & Mihalas, B. 1978, 220, 1001
Paletou, F. 1995, A&A, 302, 587
Paletou, F., Vial, J.-C., & Auer, L. H. 1993, A&A, 274, 571
Patsourakos, S., & Vial, J.-C. 2002, Sol. Phys., 208, 253
Poland, A. I., & Mariska, J. T. 1988, in Dynamics and Structure of Solar Prominences, Proc. of a Workshop held at Palma de Mallorca, ed. J. L. Ballester, & E. R. Priest, Universitat de les Illes Balears, 133
Schmieder, B., Heinzel, P., Kucera, T., & Vial, J.-C. 1998, Sol. Phys., 181, 309
Schmieder, B., Heinzel, P., Vial, J.-C., & Rudawy, P. 1999, Sol. Phys., 189, 109
Schmieder, B., Tziotziou, K., & Heinzel, P. 2003, A&A, 401, 361
Vial, J.-C. 1982, ApJ, 254, 780
Warren, H. P., Mariska, J. T., & Wilhelm, K. 1998, ApJ, 119, 105

Appendix B

Prominence parameters derived from hydrogen Lyman-α profiles measured by SOHO/SUMER

Gunár, S., Teriaca, L., Heinzel, P. & Schühle, U. 2006
in *SOHO 17 - 10 Years of SOHO and Beyond*,
eds. H. Lacoste, L. Ouwehand, ESA SP-617 (GTHS)

PROMINENCE PARAMETERS DERIVED FROM HYDROGEN LYMAN-α SPECTRAL PROFILES MEASURED BY SOHO/SUMER

S. Gunár[1,3], L. Teriaca[2], P. Heinzel[1], and U. Schuehle[2]

[1]Astronomical Institute, Academy of Sciences of the Czech Republic, 25165 Ondřejov, Czech Republic
[2]Max-Planck-Institut für Sonnensystemforschung, Max-Planck-Str. 2, 37191 Katlenburg-Lindau, Germany
[3]Astronomical Institute, Faculty of Mathematics and Physics, Charles University, Prague, Czech Republic,
gunar@asu.cas.cz

ABSTRACT

We present SOHO/SUMER observations of a solar prominence in the hydrogen Lyman-α line and compare the line profiles with synthetic ones obtained using our 2D prominence modelling. The observations contain the raster image of a solar prominence in Lyman-α and in Si III lines (observed on April 18, 2005). The raster consists of 76×50 pixels and in each pixel we have the full profile of the two lines. In order to derive the prominence parameters we use our fine structure models of vertical threads in magnetohydrostatic (MHS) equilibrium (Heinzel & Anzer (2001) and Heinzel et al. (2005)). By varying of the input parameters (central temperature, boundary pressure, magnetic field, central column mass and turbulent velocity) we obtained synthetic Lyman-α profiles which are in good agreement with the observed ones. In this way we are able to determine thermodynamical parameters in the observed prominence.

1. INTRODUCTION

One decade of observations carried out by the SUMER UV-spectrograph (*Solar Ultraviolet Measurements of Emitted Radiation*) on board of SOHO (*SOlar and Heliospheric Observatory*) provide important insights into the properties of the solar atmosphere. A large part of the observations have been devoted to solar quiescent prominences and the data represents major steps towards our understanding of their structure and physical parameters. The unique ability of the SUMER to observe the whole hydrogen Lyman series leads to considerable amount of spectral data of Lyman lines and of the continuum in prominences. Some of these data and their analysis can be found in Schmieder et al. (1998, 1999, 2003), Heinzel et al. (2001) and Stellmacher et al. (2003); see also a review of SOHO prominence observations by Patsourakos & Vial (2002). SUMER spectroscopic data provide an important constraint on prominence modelling. In order to interpret them properly one has to use highly sophisticated models with complex non-LTE radiative transfer computations. Such models of the prominence fine structure were recently presented by Heinzel & Anzer (2001) and Heinzel et al. (2005).

2. OBSERVATIONS

The SUMER instrument (Wilhelm et al. 1995) on board SOHO is a stigmatic spectrograph equipped with two photon-counting detectors (A and B). Both detectors have 1024 spectral columns and 360 spatial rows. Since May 2004 the Detector A has been showing a deterioration of the electronics responsible of the readout in the y direction (y-ADC), affecting the spatial (along the slit) information, while the x-ADC is working correctly, leading to correct spectral information. During April 18, 2005 only the 58 rows at the bottom of the detector retained their full spatial resolution ($\approx 1''$) and were used for the present study. The study consists of a scan of a $85" \times 50"$ area centred at coordinates $X = 1001", Y = 200"$ inside a large prominence shown in the He II 304$\mathring{A}$ image (Fig. 1) from EIT at the day of the observation. The scan was obtained by stepping the telescope by $1.13"$ westward with the $0.3" \times 120"$ slit illuminating the bottom part of detector A. In such a way 76 spectra were acquired by exposing for 10 seconds. Two spectral windows $\approx$ 2Å wide (50 pixels, 43.8 mÅ/pix), centred on the Si III 1206.51 and on the H I Ly-α 1215.67, were selected to be finally telemetered to the ground. Observations started at 15:48:14 UTC and ended at 16:08:16 UTC. Due to the continuously changing detector conditions, special attention needs to be paid to the data reduction process. The flat-fields, in particular, have been obtained by averaging and median filtering large amounts of data acquired during this epoche.

The observational data consist of the raster of 76 pixels with the Lyman α and Si III line profiles in each spatial pixel. For the analysis of the Lyman α profiles, and for their comparison with the synthetic profiles obtained by modelling of a static prominence, we need profiles with symmetrical shape. Such profiles occur in the observational data in a small clustered locations (3 to 5 pixels

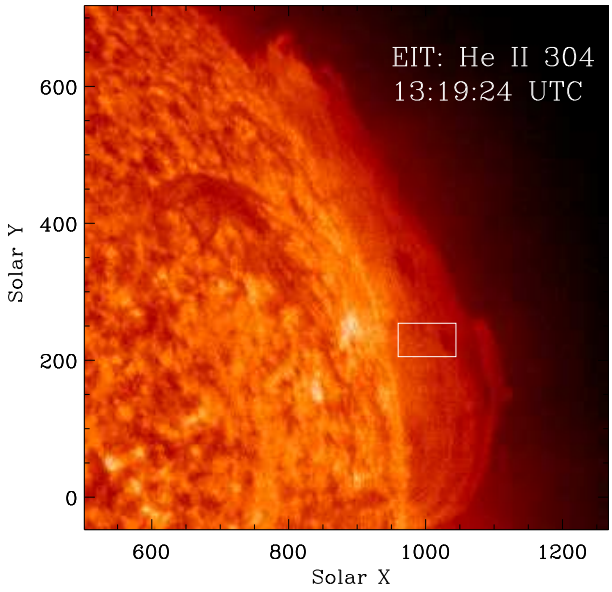

Figure 1. Position of the raster in the image from the EIT in the He II *304Å.*

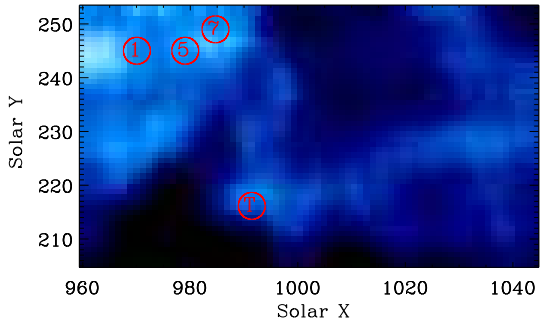

Figure 2. Raster image of the $85" \times 50"$ *(76× 50 pixels) area centred at solar coordinates* $X = 1001", Y = 200"$*. Red circles indicate the four areas (1, 5, 7, T) within which small cluster of pixels where chosen to yield the analysed line profiles.*

close to each other) and they ensure us that there are no differential velocities in the observed areas. For the comparison of the observed data with our models we took out four small areas with symmetrical profiles clustered in nearby pixels. For each area (1, 5, 7, T - denotes a bright vertical thread) we did the average profile of nearby symmetrical profiles. In Fig. 2 we show the positions of these areas in the raster image.

3. MODELLING

Models of prominences we use here are presented by Heinzel & Anzer (2001) and Heinzel & Anzer (2005). They consist of two-dimensional vertically infinite threads in MHS equilibrium with empirically prescribed temperature structure. Two-dimensional prominence thread models provide us with different synthetic profiles when the orientation of the line-of-sight is along or across the magnetic field lines, respectively (Heinzel et al. 2005). The information about the orientation of the field lines with respect to the line-of-sight is an important constraint for analysis of the observed spectra. From the observations carried out by ground observatories one can see the shape of the filament before/after it is observed as a prominence on the limb. From the shape of the filament it is possible to estimate the orientation of the magnetic field in the prominence/filament with certain accuracy. For our study we use the observations from the Meudon Spectroheliograph and from the Big Bear Solar Observatory (BBSO). The analysis of the ground-based observations from April 13 to April 18, 2005 shows that the following prominence is observed more-less along the field lines (Fig. 3).

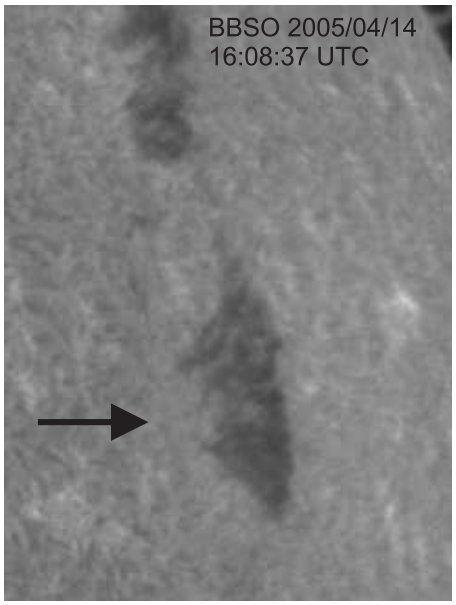

Figure 3. The filament observed by BBSO before it was observed as a limb prominence by SUMER. An arrow shows the line-of-sight for the SUMER observations.

Area	T_0 [K]	M_0 [g cm^{-2}]	$B_x(0)$ [Gauss]	p_0 [dyn cm^{-2}]	v_t [$\times\ c_s$]
1	8000	8.10^{-5}	6	0.03	0.8
5	6000	5.10^{-5}	4	0.025	0.8
7	6000	5.10^{-5}	4	0.035	0.8
T	8000	$1.6.10^{-5}$	2	0.03	0.4

Table 1. List of the input parameters for each area on the raster.

Each model of the prominence is prescribed by a set of the input parameters. This set consists of a central (minimum) temperature T_0, column mass in the center of the thread M_0, horizontal field strength in the middle of the thread $B_x(0)$, coronal pressure p_0, exponents γ_1 and γ_2 prescribing the temperature structure and a turbulent velocity given as a constant fraction of the sound speed.
By varying of this set of the parameters we obtain the best fit of the synthetic Lyman α profiles to the observed ones for each area. The input parameters for these models are listed in the Tab. 1. Exponents γ_1 and γ_2 are equal to 5 and 30. The plots of the observed and the synthetic Lyman α line profiles are shown in Fig. 4. The full bold lines represent the synthetic profiles, the dashed lines are observed Lyman α profiles with plotted error bars.

4. DISCUSSION AND CONCLUSIONS

The observed profiles of the Lyman-α line shown in Fig. 4 could be very well reproduced in all four selected regions. Small discrepancies are still in the wings of the line, as the modelled profiles tend to be narrower than observed, while reproducing the width and depth of the central reversal. Thus the parameters derived in the Tab. 1 represent the best compromise obtained by fitting this complex line profiles. The good correspondence between the models and the observed profiles is the result of using rather sophisticated thread-like MHS models where the non-LTE radiative transfer is computed in 2D and using the partial redistribution in Lyman lines for analysis. Since we have met severe difficulties in fitting the higher Lyman lines by just 1D models, this novel approach seems to be promising. It also allows us to consider the effect of the line-of-sight orientation with respect to the magnetic field lines on the emergent line profiles which is rather critical for analysis.
From our results we find that B is between 4 and 6 gauss near the limb and around 2 gauss higher up. However, this values are quite smaller than those recently measured by Merenda et al. (2005) in a polar crown (around 30 G). Values between 10 and 20 gauss are also measured by Casini et al. (2003). Further investigations, both theoretical and observational, seem necessary to solve this discrepancy.

ACKNOWLEDGMENTS

This work was supported by ESA-PECS project No. 98030. SOHO is a space mission of international cooperation between the European Space Agency (ESA) and the National Aeronautic and Space Administration (NASA). The SUMER instrument and its operation are financed by the Deutsches Zentrum für Luft und Raumfahrt (DLR), the Centre National d'Études Spatiales (CNES), NASA and ESA's PRODEX programme (Swiss contribution).

REFERENCES

[1] Casini, R., Lpez Ariste, A., Tomczyk, S.; Lites, B. W.: 2003, *Astrophysical J.* **598**, 67

[2] Heinzel, P. & Anzer, U.: 2001, *Astron. Astrophys.* **375**, 1082

[3] Heinzel, P., Anzer, U. & Gunar, S.: 2005, *Astron. Astrophys.* **442**, 331

[4] Heinzel, P., Schmieder, B., Vial, J.C. & Kotrč, P.: 2001, *Astron. Astrophys.* **370**, 281

[5] Merenda, L., Trujillo Bueno, J., Landi degl'Innocenti, E., Collados, M.: 2005, *ESA SP 596*, 18

[6] Patsourakos, S. & Vial, J.-C.: 2002, *Solar Phys.* **208**, 253

[7] Schmieder, B., Heinzel, P., Kucera, T. & Vial, J.-C.: 1998, *Solar Phys.* **181**, 309

[8] Schmieder, B., Heinzel, P., Vial, J.-C. & Rudawy, P.: 1999, *Solar Phys.* **189**, 109

[9] Schmieder, B., Tziotziou, K. & Heinzel, P.: 2003, *Astron. Astrophys.* **401**, 361

[10] Stellmacher, G., Wiehr, E. & Dammasch, I.E.: 2003, *Solar Phys.* **217**, 133

[11] Wilhelm, K., Curdt, W., Marsch, E., and 13 coauthors: 1995, *Solar Phys.* **162**, 189

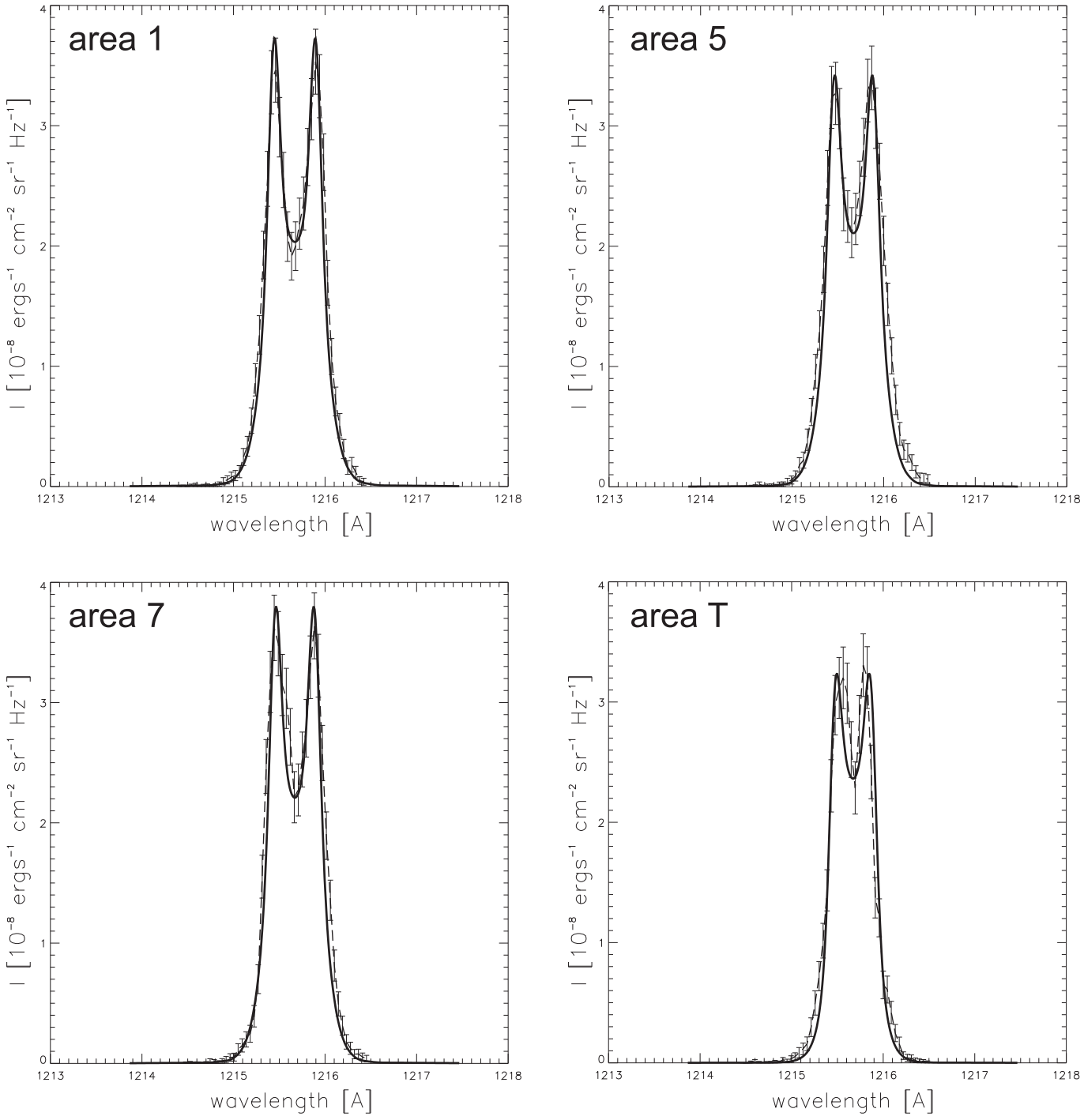

Figure 4. Lyman α profiles for each area on the raster (1, 5, 7, T). Full bold lines represent the synthetic profiles, the dashed lines are observed Lyman α profiles with plotted error bars.

Appendix C

Prominence fine structures in a magnetic equlibrium: III. Lyman continuum in 2D configurations

Gunár, S., Heinzel, P. & Anzer, U. 2007a
Astron. Astrophys. **463**, 737 (GHA)

A&A 463, 737–743 (2007)
DOI: 10.1051/0004-6361:20066142

Astronomy & Astrophysics

Prominence fine structures in a magnetic equilibrium

III. Lyman continuum in 2D configurations

S. Gunár[1,2,3], P. Heinzel[1], and U. Anzer[2]

[1] Astronomical Institute, Academy of Sciences of the Czech Republic, 25165 Ondřejov, Czech Republic
e-mail: [gunar;pheinzel]@asu.cas.cz
[2] Max-Planck-Institut für Astrophysik, Karl-Schwarzschild-Strasse 1, 85740 Garching, Germany
e-mail: ula@mpa-garching.mpg.de
[3] Astronomical Institute, Faculty of Mathematics and Physics, Charles University, Prague, Czech Republic

Received 29 July 2006 / Accepted 19 October 2006

ABSTRACT

Aims. We discuss the behavior of the Lyman continuum profiles studied on the grid of 2D vertical-thread models for prominence fine structures.
Methods. Multilevel non-LTE transfer calculations for a 12-level plus continuum hydrogen model atom are used.
Results. Since the Lyman continuum is formed in regions with different temperatures for different orientations between the magnetic field direction and the line-of-sight, our Lyman continuum modeling, together with additional information from Lyman lines, represents a very useful tool for the determination of the thread structure.
Conclusions. A comparison between our theoretical Lyman continuum models between 800 Å and 911 Å with the observed values shows that such a modeling can give interesting new constraints on the temperature structure in prominence threads.

Key words. Sun: prominences – radiative transfer – line: profiles

1. Introduction

In the past ten years the observations by the SUMER UV-spectrograph (Wilhelm et al. 1995) on board SOHO (*SOlar and Heliospheric Observatory*) have produced a considerable amount of spectral data of hydrogen Lyman lines and of the continuum in prominences. Some of these data and their analysis can be found in Schmieder et al. (1998, 1999, 2003), Heinzel et al. (2001), and Gunár et al. (2006); see also a review of SOHO prominence observations by Patsourakos & Vial (2002) and Heinzel et al. (2006). These Lyman line and continuum observations represent an important constraint for prominence modeling. To interpret them properly one has to use highly sophisticated models with complex non-LTE radiative transfer computations and include the *prominence-corona transition region* (PCTR). An earlier study by Fontenla et al. (1996) considered an ensemble of many thin vertical 1D slabs, each having its own PCTR. They found that their results are not entirely compatible with the available observations and therefore some magnetic shear will be required. More recently Labrosse & Gouttebroze (2004) presented radiative transfer calculations of the He I triplet lines in a 1D vertical slab and also concluded that the presence of a PCTR will be required to match the observations. 2D models of the prominence fine structure were presented by Heinzel & Anzer (2001, hereafter referred to as Paper I). They consist of two-dimensional vertically infinite threads in magnetohydrostatic (MHS) equilibrium (for further details see also Heinzel & Anzer 2005). These models consistently solve the 2D radiative transfer with partial frequency redistribution in Lyman lines, together with the MHS equations. The importance of such two-dimensional modeling for a proper interpretation of the SUMER spectra was suggested by Heinzel et al. (2001). A detailed analysis of the SUMER spectra of two quiescent prominences shows a strong unreversed emission detected in Lyman lines higher than Lα in one case. The other prominence with a similar brightness in the Lyman spectra exhibits all lines strongly reversed. This can be explained by a different orientation of the magnetic field with respect to the line-of-sight. Thus the prominence threads are seen from different sides with the different shape of the PCTR. This idea is further corroborated by Heinzel et al. (2005, hereafter referred to as Paper II), where we have taken an important step towards the understanding of the behavior of the Lyman spectrum formation. While Paper II concentrated on the analysis of the Lyman line formation and no discussion of the Lyman continuum behavior has been done there, the purpose of this paper is to model the Lyman continuum. Section 2 of this paper describes our 2D modeling and Sect. 3 presents the discussion and gives our conclusions.

2. 2D modeling of the Lyman continuum

The temperature structure of fine structure threads is characterized by a PCTR with a steep gradient of the temperature across the magnetic field lines and a shallower increase of the temperature along the field lines. Empirical temperature profiles of these threads were first used by Heinzel & Anzer (2001), who assumed a simple analytical description with

$$T(m,y) = T_{\rm cen}(y) + [T_{\rm tr} - T_{\rm cen}(y)] \left\{ 1 - 4\frac{m}{M(y)} \left[1 - \frac{m}{M(y)} \right] \right\}^{\gamma_1}, \quad (1)$$

where $T_{\rm tr}$ represents the temperature at the boundary (for the hydrogen plasma was set to the 50 000 K) and the exponent γ_1 determines the gradient of the temperature along the field lines

(x-direction). Column-mass scale m is parallel to the x-direction with a simple relation through the plasma density. The temperature in the mid-plane (i.e., at $x = 0$) is given by

$$T_{\rm cen}(y) = T_{\rm tr} - (T_{\rm tr} - T_0)\left(1 - \left|\frac{y}{\delta}\right|^{\gamma_2}\right), \qquad \text{for} \qquad |y| \le \delta, \quad (2)$$

where T_0 is the (minimum) central temperature (here we take 8000 K), 2δ represents the width of the thread perpendicular to the field lines (the width for our model is 1000 km), and the exponent γ_2 represents the steep temperature gradient across the field lines. The 2D temperature structure is then fully determined by the exponents γ_1 and γ_2. The density structure of the prominence thread was calculated for MHS equilibria in our Papers I and II. In the present paper we take these results into account. The magnetic field lines projected onto the (m, y)-plane are parallel to the m-direction.

Concerning limitations of our model: our 2D modeling of the prominence fine structure including the radiative transfer represents the most advanced approach. There are no such 3D models yet. However, we are about to work on a generalization of our model to 3D. We do not consider magnetic shear because our threads are always along the magnetic field independent of the fact that the field can be sheared with respect to the prominence/filament axis. Plasma flows in general do not have a strong influence on the Lyman continuum profiles (they are not affected by Doppler shift).

3. Effect of the different temperature structure

To show the influence of different temperature structure on the Lyman continuum we use the models $\boldsymbol{A}_1(\gamma_1 = 5)$ and $\boldsymbol{C}_1(\gamma_1 = 10)$ of our Paper II. Model $\boldsymbol{B}_1$ differs from $\boldsymbol{C}_1$ only in the value of the parameter γ_2. Since in these models the PCTR slab across the field lines is very thin, the Lyman continuum is formed in regions deeper in the thread and is not directly influenced by γ_2. Minor effects of γ_2 on the Lyman continuum profile are due to its influence on the global shape of the temperature structure. That results in similar Lyman continuum profiles for models $\boldsymbol{B}_1$ and $\boldsymbol{C}_1$. The other models of our grid from Paper II ($\boldsymbol{A}_2, \boldsymbol{A}_3$, etc.) show the same behavior as $\boldsymbol{A}_1$ and $\boldsymbol{C}_1$, but with smaller Lyman continuum intensities.

The parameter γ_1 prescribes the PCTR area along the field lines characterized by a shallower gradient of the temperature. The formation depth of the Lyman continuum is inside this region and thus the exponent γ_1 has a significant effect on the Lyman continuum profile. The basic parameters of the models $\boldsymbol{A}_1(\gamma_1 = 5)$ and $\boldsymbol{C}_1(\gamma_1 = 10)$ are: $M_0 = 2 \times 10^{-4}$ g cm^{-2}; $B_x(0) = 8.4$ Gauss; $\gamma_2 = 30$, where M_0 is the maximum column density along the central field line and $B_x(0)$ is the horizontal field in the middle of the thread. The only difference is thus in the parameter γ_1.

The Lyman continuum profiles for these two models are shown in Fig. 1. Here the full lines represent averaged profiles over the width of the thread (profiles seen along the field lines), the dashed lines are mean profiles over the whole length of the thread (seen across the field lines). Double-arrowed lines belong to model $\boldsymbol{C}_1$. The main difference between the Lyman continuum profiles for models $\boldsymbol{A}_1$ and $\boldsymbol{C}_1$ lies in the value of the specific intensity at each wavelength. As is shown in Fig. 1, the specific intensity for model $\boldsymbol{A}_1$ is almost twice as high as for model $\boldsymbol{C}_1$, while the difference between the two directions of view is almost one order of magnitude. For a detailed interpretation of these calculations we further use the contribution functions for a set of wavelengths of the Lyman continuum.

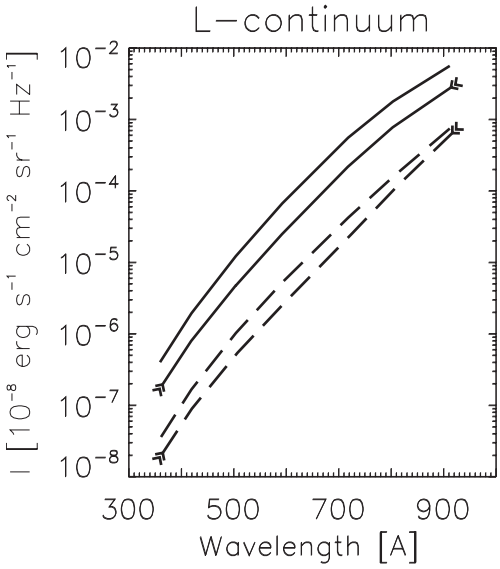

Fig. 1. Lyman continuum for models $\boldsymbol{A}_1$ and $\boldsymbol{C}_1$. Full lines represent averaged profiles over the width of the thread, dashed lines are mean profiles over the whole length of the thread. Double-arrowed lines belong to the model $\boldsymbol{C}_1$.

The description of the contribution-function computation was given in Paper II. We show panels of plots of contribution functions for both models and certain wavelengths with over-plotted contours of temperature and density. The bold dashed contour represents the level of the optical depth of $\tau = 1$ at the selected wavelength. Each plot shows the spatial variation of the contribution to the specific intensity for a given wavelength as a function of the geometrical position. The white regions represent major contributions, the black ones are regions with minor contribution. The panel plots for given wavelengths (Figs. 2–4) are organized as follows: the first four plots are for model $\boldsymbol{A}_1$, the second four for model $\boldsymbol{C}_1$. The upper pair of plots represents viewing along the field lines (*from the left side* in our plots, marked as x-direction according the geometry of the thread), the lower pair represents viewing across the field lines (*from the bottom* in our plots, marked as y-direction). On the left-hand side are the contribution functions over-plotted by iso-lines of the temperature (contours represent 9000, 10 000, 12 000, 15 000, 20 000, 30 000, and 40 000 K starting at the center of the thread). On the right-hand side are the iso-lines of the density for 0.25, 0.5, 1.0, 1.5, 2.0, and 2.5×10^{-13} g cm^{-3} starting at the borders of the thread. Note that these figures are not drawn to the true scale (they are squeezed in the x-direction). We shall now discuss the results of our model calculations (shown in Fig. 1) for wavelengths that lie between the head of the Lyman continuum at 911 Å and the head of the He I continuum at 504 Å.

911 Å

When viewed along the field lines (*from the left side*) the maximum of the contribution function for model $\boldsymbol{A}_1$ is in the region with the temperature between 12 000 and 17 000 K (Fig. 2). The specific intensity of model $\boldsymbol{C}_1$ is formed at slightly lower temperatures (10 000 to 15 000 K) and also at lower densities. Therefore the value of the specific intensity at the wavelength of 911 Å for model $\boldsymbol{A}_1$ is two times higher (6.0×10^{-10} erg s^{-1} cm^{-2} sr^{-1} Hz^{-1}) than for model $\boldsymbol{C}_1$ (3.0×10^{-10} erg s^{-1} cm^{-2} sr^{-1} Hz^{-1}) (see also Fig. 1). In the direction of view across the field lines (*from the bottom*)

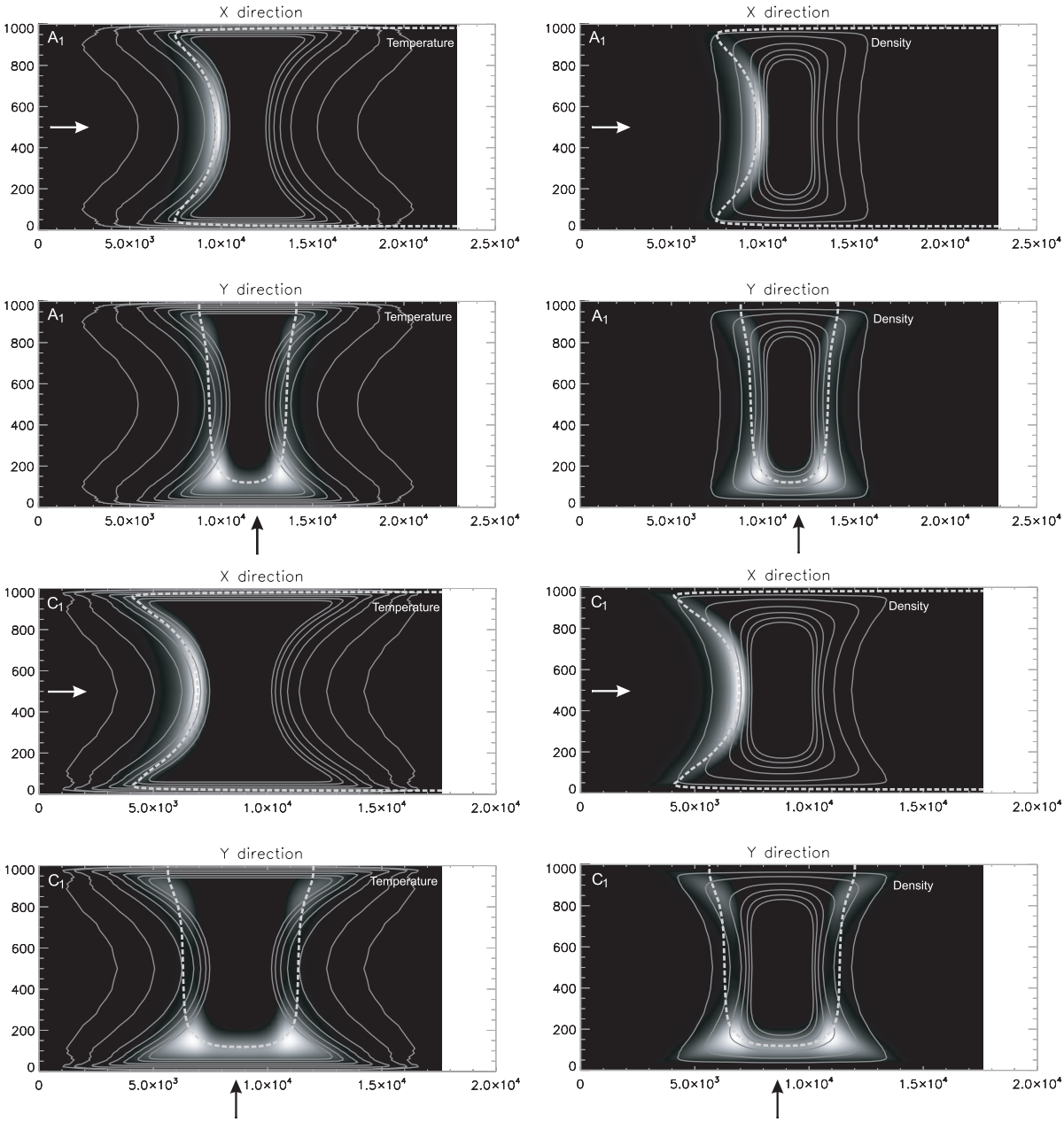

Fig. 2. Contribution function for Lyman continuum at the wavelength 911 Å for models $\boldsymbol{A}_1$ (the first four plots) and model $\boldsymbol{C}_1$ (the second four plots). The upper pair of the plots for each model represents the viewing along the field lines (*from the left side*), the lower pair represents the viewing across the field lines (*from the bottom*). On the left-hand side iso-contours of the temperature (9000, 10 000, 12 000, 15 000, 20 000, 30 000, and 40 000 K) and on the right-hand side iso-contours of the density (0.25, 0.5, 1.0, 1.5, 2.0, and 2.5×10^{-13} g cm^{-3}) are shown. The bold dashed line represents the contour of τ(911 Å) = 1.

the maximum of the contribution function is in the central region with minimal temperature for both models; however, for model $\boldsymbol{A}_1$ this area has a higher density. The value of the specific intensity varies along the length of the thread. In the central cool part it is almost the same for both models, while the maximum of the intensity is twice as high for model $\boldsymbol{A}_1$ as for model $\boldsymbol{C}_1$. The areas with the major contribution correspond to the $\tau = 1$ contour. We also have similar results for the wavelength of 803 Å.

717 Å

For the direction of view along the field lines the specific intensity comes from the region with temperatures from 10 000 up to 20 000 K for model $\boldsymbol{A}_1$ and up to 18 000 K for model $\boldsymbol{C}_1$ with slightly higher density for model $\boldsymbol{A}_1$ (Fig. 3). The specific intensity is again much higher for model $\boldsymbol{A}_1$ (Fig. 1). Viewed across the field lines the place of formation for model $\boldsymbol{A}_1$ is shifted to the same area as for the direction of view along the field. However, across the field lines we see two symmetrical areas of major contribution. The specific intensity of model $\boldsymbol{C}_1$ is partially formed in the central cool part of the thread and partially in the same region as viewed along the field lines. The value of the specific intensity is higher for model $\boldsymbol{A}_1$ everywhere along the length of the thread.

504 Å

For both directions of view the specific intensity is formed at higher temperatures from 15 000 to more than 30 000 K, but

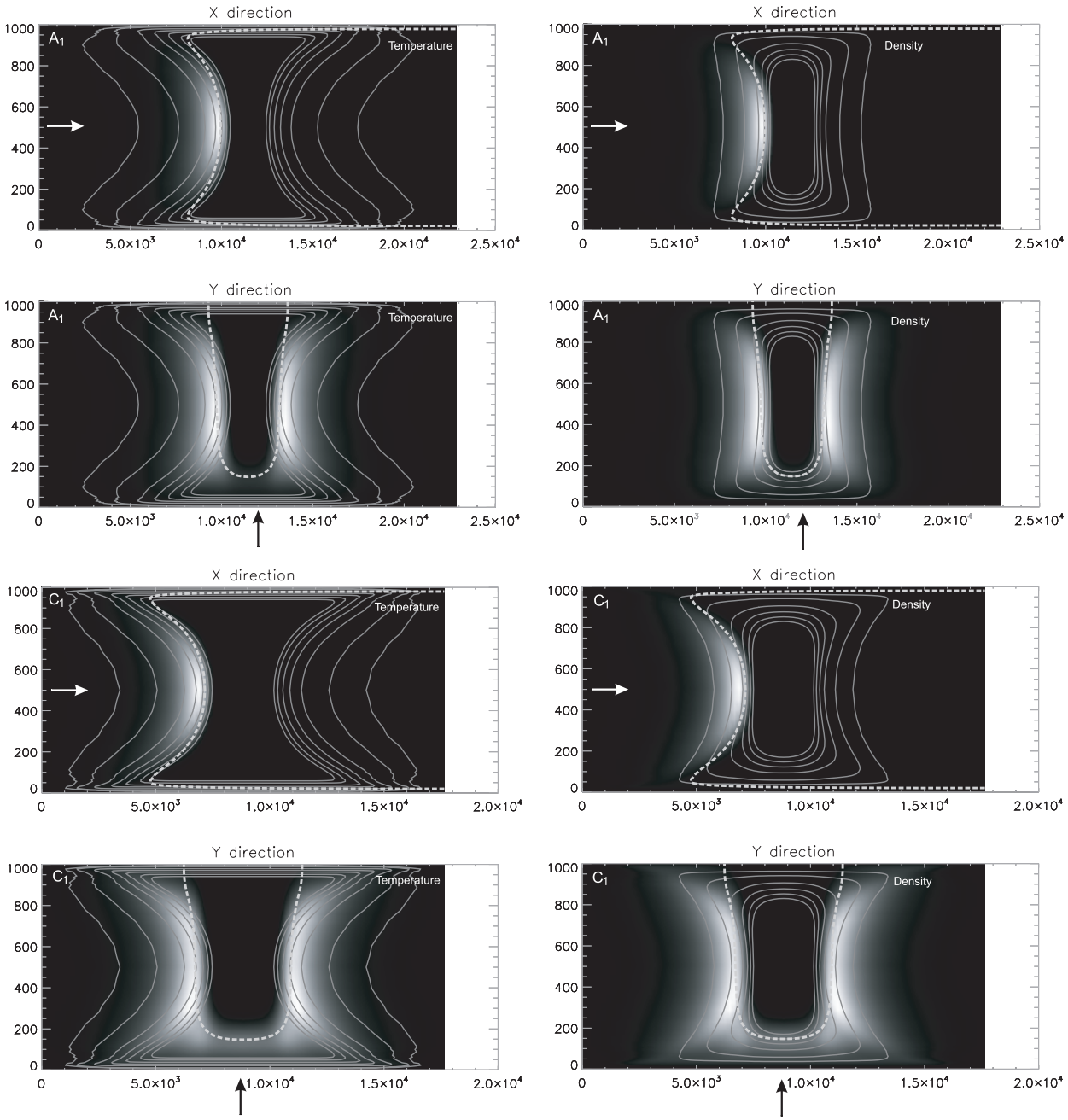

Fig. 3. Same as in Fig. 2 but at the wavelength 717 Å.

the density is higher for model $\boldsymbol{A}_1$ (Fig. 4). Therefore the intensity for model $\boldsymbol{A}_1$ is higher than for model $\boldsymbol{C}_1$ in both directions of view. All contributions come from regions lying in front of the $\tau = 1$ contour because of the insufficient temperature at lower wavelengths of the Lyman continuum in the $\tau = 1$ region. Similar results (assuming pure hydrogen) were also obtained for wavelengths below 504 Å.

The parameter γ_1 prescribes the gradient of the temperature along the field lines. With a lower value of γ_1 we have a smoother increase of temperature from the minimal value $T_0 = 8000$ K to the temperature at the boundary $T_{\rm tr} = 50\,000$ K. This results in higher temperatures and densities in areas where the Lyman continuum for a certain wavelength is formed and thus to higher values of the specific intensity for models with lower values of the exponent γ_1.

4. Effect of the fine structure orientation

The effect of the fine-structure thread orientation with respect to the line-of-sight is given by the shape of the temperature structure, which is characterized by the PCTR as outline in our Sect. 2. To show the difference between Lyman continuum profiles seen along and across the field lines we use model $\boldsymbol{C}_1$. For a detailed analysis the wavelengths of 911 Å and 803 Å are useful since their formation region when seen across the field lines is different from the one viewed along the field in comparison to the lower wavelengths.

In the case that the line-of-sight is oriented along the field lines, the Lyman continuum in the range 911 Å to 803 Å is formed in the PCTR with the temperature gradient described by γ_1 in the area with temperatures from 10 000 to 15 000 K. When seen across the field lines the place of the formation is in

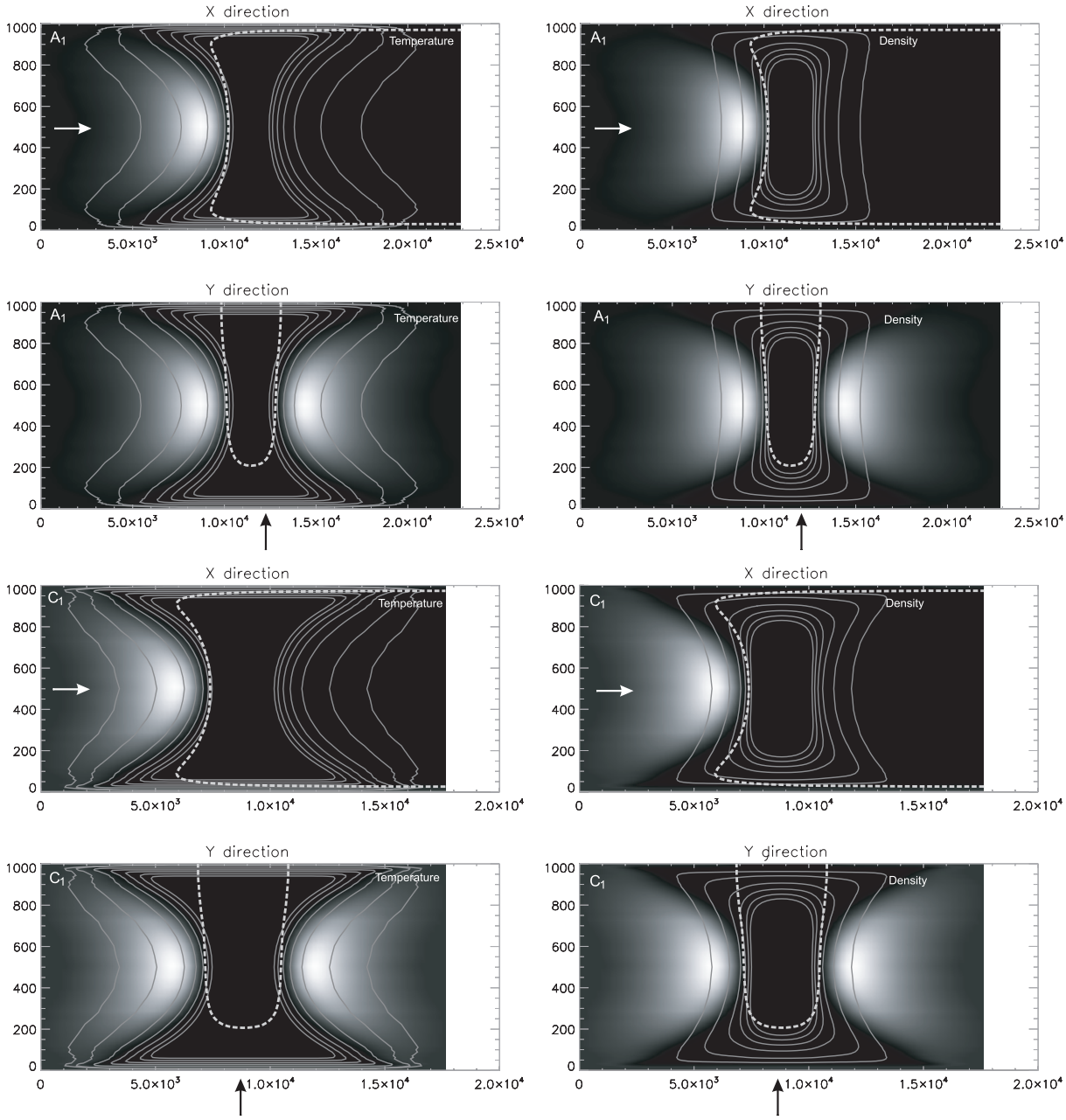

Fig. 4. Same as in Fig. 2 but at the wavelength 504 Å.

the central (coolest) part of the thread. The contribution function for this direction of view has two peaks with an area of minor contribution between them (Fig. 2). Also according to the contribution function, the specific intensity has two peaks at the same position (Fig. 5). The position of the peaks of the specific intensity can be explained by the location of the $\tau = 1$ line. The contribution function follows the $\tau = 1$ line and has a maximum at the places where the $\tau = 1$ line is curved inwards. Thus we see there a bigger contributing region than in the center of the thread.

In the direction of view across the field lines the Lyman continuum is formed at temperatures significantly lower than those seen along the field lines. This is shown also in Fig. 6 where the bold line represents the averaged profile over the width of the thread (profile seen along the field lines), which is formed at a higher temperature than the continuum seen across the field lines. The other lines represent Lyman continuum profiles in different positions along the length of the thread from the center of the thread to the position with the maximum intensity (see Fig. 5). The specific intensity is drawn in logarithmic scale.

5. Discussion and conclusions

This investigation shows that the prominence fine structure can have a very strong influence on the shape of the observed Lyman continuum. There are several aspects that one has to take into account for the interpretation of such spectra. The presence of the PCTR is very important for the emission of the Lyman continuum. A direct comparison of Figs. 2 to 4 shows that for the wavelengths around 911 Å the contribution mainly comes from the innermost parts of the PCTR and also from parts of the cool prominence interior. The location of the emission also strongly depends on the viewing direction with respect to the magnetic field. At 911 and 803 Å, the emission is centered around the

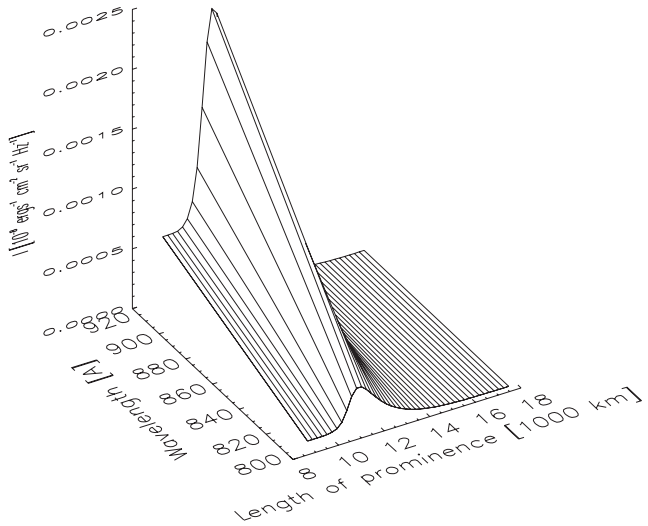

Fig. 5. Lyman continuum intensity variation along the thread for model $\boldsymbol{C}_1$. The plot represents one half of the thread from its center.

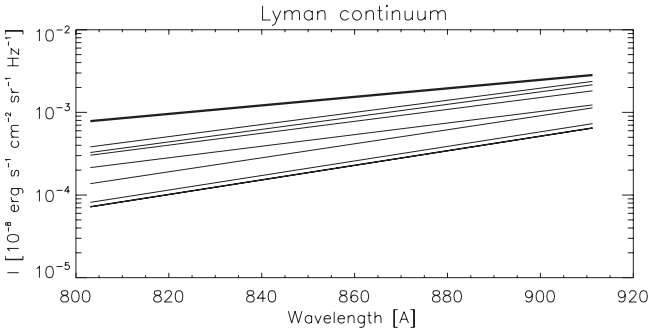

Fig. 6. Lyman continuum for model $\boldsymbol{C}_1$. The bold line represents an averaged profile seen along the field lines. Other lines belong to different positions along the length of the thread (seen across the field) from the center of the thread (the lowest lines) to the peak (the highest lines).

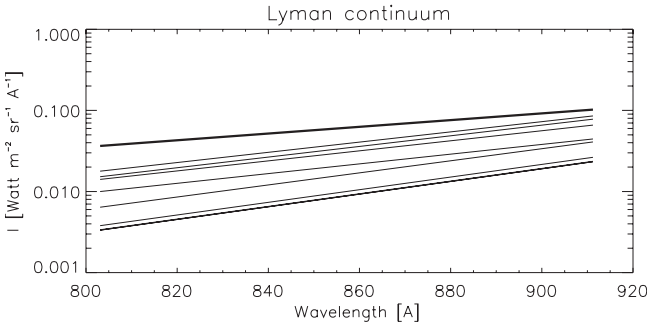

Fig. 7. Same plot as in Fig. 6, but the intensity is expressed in Watt m^{-2} sr^{-1} $Å^{-1}$ for a better comparison with Parenti et al. (2005).

$\tau = 1$ line. At 718 Å, and even more pronounced at 504 Å, the emission basically comes from hotter parts of the PCTR and the region is spatially much more extended. In these cases it comes from regions in front of the $\tau = 1$ line (i.e., optically thin regions). The emergent spectra vary strongly as one moves along the threads (Fig. 5). This effect will make any temperature determination on this basis rather uncertain unless we can reach a very high spatial resolution of individual threads.

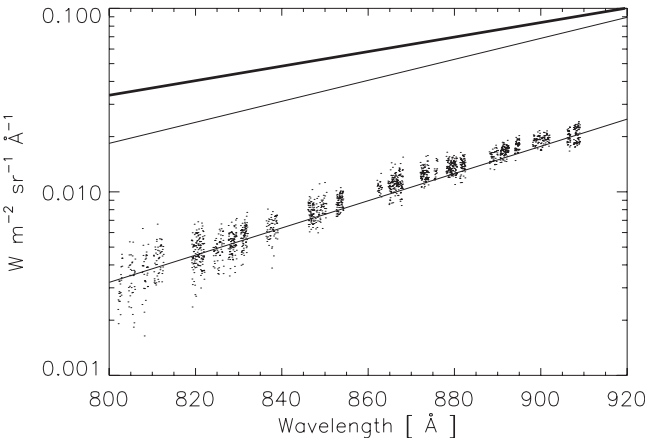

Fig. 8. Intensity of the Lyman continuum (corrected) from part A_1 of the prominence discussed by Parenti et al. (2005). The bold line represents an averaged profile of model $\boldsymbol{C}_1$ seen along the field lines. Other lines belong to different positions of model $\boldsymbol{C}_1$ along the length of the thread (seen across the field).

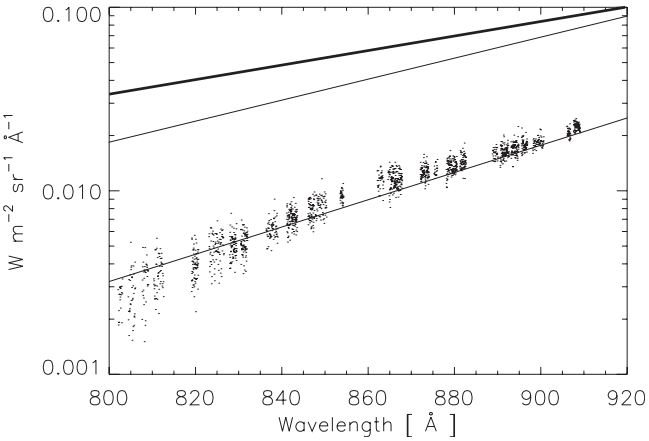

Fig. 9. Same as in Fig. 8, but for part A_2 of the prominence.

The situation is somewhat clearer if one only considers the part of the spectrum between 800 Å and 911 Å, as was done in Parenti et al. (2005). Then the main contributions over this entire spectral range come from approximately the same locations in space. In such a case, it is possible to interpret this spectrum in terms of a mean temperature of the contributing region. But the contributing regions still depend strongly on the viewing direction. From Fig. 2 one sees that the contribution comes from a region with the temperature between 10 000 to 15 000 K when viewed along the field lines (model $\boldsymbol{C}_1$) and from regions with the temperature slightly higher than 8000 K when looking perpendicular to the field lines (see Fig. 7). In the first case one looks at the innermost parts of the PCTR, in the second mainly at the cooler prominence body. Therefore the temperatures derived by making spectral fits to the observations will be strongly dependent on the fine structure and the viewing angle. But in all cases the temperature derived on this basis will lead to upper limits for the true central prominence temperature.

All profiles seen across the field lines (Fig. 7) come from regions with similar temperatures, the only difference is in the *b*-factors (i.e., non-LTE departure coefficients for the ground level of the hydrogen). The lowest profiles with the highest values of the *b*-factors correspond to the very central part of the thread. These profiles represent satisfactory fits to the data from

part A_1 of the prominence discussed by Parenti et al. (2005) (Fig. 8). Their derived temperature (8300 K) is slightly higher than the central temperature that we used in our models. For part A_2 (Fig. 9) they obtained a temperature of 7600 K, which is lower than the minimum temperature of our set of models. Note that Parenti et al. (2005) derived the color temperature from spectra in Figs. 8 and 9 and then assigned it to the kinetic temperature. This is based on previous results of Gouttebroze et al. (1993).

Our computations show that temperatures derived by using the color temperature can be considered as upper limits for the central prominence temperature. This is due to the variation of the *b*-factors along the wavelength, which allows us to make same fit to the spectra in Figs. 8 and 9 with lower temperature. The temperatures determined by Parenti et al. (2005) ranging from 7600 to 8300 K are actually not in conflict with possibly lower values in the central parts.

This paper shows that the Lyman continuum spectrum between 800 Å and 911 Å alone does not give a unique answer about the plasma parameters in prominences. Therefore it will be desirable to analyze simultaneous measurements of this continuum (in a broader wavelength range) together with the detailed spectra of different Lyman lines. This can give more rigorous constraints on the models and therefore will allow one to obtain more reliable estimates of the physical conditions in quiescent prominences.

Acknowledgements. S.G. and P.H. acknowledge the support from the MPA Garching; U.A. thanks for support from the Ondřejov Observatory. This work was done during S.G.'s stay at the MPA Garching supported by the EARA-EST programme and in the frame of grant No. IAA 3003203 of the Grant Agency of the Academy of Sciences of the Czech Republic and ESA-PECS project No. 98030. We thank S. Parenti for providing us with Figs. 8 and 9. SOHO is a space mission of international cooperation between ESA and NASA.

References

Anzer, U., & Heinzel, P. 1999, A&A, 349, 974
Fontenla, J. M., Rovira, M., Vial, J.-C., & Gouttebroze, P. 1996, ApJ, 466, 496
Gouttebroze, P., Heinzel, P., & Vial, J.-C. 1993, A&AS, 99, 513
Gunár, S., Teriaca, L., Heinzel, P., & Schuehle, U. 2006, in Proc. SOHO 17 Conf., ESA-SP, in press
Heinzel, P., & Anzer, U. 2001, A&A, 375, 1082 (Paper I)
Heinzel, P., & Anzer, U. 2005, in Solar Magnetic Phenomena, ed. A. Hanslmeier, A. Veronig, & M. Messerotti, Astron. Astrophys. Space Sci. Lib., 320 (Dordrecht: Springer), 115
Heinzel, P., Anzer, U., & Gunár, S. 2005, A&A, 442, 331 (Paper II)
Heinzel, P., Schmieder, B., & Vial, J. C. 2006, in Proc. SOHO 17 Conf., ESA-SP, in press
Heinzel, P., Schmieder, B., Vial, J. C., & Kotrč, P. 2001, A&A, 370, 281
Labrosse, N., & Gouttebroze, P. 2004, ApJ, 617, 614
Parenti, S., Lemaire, P., & Vial, J.-C. 2005, A&A, 443, 685
Patsourakos, S., & Vial, J.-C. 2002, Sol. Phys., 208, 253
Schmieder, B., Heinzel, P., Kucera, T., & Vial, J.-C. 1998, Sol. Phys., 181, 309
Schmieder, B., Heinzel, P., Vial, J.-C., & Rudawy, P. 1999, Sol. Phys., 189, 109
Schmieder, B., Tziotziou, K., & Heinzel, P. 2003, A&A, 401, 361
Wilhelm, K., Lemaire, P., Curdt, W., et al. 1995, Sol. Phys., 170, 75

Appendix D

Spectral diagnostics of the magnetic field orientation in a prominence observed with SOHO/SUMER

Schmieder, B., Gunár, S., Heinzel, P. & Anzer, U. 2007
Solar Phys., **241**, 53 (SGHA)

Solar Phys (2007) 241: 53–66
DOI 10.1007/s11207-007-0251-5

Spectral Diagnostics of the Magnetic Field Orientation in a Prominence Observed with SOHO/SUMER

B. Schmieder · S. Gunár · P. Heinzel · U. Anzer

Received: 29 June 2006 / Accepted: 19 January 2007 /
Published online: 14 March 2007

Abstract During several campaigns focused on prominences we have obtained coordinated spectral observations from the ground and from space. The SOHO/SUMER spectrometer allows us to observe, among others, the whole Lyman series of hydrogen, while the Hα line was observed by the MSDP spectrograph at the VTT. For the Lyman lines, non-LTE radiative-transfer computations have shown the importance of the optical thickness of the prominence – corona transition region (PCTR) and its relation to the magnetic field orientation for the explanation of the observed line profiles. Moreover, Heinzel, Anzer, and Gunár (2005, *Astron. Astrophys.* **442**, 331) developed a 2D magnetostatic model of prominence fine structures that demonstrates how the shapes of Lyman lines vary, depending on the orientation of the magnetic field with respect to the line of sight. To support this result observationally, we focus here on a round-shaped filament observed during three days as it was crossing the limb. The Lyman profiles observed on the limb are different from day to day. We interpret these differences as being due to the change of orientation of the prominence axis (and therefore the magnetic field direction) with respect to the line of sight. The Lyman lines are more reversed if the line of sight is across the prominence axis as compared to the case when it is aligned along its axis.

Keywords Prominences · Hydrogen Lyman lines · Solar magnetic fields

B. Schmieder (✉)
Observatoire de Paris, Laboratoire d'Etudes Spatiales et d'Instrumentation en Astrophysique, 92195 Meudon Cedex, France
e-mail: brigitte.schmieder@obspm.fr

S. Gunár · P. Heinzel
Astronomical Institute, 25165 Ondrejov, Czech Republic

S. Gunár
Astronomical Institute, Faculty of Mathematics and Physics, Charles University, Prague, Czech Republic

U. Anzer
Max-Planck-Institut f. Astrophysik, Karl-Schwarzschild Str. 1, 85740 Garching, Germany

1. Introduction

Solar prominences consist of cool plasma located in the hot corona and supported against gravity by external forces, either of dynamic or magnetic nature. The dynamic models invoke injection of chromospheric plasma from below. The injection can be produced by thermal instability, leading to dynamic condensation along flux tubes (Poland and Mariska, 1986; Karpen, Antiochos, and Klimchuk, 2006), by Alfvén waves (Lin, 2002) or by reconnection-driven flows (Litvinenko and Martin, 1999).

Magnetic hydrostatic models for quiescent prominences were first proposed in 1D by Kippenhahn and Schlüter (1957) and Kuperus and Raadu (1974). The prominence as a whole is represented by dipped magnetic field lines in a vertical plane. A straightforward generalisation of these models to fine structures can be envisioned as purely local magnetohydrostatic (MHS) equilibria, producing many local magnetic dips everywhere. Such a scenario was first proposed by Poland and Mariska (1988), who considered local magnetic dips due to the cool plasma weight. These dips would propagate vertically to form apparent narrow vertical plasma threads. Heinzel and Anzer (2001) developed this solution of 2D MHS equilibria coupled to non-LTE radiative transfer in two dimensions. In 3D approaches, MHS modelling using linear or nonlinear force-free fields was recently studied by different groups, who showed that prominence fine structures could be mapped by dips of magnetic arcades computed by extrapolation using photospheric magnetograms as boundary conditions (Aulanier and Démoulin, 1998; Aulanier and Schmieder, 2002; van Ballegooijen, 2004; Régnier and Amari, 2004).

The observations of prominences require long exposure times (∼3 times longer than for filaments) and generally it is difficult to distinguish the fine structures even with high-resolution telescopes and thus to define physical quantities of the fine structures, *i.e.* magnetic field, velocity field and optical thickness. However, at the limb it is possible to have good diagnostics to define the orientation of prominence fine threads and their physical parameters.

In this paper we propose two methods to derive the orientation of the magnetic field in prominences. The first one is purely a morphological analysis when the filament is first observed on the disk. The second uses the hydrogen Lyman line series for diagnostics as recently proposed in theoretical work based on the thickness of the prominence – corona transition region (PCTR) (Heinzel and Anzer, 2001; Heinzel, Anzer, and Gunár, 2005).

The thickness of the PCTR is interpreted in terms of the integration along or across the field lines. The reversed profiles were assigned to a prominence viewed across the field lines (narrow PCTR), while the unreversed ones belong to a prominence viewed along field lines where the PCTR is assumed to be much more extended. Therefore, the line profiles should be different for observations of prominences along their axis or perpendicular to it.

The prominence that we choose to use for this study presents a round-shaped structure when observed on the disk. Thus the fine structures of this filaments appear on the limb obviously with different orientations. In Section 2 we present the morphological diagnostics leading to an empirical determination of the orientation of the fine structures and therefore of the magnetic field. In Section 3 the Lyman line profiles observed by SOHO/SUMER (Wilhelm *et al.*, 1995) are presented and discussed in the frame of the theoretical models of Heinzel, Anzer, and Gunár (2005).

We conclude that the results of the two methods are in agreement and thus the Lyman lines are good diagnostics to derive the orientation of the magnetic field and the physical parameters of the fine structures.

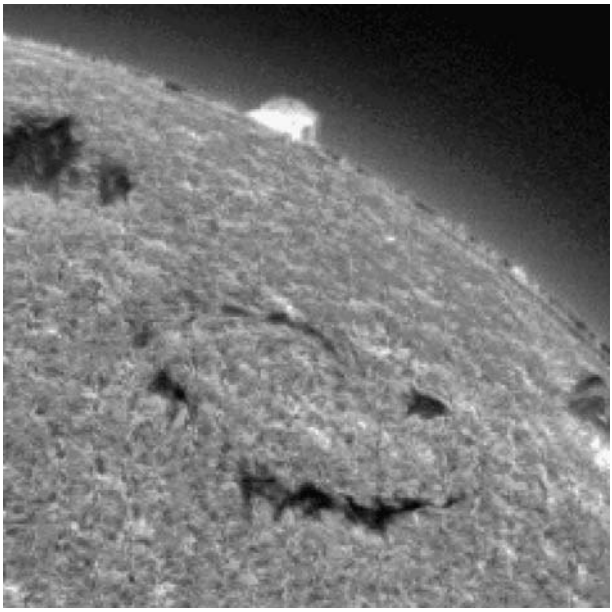

Figure 1 BBSO observation of a round-shaped filament on the disk on October 12, 1999, at 14:04 UT. The field of view is 420 × 420 arcsecs. The orientation of its fine structures indicates that it is a dextral filament.

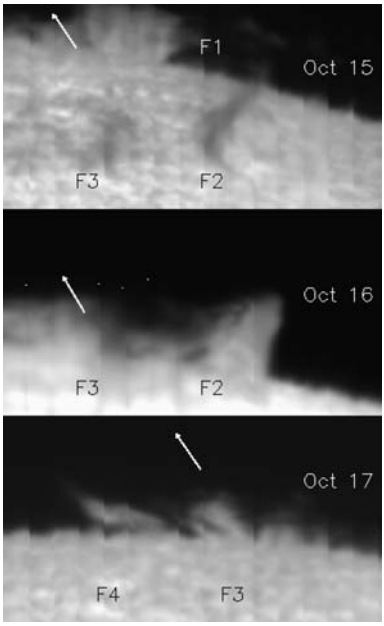

Figure 2 Prominences observed on October 15 at 11:45 UT, on October 16 at 11:37 UT and on October 17, 1999, at 11:37 UT with the MSDP at the VTT. The letters F2, F3 and F4 indicate the latitude positions of different sections of the round filament. On October 15, the sections F2 and F3 are on the disk; they cross the limb on the next day and erupt on October 17. The arrows indicate the North direction and approximately the direction of the SUMER slit. The SUMER slit (120 arcsecs long) crosses the limb and the prominence. The field of view is 228 × 100 arcsecs.

2. Observations of the Filament

2.1. Overview

The filament/prominence used for this study was observed from October 15 to 17, 1999 (N45° – 55°, W50° – 90°), as a target of the MEDOC coordinated campaign between SOHO

and ground-based instruments. A filament with a round shape was observed during three days before crossing the limb (Figure 1). We concentrate our study on the observations obtained mainly with the SUMER spectrometer (Wilhelm *et al.*, 1995) and in addition we used the observations made with the Multi-channel Subtractive Double Pass spectrograph (MSDP) (Mein, 2002) operating on the German solar telescope VTT in Tenerife (Table 1). The VTT has no pointing information; only approximative coordinates can be derived from comparison with synoptic full-disk observations. The VTT observations are presented in Figure 2 and synoptic data in Figure 3. In Meudon spectroheliograms, a SOHO/EIT image at 304 Å and high-contrast spectroheliograms of Big Bear Solar Observatory (BBSO) we see that the round-shaped filament consists of four sections (F1, F2, F3 and F4) that successively cross the limb. The analysis of the filament will allow us to have a 3D view of the fine structures of the prominence.

2.2. Morphological Diagnostics of the Orientation of the Prominence Fine Structures

The fine structures of filaments observed on the disk with high spatial resolution can indicate the orientation angle θ of the horizontal component of the magnetic field versus the filament axis because the magnetic field lines are frozen in the plasma. In our case the round-shaped filament is observed on the disk with survey instruments having a relatively low resolution (Figure 1); therefore, the fine structures are not really visible. We see mainly the barbs and the orientation of their axis, which indicates the chirality of the filament (which is dextral in our case according to the criteria of Martin, 1998) but not really the orientation of the fibrils.

Observationally, the orientation angle of the horizontal magnetic vector with respect to the prominence axis has been statistically measured by Leroy, Bommier, and Sahal-Bréchot (1984). From 256 observed prominences, they found a value of $\theta = -25°$ with a large uncertainty. This uncertainty reflects the dispersion of the 256 measurements, one for each prominence.

A recent study of models based on three-dimensional constant-α (linear) magneto-hydrostatic (MHS) extrapolations of observed photospheric line-of-sight magnetograms gives us new insight on the different characteristics of the magnetic field in prominences (Aulanier and Démoulin, 2003). In particular, it is shown that the θ angle is commonly constant in each prominence and lower than $-20°$ for altitudes larger than few Mm, which correspond to the main body of prominences. On the other hand, at lower altitudes the values of θ may have a larger dispersion. For a given prominence these dispersed values could correspond to fine structures in feet or barbs. In this study we consider mainly the body of the prominence and assume a small θ angle. This seems reasonable in our case. Thus we can deduce the orientation of the prominence versus the line of sight:

- If the main axis of a filament is oriented along a solar meridian (North – South orientation), the fine structures are also more or less oriented along the meridian.
- If the filament axis follows a parallel to the equator, the fine structures are also more or less oriented East – West.
- Viewed at the limb, a filament oriented North – South will appear as an arch, the barbs being the footpoints of the arch. We can say that the line of sight is crossing the magnetic fine structures.
- A filament oriented East – West will appear as a compact prominence, with all its main axis integrated along the line of sight. In that case the line of sight follows the main direction of the magnetic field of the structures.

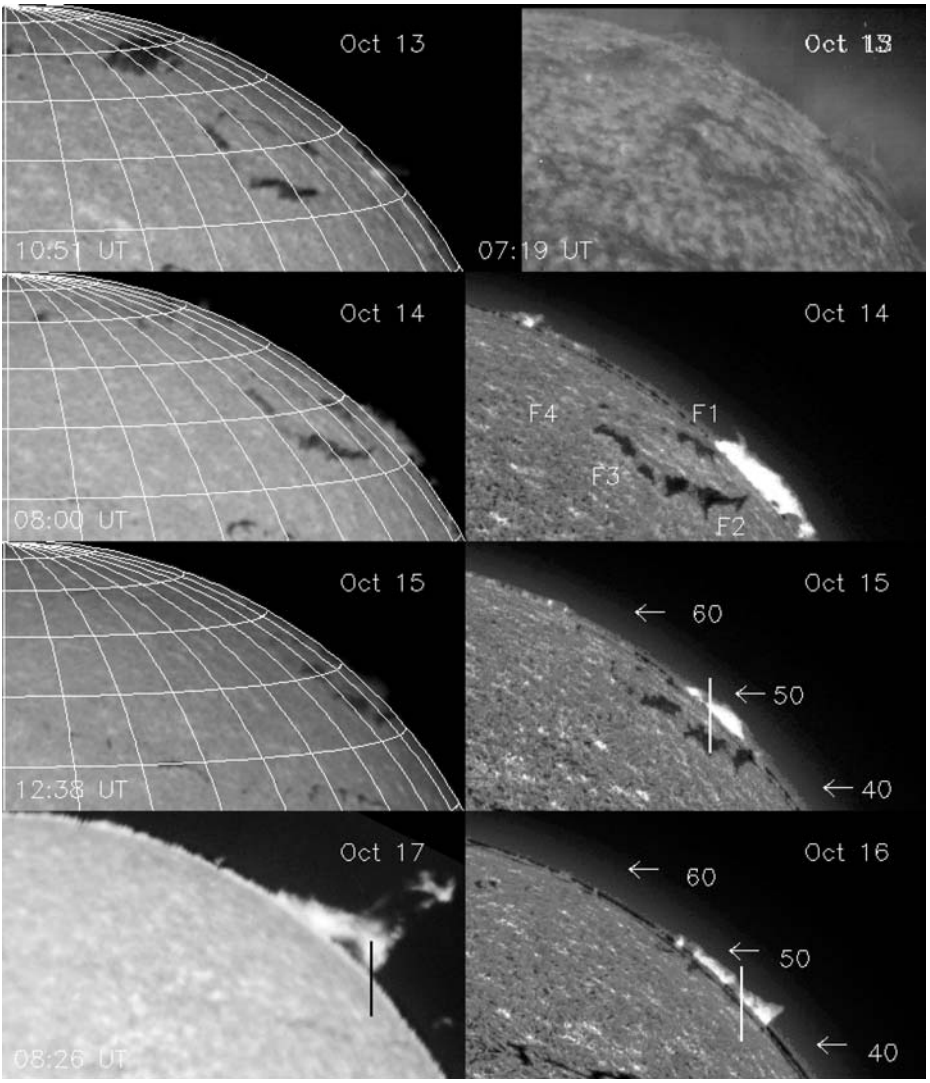

Figure 3 Observations of a round-shaped filament/prominence (F1, F2, F3, F4) from October 13 to October 17, 1999: in the left column, prominence at Meudon Hα spectroheliograms with superposed heliographic coordinates grid for October 13, 14 and 15 (rows 1, 2 and 3); in the right column are presented one observation with SOHO/EIT at 304 Å at 07:19 UT (top panel) and the BBSO observations in Hα obtained around 15 UT. Notice the round-shaped channel in the He II 304 Å EIT image. In the last row, the right panel is the BBSO image for October 16 and the left panel is the Meudon Hα image with the eruptive prominence on October 17 at 08:26 UT. The vertical line in the prominences observed on October 15, 16 and 17 represents the approximate location of the SUMER slit for the time series observations. The arrows, followed by numbers, indicate the latitudes N40°, N50° and N60°.

This discussion allows us to derive from filament observations the orientation of the fine structures versus latitude and longitude and finally versus the line of sight. The round-shaped filament that we have observed during three days consists of several sections (F1, F2, F3 and F4) well visible on October 14 before it crosses the limb (Figure 3). Sections F1 and F3 are

Table 1 Coordinates of the prominence observations with SOHO/SUMER and the VTT telescope. (Column 2: x, y are the coordinates of the centre of the SUMER slit in arcseconds, column 3: their corresponding heliographic latitudes, column 4: times of the observations at the VTT, column 5: intervals of the time series observed with SUMER.)

Date	x, y [arcsecs]	Latitude [degrees]	VTT [UT]	SUMER [UT]
15 Oct	634, 743	N50	11:45, 16:21	13:45 – 15:10
16 Oct	682, 675	N45	11:37, 12:30, 16:30	11:35 – 14:58
17 Oct	654, 716	N48	11:37, 14:30, 16:30	11:31 – 14:54

oriented North – South; Sections F2 and F4 are oriented East – West. The prominence on October 15 is formed by section F1 located at N50° (Figure 3). The line of sight is crossing the fine structures. On October 16 the prominence consists of two sections, with the southern part (located at N45°), section F2, crossing the limb (Figure 3). The fine structures are integrated along the line of sight, which follows more or less the direction of the magnetic field. In contrast, the northern part of the prominence between N50° and N60° is section F3, oriented North – South, and we could expect that the line of sight is perpendicular to the fine structure axis (or the magnetic field direction). This is in agreement with the North – South orientation of the barbs, which are easily visible on October 12 (Figure 1). On October 17 the prominence should correspond to the top of sections F3 and F4. The prominence is eruptive at 08:26 UT (Figure 3), still visible on the VTT observation at 11:37 UT (Figure 2) and gone in the BBSO image at 15:10 UT. The structures should be integrated along the line of sight.

The heliographic coordinates (latitude and longitude) of the different sections of the filament when crossing the limb are extrapolated and for each day we see which section appears as a prominence. We propose an approximate value of the angle ϕ between the line of sight and the fine structures of the different sections as they are observed over the limb by SUMER in order to summarise the previous discussion (Table 2).

This method is empirical and thus uncertain. We have to assume that no drastic changes occur in the filament before crossing the limb and that the fine structures have the same orientation as the filament axis. Even though this looks reasonable for our round-shaped filament it could be still questionable according to recent observations of filaments with high spatial resolution (O. Engvold, private communication). In the next section we present a second diagnostic method to derive the orientation of the prominence based on the shape of the Lyman lines.

3. Lyman Lines

3.1. SUMER Observations

The Joint Observing Program JOP 107 was running using the CDS and SUMER spectrometers. However, in this study we did not use the CDS observations. The main characteristics of the observation sequences with SUMER are presented in Table 3. We will name the Lyman lines as follows: L2 for Lyman β, L3 for Lyman γ, L4 for Lyman δ and so on. SUMER observed time series of the Lyman lines using two wavelength ranges, one centred on L2 and

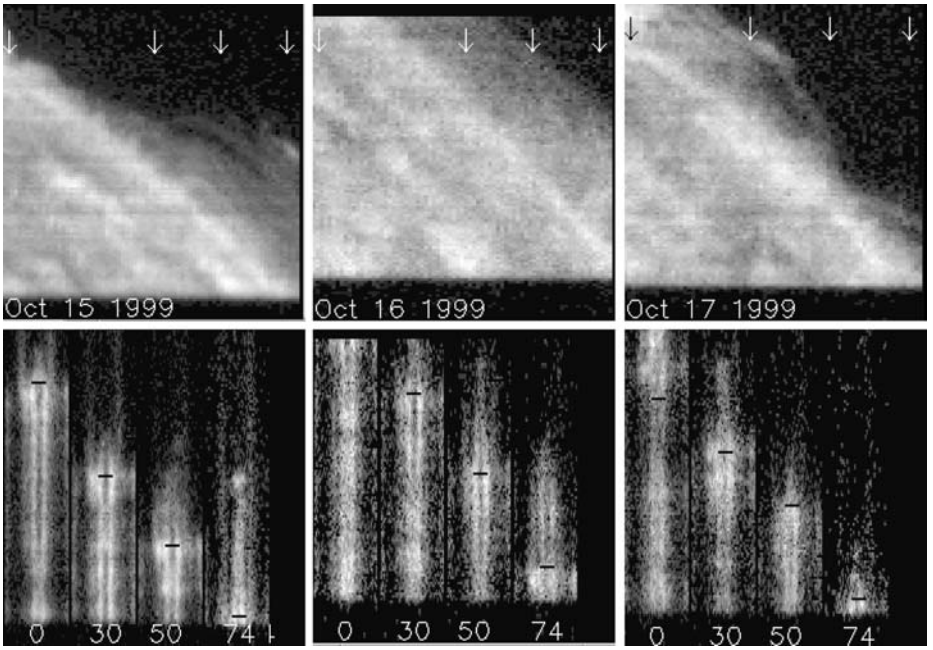

Figure 4 Rasters made with SUMER time series of 76 spectra in the L4 line through the prominences on October 15 at 13:45 UT, October 16 at 11:35 UT and October 17 at 11:31 UT (during 40 min). The field of view of the images is about 114 × 110 arcsecs (approximatively 10 degrees in latitude). Some spectra (110 arcsecs in the *y* direction) are presented below; their positions are indicated by numbers and arrows in the images. The limb is identified by brightenings and is indicated by black horizontal lines over the spectra. Some data are missing at the bottom of the spectra and for October 16 also at the top (black areas). North is up.

Table 2 Heliographic positions in degrees (latitude N and longitude W) of sections F1, F3 and F4 of the filament measured on the grid over the spectroheliograms and then extrapolated as the filament is crossing the limb; ϕ is the approximate value of the angle between the line of sight and the fine structures at the limb derived with the morphological diagnostics. The asterisks indicate the sections observed by SUMER on October 15, 16 and 17, respectively.

Section	Day Latitude	12 W	13 W	14 W	15 W	16 W	17 W	ϕ [degrees]
F1	N50	50	62	75	88*			90°
F2	N45		40 – 55	53 – 70	70 – 80	83 – 93*		0°
F3	N45 – 55	28	40	52	70	83*		90°
F4	N50	28	44	57	68	81	94*	0°

the other one on the higher lines in the series (L4 and L5 to L10). Full spectra (40 Å) were registered for wavelength calibration. Context rasters were performed in the L4 (949.74 Å) and SVI (944.54 Å) lines by scanning the region of the filament/prominence at the beginning and end of the sequences of observations with a step of 1.5 arcsecs covering a field of view of 114 × 120 arcsecs with 76 spectra obtained in 40 min. These two modes were followed

Table 3 Characteristics of the SUMER program (JOP107). The sequence of observations is repeated several times during the observing periods. The program starts and ends with "rastering" the region in L4 and S VI lines (Figure 4); "full spectra" means that 40 Å spectra covering the detector is registered; "7 or 2 lines" means that only 7 or 2 short spectra centred on 7 or 2 lines are registered.

Mode	Lines	Number of windows	Cadence	Exp. time [sec]	Duration [min]	Slit
Raster	L4, S VI	2	76	30	40	4/7
Full spectra	L4 – L10	1	1	127	2	5/8
7 lines	L4 – L7, S VI, O IV	7	16	45	12	5/8
2 lines	L2, O VI	2	2	30	2	5/8
...						
Raster	L4, S VI	2	76	30	40	4/7

by time series of spectra centred on 7 lines or 2 according to the wavelength range (using 7 or 2 windows over the detector to gain time and telemetry space). The observations were performed by using the 1 × 120 arcsec slit (slit 4/5) on October 15 and the 0.3 × 120 arcsec slit (slit 7/8) for October 15, 16 and 17. Slits 4 and 7 are centred on the detector; slits 5 and 8 are positioned in the low part of the detector. In fact 10 pixels in the North – South direction are not available and therefore the size of the images are 115 by 110 arcsecs. Figure 4 shows images of the prominences and parts of the disk obtained from the rastering mode in the L4 line by integrating the line profiles. The limb appears brighter than the disk. The raster frames correspond to a total dimension 114 × 120 arcsecs but because of bad pixels the images are reduced to 114 × 110 arcsecs. Below each raster we present, as examples, four spectra showing large reversed profiles on the disk, similar to filament profiles that we have studied in previous papers, and weak reversed and unreversed profiles for the prominences. Some sections of the spectra in the bottom and at the top are black because of missing data. On October 15, L4 is weak in the prominence and the profile is reversed except in the spectra corresponding to the right side of the raster where the prominence is brighter with some ejected bubbles (spectra 74). On October 16 all the profiles are reversed while on October 17 they are mainly not reversed.

3.2. Lyman Line Profiles

The L2 line spectra for the three days (October 15 – 17) are presented in Figure 5. The location of these spectra corresponds to the central part of the raster in Figure 4. Detached blobs of material are visible from time to time. It is not possible to accurately determine the position of the SUMER slit in the prominence, since the coordinates indicated in the header of the files are not always correct. Besides, the spectra have a curved shape and spatial co-alignment between L2 and L4 spectra needs a shift of 5 pixels in the direction of the slit. L2 gives a different co-alignment than L4. Using the SUMER raster we co-align the L4 observation with the Hα observation obtained with the VTT. Figure 2 shows the prominence observed with the MSDP on the VTT and the arrows indicate roughly the SUMER slit direction. The slit crosses the limb and the prominences. On October 15, the slit of SUMER crosses the F1 fine structures, on October 16, it crosses the F3 fine structures and on October 17 the slit integrates the F3 – F4 structures while the prominence is erupting.

The integrated intensities of the Lyman lines in the prominences are summarised in Table 4; they are relatively low compared with the intensities of the observed prominences

Table 4 Integrated intensities of Lyman lines observed on the disk (disk) and in prominences (prom) in erg/s/cm^2/sr. The pixel number indicates the interval in pixels along the slit where mean prominence profiles were calculated (approximatively 10 to 20 arcsecs long).

Date	Pixels	L2 disk	L2 prom	L4 disk	L4 prom	L5 disk	L5 prom
15 Oct	41 – 50	996	158	140	40	79	17
16 Oct	20 – 30	1194	187	155	33	96	23
	5 – 20	719	159	88	20	66	17
17 Oct	35 – 45	891	164		11	15 – 22	7.4

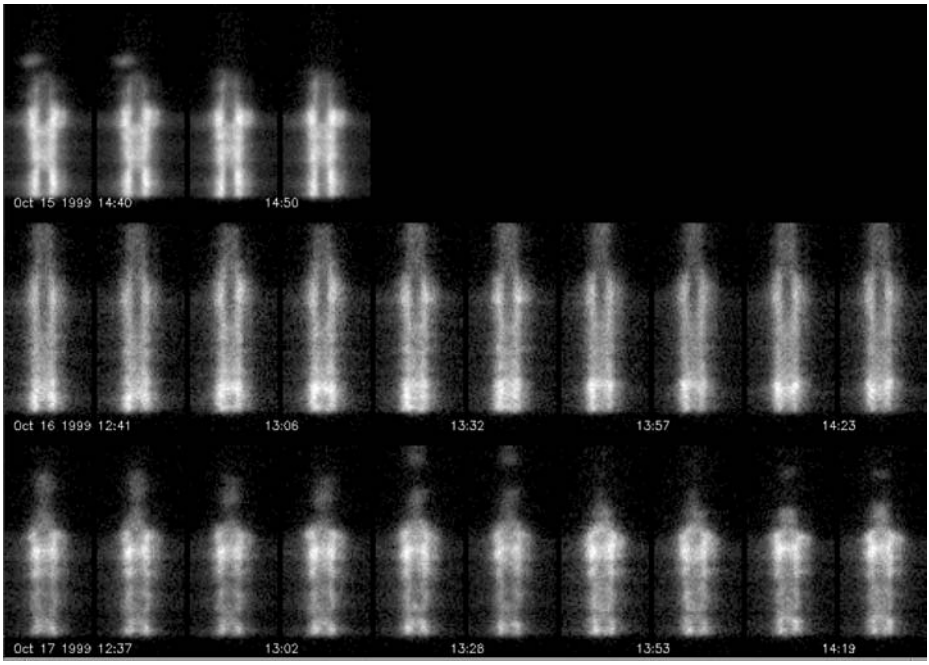

Figure 5 Temporal changes in the spectra of L2 observed partly on the disk and partly in the prominence (the limit between the disk and the prominence can be identified by its increased brightness): top panels on October 15, 1999 (the profiles are strongly reversed; notice a bubble at the top of the prominence with large velocities at 14:40 – 41 UT); middle panels on October 16 between 12:42 and 14:23 UT (the profiles are reversed); bottom panels on October 17 between 12:37 and 14:19 UT. Notice that the profiles are in emission in the prominence and that detached blobs of material are visible from time to time, particularly on October 17, as the prominence is erupting. The profiles on the disk are all reversed; they should correspond to filaments before crossing the limb.

presented by Heinzel *et al.* (2001). This round-shaped filament leads to a rather weak prominence.

Figure 6 shows typical examples of Lyman line profiles (L2, L4, L5, L6 and L7) for the three days. The characteristics of the Lyman lines "reversed or not reversed" depends on the prominence but not on the Lyman line in the series.

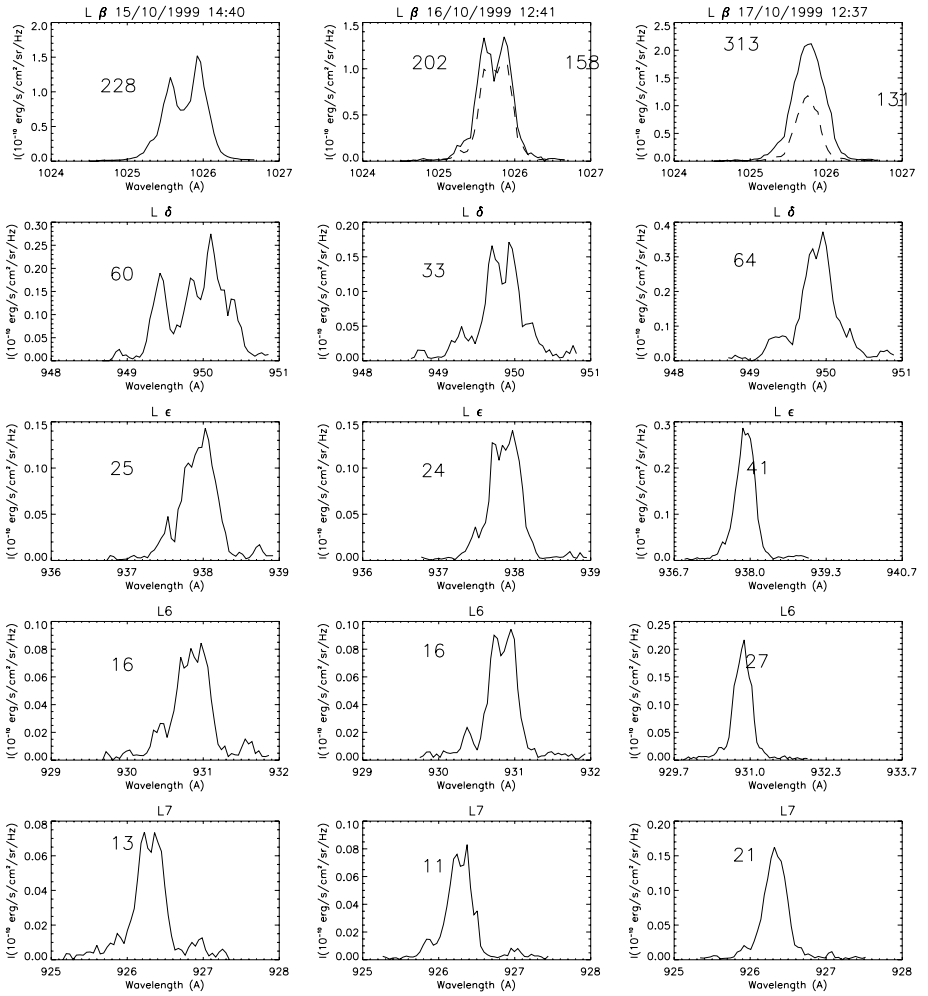

Figure 6 Examples of L2 (Lβ), L4, L5, L6 and L7 profiles in the prominences averaged over a few pixels along the slit to reduce noise (15 to 20 arcsecs) (continuous line) and a blob (dashed line) observed on October 15, 16 and 17, 1999. On October 15 the He II line in the wing of L4 is very strong (a position of the He II line at the edge of the bare part of the detector could explain such an enhancement). The numbers indicated in each panel correspond to the integrated intensity values (in cgs units).

3.3. Theoretical Lyman-Line Profiles

In our previous works (Heinzel, Schmieder, and Vial, 1997; Schmieder *et al.*, 1998; Heinzel *et al.*, 2001; Schmieder, Tziotziou, and Heinzel, 2003) we have demonstrated the importance of the prominence – corona transition region (PCTR) for the formation of hydrogen Lyman lines. In the case of prominences, the SUMER spectra of two different prominences were explained by two quite different PCTRs modelled in a 1D slab geometry (Heinzel *et al.*, 2001). More consistent models of vertical threads with 2D MHS equilibrium in the horizontal plane were recently introduced by Heinzel and Anzer (2001) and Heinzel, Anzer, and Gunár (2005) (see also Heinzel and Anzer, 2006). Multilevel non-LTE

calculations based on such 2D models clearly show that the computed Lyman-line profiles of prominences strongly depend on the viewing angle with respect to the magnetic-field orientation. The field orientation has a two-fold effect on the Lyman-line shapes. First, the density distribution along the field lines is governed by MHS equilibrium, while across the field lines the gas pressure can vary in a rather arbitrary way because the individual flux tubes are magnetically separated. Second, along the field lines the temperature variation is supposed to be relatively smooth because of efficient heat conduction. On the other hand, heat conduction across the field lines is strongly inhibited, which leads to a steep temperature gradient within the corresponding PCTR.

From the grid of 2D models computed by Heinzel, Anzer, and Gunár (2005) one can conclude that the profiles of Lyman lines higher than Lα are much more reversed when we look across the magnetic field lines. This is opposite to the situation when viewing along the field lines where the Lyman lines, and in particular higher series members, are frequently unreversed. A detailed explanation of this behaviour is given in the previously mentioned paper where various examples are shown for 18 different models.

We used this grid of models to compare theoretical Lyman profiles with the observed ones. Our aim was to find models with profiles similar to those we observed and thus qualitatively derive some parameters of the observed prominence (Figure 4). We concentrated on the L4 line profiles from rasters observed on October 16 and October 17 since we can get better averaged profiles with more points in prominences. We have not used the L4 lines from the raster observed on October 15 since they are blended by the He II line. The spectra of the prominences of each day are well characterised with or without reversal (see Section 3.1). Figures 7 and 8 show the variation of the L4 line along the raster. Each profile of surface plots represents an averaged profile along the slit at a given position on the raster, while plots on the right-hand side are averaged profiles over all raster positions. The averaged profiles keep the characteristics of the individual profile of each prominence while reducing noise.

According to our morphological study (Section 2.2), the filament section F3 is observed as a prominence on October 16. The angle ϕ of the line of sight with the fine structure (magnetic field lines) is approximately 90° (Table 2). On October 17 section F4 is observed with the angle between fine structure and line of sight estimated as 0° (Table 2). Reversed profiles correspond to the fine structure observed across the field, while emission profiles correspond to observations along the field lines. This is in agreement with the predictions of Heinzel, Anzer, and Gunár (2005) models.

3.4. Characteristics of the Models

Within the grid of 18 models we have found those with closest agreement between theoretical and observed L4 lines. Figure 9 shows the L4 profiles of models $\boldsymbol{C}_2$ and $\boldsymbol{C}_4$. In one case the profile represents the averaged profile of the central part of the modelled prominence thread seen across the field ($\boldsymbol{C}_2$). The other profile represents averaged profiles over the width of the thread (1000 km) seen along the field lines ($\boldsymbol{C}_4$). Note that synthetic profiles are chosen as best matches from the grid of models.

Figure 10 shows the temperature variation across the field with two thin PCTR regions with a very steep gradient of the temperature, the density variation across the field (along the width of the thread) and the optical depth variation across the field lines at 949.74 Å.

Figure 11 shows the temperature variation along the field lines with two thicker PCTR regions with a gentle gradient of the temperature, the density variation along the field (along the length of the thread) and the optical depth variation across the field lines at 949.74 Å.

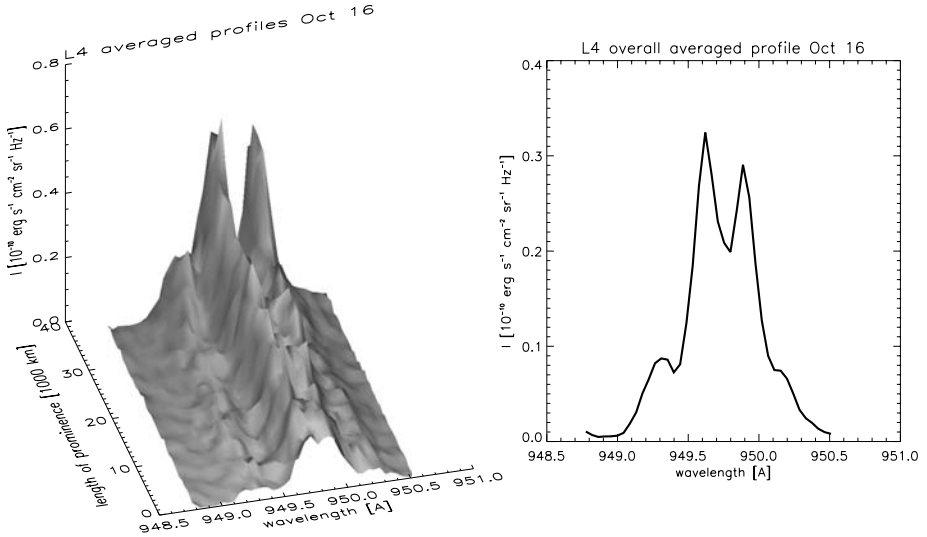

Figure 7 L4 observed on October 16. Surface plot on the left shows the line variation along the raster. Each profile represents an averaged profile along the slit at the given position on the raster. On the right is shown the overall averaged profile along the raster positions.

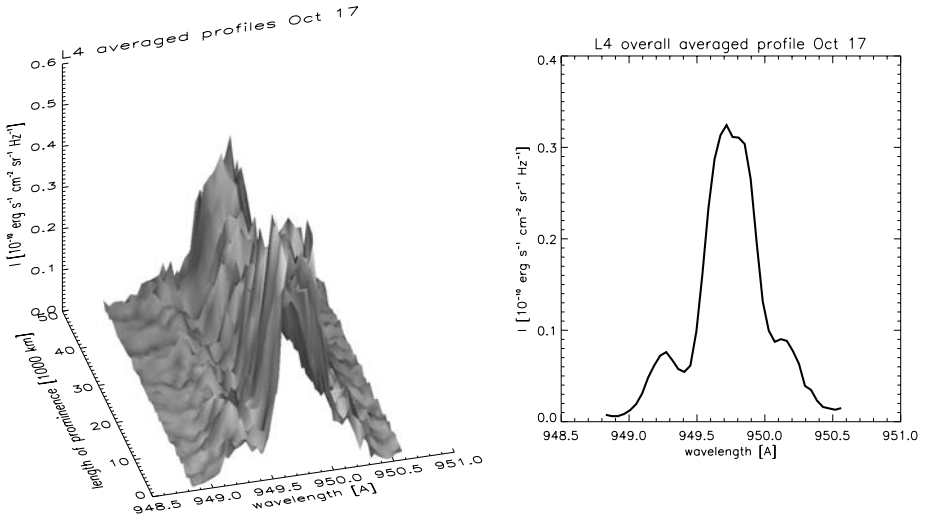

Figure 8 L4 observed on October 17. Surface plot on the left shows the line variation along the raster. Each profile represents an averaged profile along the slit at the given position on the raster. On the right is shown the overall averaged profile along the raster positions.

4. Conclusions

During a MEDOC campaign operated in Orsay, we have observed with the SOHO/SUMER spectrometer a filament crossing the limb on October 15 – 17, 1999. The filament has a

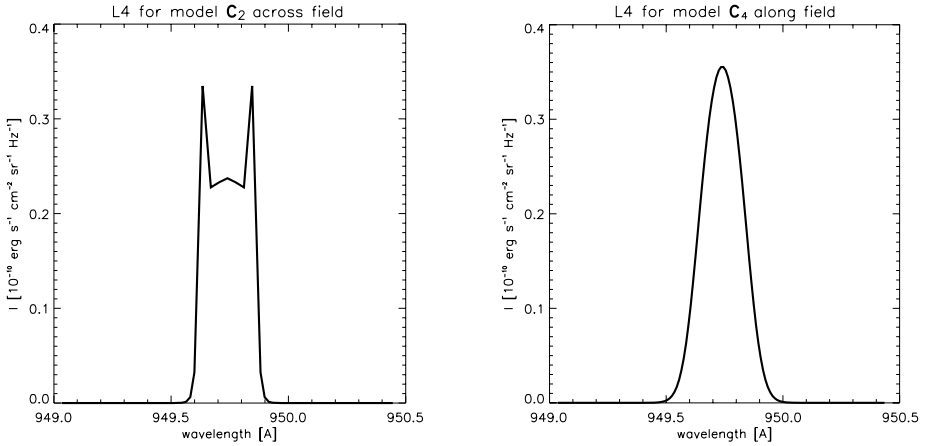

Figure 9 Lyman δ profiles of models $\boldsymbol{C}_2$ (left) and $\boldsymbol{C}_4$ (right).

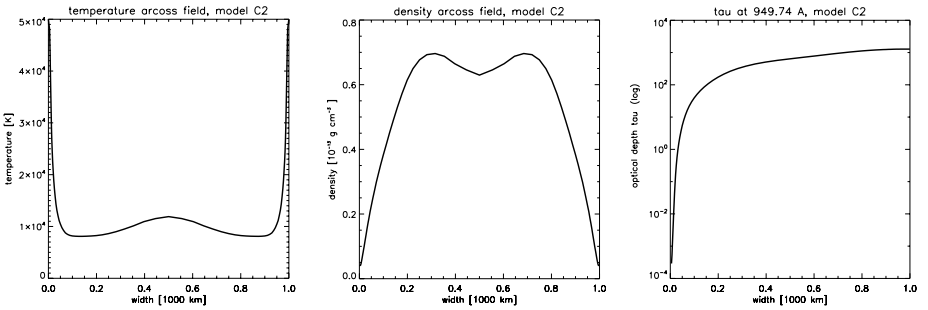

Figure 10 Temperature, density and optical depth variation across the field lines for model $\boldsymbol{C}_2$.

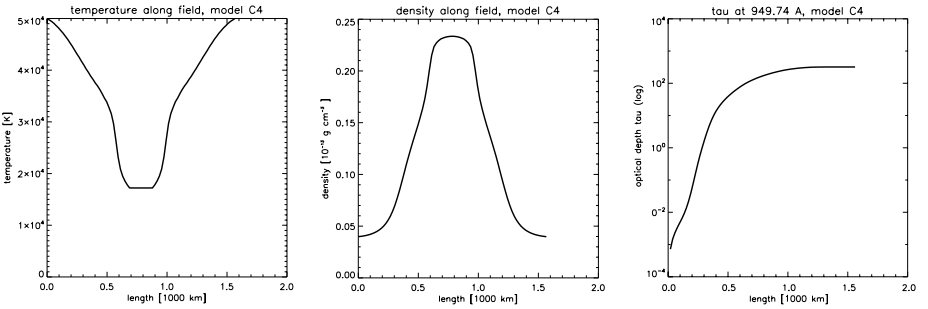

Figure 11 Temperature, density and optical depth variation along the field lines for model $\boldsymbol{C}_4$.

round shape when viewed on the disk and consequently consists of different sections with different orientations. In a first study we use the characteristics of filaments to proceed to a morphological analysis of the different sections and determine the predicted angle between the line of sight and the orientation of the filament, and thus of the magnetic field, as it

crosses the limb and becomes a prominence. In a second part of the work we study the profiles of the Lyman line series observed in the prominences and use the behaviour of the profiles as a diagnostics of the orientation of the magnetic field of the fine structure of the prominences.

The round-shaped filament gives us a unique opportunity to compare the observed Lyman-line profiles (see Figure 6) with theoretical ones. We clearly see how the shape of profiles changes during the subsequent three days when the orientation of the magnetic field with respect to the line of sight is also changed as we derive in this paper. These variations have the same qualitative behaviour as those computed theoretically for 2D thread models. The Lyman lines are more reversed if the line of sight is across the prominence axis as compared to the case when it is aligned along its axis. This result supports the idea that the PCTR can be quite different for different field orientations and that the shape of the Lyman lines provides useful diagnostics for that.

Acknowledgements The authors thank the planners of SOHO instruments during the MEDOC campaign (JOP107). SOHO is an ESA/NASA space mission. This work was done in the framework of the RTN programme (European Solar Magnetism Network, Contract No. HPRN-CT-2002-00313). It was also supported by the ESA-PECS Project No. 98030 and by Grant No. A3003203 of the Grant Agency of the Academy of Sciences of the Czech Republic. BS thanks the Max-Planck-Institut f. Astrophysik and the observatory in Ondřejov for their hospitality during her successive stays. We thank the VTT staff and particularly Dr. Nicole Mein who processed the MSDP data and Dr. Art Poland who read and corrected the manuscript.

References

Aulanier, G., Démoulin, P.: 1998, *Astron. Astrophys.* **329**, 1125.
Aulanier, G., Démoulin, P.: 2003, *Astron. Astrophys.* **402**, 769.
Aulanier, G., Schmieder, B.: 2002, *Astron. Astrophys.* **386**, 1106.
Heinzel, P., Anzer, U.: 2001, *Astron. Astrophys.* **375**, 1082.
Heinzel, P., Anzer, U.: 2006, *Astrophys. J.* **643**, L65.
Heinzel, P., Anzer, U., Gunár, S.: 2005, *Astron. Astrophys.* **442**, 331.
Heinzel, P., Schmieder, B., Vial, J.C.: 1997, *Proc. SOHO 5 Workshop, ESA*, **SP-404**, 427.
Heinzel, P., Schmieder, B., Vial, J.C., Kotrč, P.: 2001, *Astron. Astrophys.* **370**, 281.
Karpen, J.T., Antiochos, S.K., Klimchuk, J.A.: 2006, *Astrophys. J.* **637**, 531.
Kippenhahn, R., Schlüter, A.: 1957, *Z. Astrophys.* **43**, 36.
Kuperus, M., Raadu, M.A.: 1974, *Astron. Astrophys.* **31**, 189.
Leroy, J.L., Bommier, V., Sahal-Bréchot, S.: 1984, *Astron. Astrophys.* **131**, 33.
Lin, Y.: 2002, *Solar Variability: From Core to Outer Frontiers, ESA*, **SP 506**, 681.
Litvinenko, Y.E., Martin, S.F.: 1999, *Solar Phys.* **190**, 45.
Martin, S.F.: 1998, *Solar Phys.* **182**, 107.
Mein, P.: 2002, *Astron. Astrophys.* **381**, 271.
Poland, A.I., Mariska, J.T.: 1986, *Solar Phys.* **104**, 303.
Poland, A.I., Mariska, J.T.: 1988, In: Ballester, J.L., Priest, E.R. (eds.) *Dynamics and Structure of Solar Prominences*, Universitat de les Illes Balears, Palma de Mallorca, p. 133.
Régnier, S., Amari, T.: 2004, *Astron. Astrophys.* **425**, 345.
Schmieder, B., Tziotziou, K., Heinzel, P.: 2003, *Astron. Astrophys.* **401**, 361.
Schmieder, B., Heinzel, P., Kucera, T., Vial, J.C.: 1998, *Solar Phys.* **181**, 309.
van Ballegooijen, A.: 2004, *Astrophys. J.* **612**, 519.
Wilhelm, K., Curdt, W., Marsch, E., *et al.*: 1995, *Solar Phys.* **162**, 189.

Appendix E

Properties of prominence fine-structure threads in a derived from SOHO/SUMER hydrogen Lyman lines

Gunár, S., Heinzel, P., Schmieder, B., Schwartz, P. & Anzer, U. 2007b
Astron. Astrophys. **472**, 929 (GHSSA)

Astronomy & Astrophysics manuscript no. aa7785-07
August 1, 2007

Properties of prominence fine-structure threads derived from SOHO/SUMER hydrogen Lyman lines

S. Gunár[1,2,3], P. Heinzel[1,2], B. Schmieder[4], P. Schwartz[1], and U. Anzer[2]

[1] Astronomical Institute, Academy of Sciences of the Czech Republic, 25165 Ondřejov, Czech Republic
e-mail: [gunar;pheinzel]@asu.cas.cz
[2] Max-Planck-Institut für Astrophysik, Karl-Schwarzschild-Strasse 1, 85740 Garching, Germany
[3] Astronomical Institute, Faculty of Mathematics and Physics, Charles University, Prague, Czech Republic
[4] Observatoire de Paris, Section de Meudon, 92195 Meudon Principal Cedex, France

Received 3 May 2007 / Accepted 8 June 2007

ABSTRACT

Context. The SOHO/SUMER observations provide us for the first time with the prominence spectra in the Lyman-α line outside the attenuator together with the higher members of the hydrogen Lyman series.
Aims. We derive the prominence fine-structure thread properties by comparing the SOHO/SUMER hydrogen Lyman series observations with the synthetic Lyman lines.
Methods. To obtain the synthetic profiles of the Lyman lines, we used 2D prominence fine-structure thread models with a PCTR and consistently solved the 2D non-LTE multilevel radiative transfer. The trial-and-error method was applied to find the model with the best agreement between the synthetic Lyman line profiles and the observed ones.
Results. The properties of the resulting model with the best match of the synthetic and observed line profiles are central (minimum) temperature $T_0 = 7000$ K, maximum column mass in the centre of the thread $M_0 = 1.1 \times 10^{-4}$ g cm^{-2}, horizontal field strength in the middle of the thread $B_x(0) = 6$ Gauss and the boundary pressure $p_0 = 0.015$ dyn cm^{-2}.
Conclusions. The Lyman line profiles observed by SOHO/SUMER can be better reproduced by using multi-thread models consisting of a set of the 2D prominence fine-structure threads placed perpendicularly to the line-of-sight, rather than with the single-thread model.

Key words. Sun: prominences – radiative transfer – line: profiles

1. Introduction

The observations in the hydrogen Lyman lines and in the continuum, represent an important contribution to the understanding of the structure and physical properties of solar prominences. A considerable amount of spectral data in the Lyman lines for quiescent prominences is provided by the SUMER UV-spectrograph (*Solar Ultraviolet Measurements of Emitted Radiation* – Wilhelm et al. 1995) on board the SOHO (*SOlar and Heliospheric Observatory*). Some of these data and their analysis can be found in Schmieder et al. (1998, 1999, 2003, 2007), Heinzel et al. (2001, 2006), Gunár et al. (2006, 2007b) and in a review of SOHO prominence observations by Patsourakos & Vial (2002). Prominence fine structures were recently reviewed by Heinzel (2007).

The formation depths of the Lyman lines and their individual parts (centre, peaks and wings) span the whole structure of the prominence from the centre to the *prominence-corona transition region* (PCTR). Thus their observations represent a significant constraint for prominence modelling. The proper interpretation of the Lyman line observations requires highly sophisticated models with complex non-LTE radiative transfer computations with the PCTR included. Heasley & Mihalas (1976) constructed 1D prominence models in magnetohydrostatic (MHS) equilibrium of the Kippenhahn-Schlüter-type (Kippenhahn & Schlüter 1957) with multi-level non-LTE radiative transfer. The importance of the PCTR for the prominence modelling has been shown by Anzer & Heinzel (1999) and more recently by Labrosse & Gouttebroze (2004). The latter authors concluded that the presence of the PCTR will be required to match the observations with their radiative transfer calculations of the He I triplet lines in a 1D vertical slab model. Heinzel & Anzer (2001) presented prominence fine-structure models in 2D MHS equilibrium (with a PCTR) and consistently solved 2D radiative transfer (for further details see also Heinzel & Anzer 2005). The importance of the 2D modelling for proper interpretation of the SUMER prominence observations was suggested by Heinzel et al. (2001).

A detailed analysis of the observed spectra of two quiescent prominences shows in one case strong unreversed emission profiles of the Lyman lines. The other prominence with a similar brightness in the Lyman spectrum exhibits a significant self-reversal in all observed lines. In order to explain such behaviour, one has to consider different orientations of the magnetic field lines with respect to the line-of-sight. If the prominence fine structure threads are seen from different sides with different shapes of the PCTR this can lead to the observed behaviour. Heinzel et al. (2005) have shown that the Lyman-line profiles are more reversed when seen across the field lines, compared to those seen along the magnetic field. This study, together with Gunár et al. (2007a) devoted to the Lyman continuum, represents an important step towards the understanding of the formation of the Lyman spectrum within solar prominences.

In the present paper we use the same 2D-modelling technique for analysing the SOHO/SUMER observations of the hydrogen Lyman-line series. We were able for the first time to analyse the Lyman-α line together with the higher members of the series. The previous study of the observed Lyman lines (Gunár

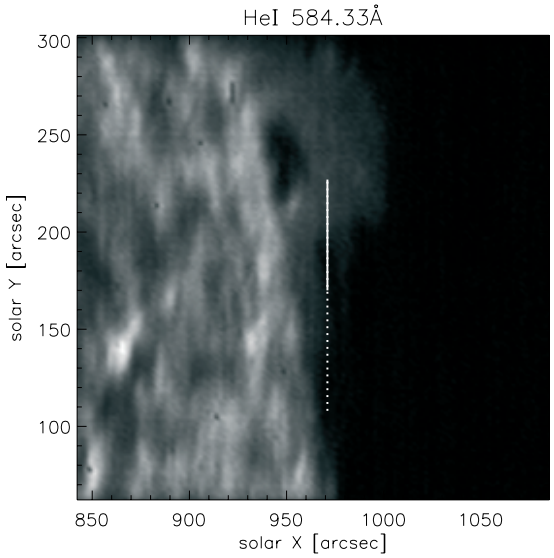

Fig. 1. CDS He I (584.33 Å) line raster with indication of the SUMER slit centred at $X = 972''$ and $Y = 168''$ in SOHO coordinates. The full line represents the part of the SUMER slit which corresponds to the part of the detector A which is still operational.

et al. 2007b) was limited to the Lyman-β to Lyman-δ lines. Other studies concerning the analysis of the SOHO/SUMER observations with the usage of the same 2D modelling are the following: Gunár et al. (2006) devoted to the study of the Lyman-α raster and Schmieder et al. (2007) with a qualitative analysis of the Lyman-δ raster. The opportunity to study the Lyman series observations including the Lyman-α, represents another important step towards the understanding of the physics of the fine-structure prominences.

The paper is organized as follows. Section 2 gives information on the observed prominence, the SUMER spectra and their calibration. Section 3 describes our 2D prominence fine-structure thread model. Section 4 gives the comparison of the observed and synthetic spectra obtained by either single-thread or multi-thread modelling. Finally, Sect. 5 presents the discussion and our conclusions.

2. Observations

The SUMER instrument is a stigmatic spectrograph equipped with two photon-counting detectors (A and B). Both detectors have 1024 spectral columns and 360 spatial rows. Since May 2004 the detector A has been showing a deterioration of the electronics responsible for the readout in the y direction (y-ADC), affecting the spatial (along the slit) information, while the x-ADC is working correctly, leading to correct spectral information.

The present study is based on the spectroscopic observations of the quiescent prominence on May 25, 2005 carried out by SUMER (detector A) during the MEDOC coordinated campaign between SOHO and ground-based instruments (MEDOC campaign No. 15, May 16−29, 2005). The SUMER slit was pointed at solar coordinates $X = 972''$ and $Y = 168''$. The narrower slit 8 ($0.3'' \times 120''$) was used for Lyman-α observations, while for other Lyman lines slit 5 ($1'' \times 120''$) was used. Figure 1 shows the prominence in the He I (584.33 Å) line observed by CDS (*Coronal Diagnostic Spectrometer* – Harrison et al. 1995) on SOHO with the position of the SUMER slit. The full line represents the part of the SUMER slit which corresponds to the part of the detector A which is still operational.

The Lyman series spectral data used in our study were obtained in time steps of approximately two minutes. Lyman-α observations began at 19:10:03 UT, Lyman-β at 19:12:23 UT, Lyman-γ and Lyman-δ at 19:14:32 UT and Lyman-5 to Lyman continuum at 19:16:44 UT. The exposure time of each observation was 115 s. All observed data were not binned during the digitization process in neither a spectral nor in a spatial direction. The dispersion is around 0.044 Å/pixel. The signal-to-noise ratio for the centre of the Lyman-α line reaches 15, for the centre of the Lyman-β line it is around 8, for Lyman-γ line-centre it is around 5 and for the centre of the higher Lyman lines it is below 2.

Calibration and correction of the observed data was done by using standard Solar-Soft procedures (in the following order: dead-time correction, flatfield, local-gain correction and correction for geometrical distortion) to obtain intensities in counts per pixel per sampling interval. Finally, these intensities were converted into physical units using the radiometric calibration. The wavelength calibration was made according to Hansteen et al. (2000) without the correction for shifts of the spectral images on the detector (therefore the wavelength calibration is not absolute). However, the absolute wavelength calibration is not necessary for us because we do not take into account any macroscopic velocities in our modelling. The uncertainties of the intensity measurements depend on the number of photons registered in each pixel during the exposure; the more photons detected in the pixel the higher the signal-to-noise ratio. Using Poisson statistics, the relative error in each pixel is proportional to the reciprocal of the square root of the counts detected in the pixel during the sampling interval (exposure time). All above-mentioned procedures correct the data only to a certain extent. Some instrumental effects as well as additional uncertainties in the radiometric calibration curve for detector A can be still present. The uncertainties in the radiometric calibration curve can be around 15% for wavelengths between 540 and 1250 Å and can rise up to 30% for higher wavelengths (Wilhelm et al. 1999).

The observations of Lyman-α used in our study are the only SUMER Lyman-α observations outside the attenuator. The line profiles of Lyman-α observed on SUMER by using the attenuator are unreliable (see Heinzel et al. 2001) and are thus not useful for the comparison with the synthetic profiles. With respect to the end of the lifetime of the SUMER detectors, observation of the intense Lyman-α line outside the attenuator is now allowed, making realistic Lyman-α profiles obtaining possible.

2.1. Observational data

Each observed spectrum consists of 120 spatial positions along the SUMER slit. From these only pixels 6 to 60 belong to the operational part of the SUMER detector (Fig. 1) and contain useful data. The profiles of each observed Lyman line exhibit rather strong variation along the slit from more intense reversed profiles on the first 30 pixels of the slit to lower emission profiles on another 30 pixels. Figure 2 shows the spectra of the Lyman-α to Lyman-δ lines from pixels 1 to 60. Figure 3 shows the variation of the intensity, integrated over the spectral domain of each line, along the slit for Lyman-α to Lyman-δ lines. The values of the integrated intensity (Fig. 3) in comparison with the values of the integrated intensity from the disk (Heinzel et al. 2001, Table 3) clearly show that the observed data we use belong to the prominence.

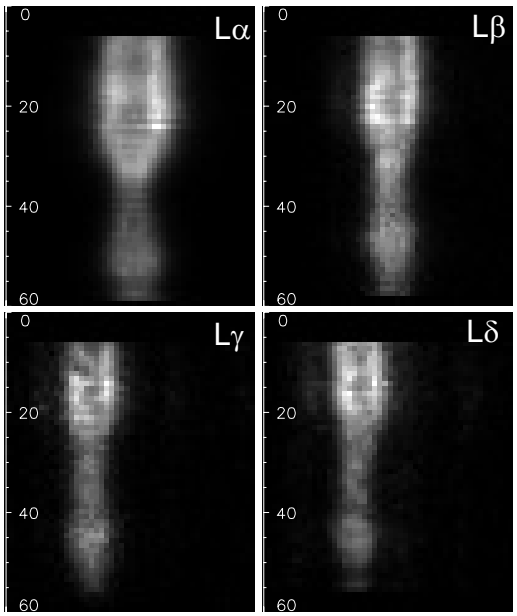

Fig. 2. SUMER spectra for Lyman-α to Lyman-δ lines from pixels 1 to 60.

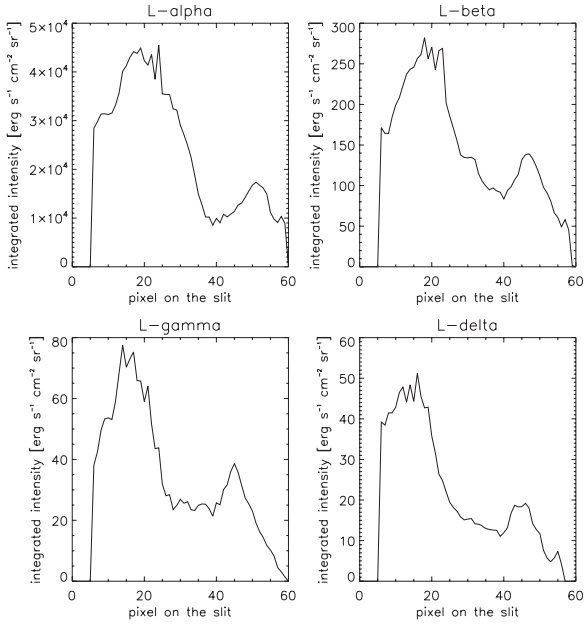

Fig. 3. The variation of the integrated intensity (over the spectral domain of each line) for Lyman-α to Lyman-δ.

In addition, reversed profiles show strong asymmetries of their peaks most probably due to velocity gradients. For the analysis of the Lyman lines by comparison with our synthetic spectra it is necessary to use symmetrical profiles. Such profiles which are almost symmetrical, occur in our observational data in small clustered locations of up to 3 pixels close to each other. An averaging over such an area can help us to avoid errors due to the possible presence of velocity gradients while the spatial resolution remains on the same level as the model resolution. The clusters of pixels with symmetrical profiles for all of the observed Lyman lines, lie between pixel 13 and 18 along the slit as follows:

The Lyman-α profile represents the average over pixels 14 to 17, Lyman-β over pixels 13 and 14, Lyman-γ over 15 to 17, Lyman-δ over 13 to 15, the observed profile of the Lyman-6 represents the profiles from pixel 15 and the Lyman-7 profile represents the average of pixels 15 and 16. The observed data of the Lyman-5 line do not contain useful symmetrical profiles and therefore we cannot use them in this study. The observed profiles of the Lyman lines higher than Lyman-7 contain a noise level which is too high to be useful for our study.

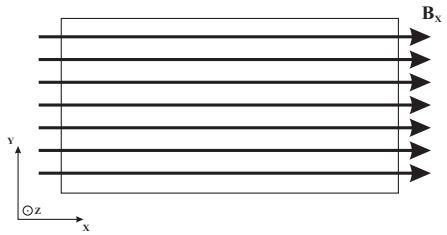

Fig. 4. Sketch of the *x*-*y* horizontal plane with the outlined direction of the horizonal magnetic field B_x.

3. 2D models of the prominence fine structure

In order to obtain the synthetic spectra we use the 2D prominence fine structure models presented by Heinzel & Anzer (2001). The prominence takes the form of a vertically infinite two-dimensional thread hanging in the a horizontal magnetic field. The variation of all quantities takes place in the *x*-*y* horizontal plane (parallel to the solar surface) with the *z*-axis pointing upwards. The thread is uniform along the *z*-axis (Fig. 4). The mathematical formulation of the 2D MHS equilibrium for such fine structure threads is described by Eqs. (2) to (7) of Heinzel & Anzer (2001). Generally, the magnetic field in prominences exhibits a strong shear component (e.g. Bommier et al. 1994). However since the fine structure threads are formed along the magnetic field independently of the shear of the magnetic field with respect to the prominence/filament axis, we do not take the shear component of the field into account. The input parameters for the MHS equilibrium are boundary (coronal) pressure p_0, the intensity of the magnetic field in the middle of the thread $B_x(0)$ and the maximum column mass M_0 which appears in the formula for $M(y)$:

$$M(y) = M_0\left(1 - \left|\frac{y}{\delta}\right|^{\gamma_3}\right), \qquad \text{for} \qquad |y| \le \delta, \tag{1}$$

where 2δ represents the width of the thread (dimension across the field lines) and exponent γ_3 is set to 2 in our models.

The empirically given temperature profile (Heinzel & Anzer 2001) considers two different shapes of the PCTR. Along the field lines (along the length of the thread) the temperature gradually increases from the central coolest part of the prominence thread towards the boundary temperature. In contrast, across the field lines the temperature exhibits a very steep gradient towards the boundary, within a very thin PCTR layer. This is caused by strongly inhibited heat conduction across the magnetic field lines. The temperature profile can thus be expressed as

$$T(m,y) = T_{\rm cen}(y) + [T_{\rm tr} - T_{\rm cen}(y)]\left\{1 - 4\frac{m}{M(y)}\left[1 - \frac{m}{M(y)}\right]\right\}^{\gamma_1}, \tag{2}$$

where $T_{\rm tr}$ represents the temperature at the boundary and the exponent γ_1 is properly chosen to describe the gradual increase of the temperature along the field lines. The column-mass coordinate m characterizes the extension of the thread in the geometrical x direction. $T_{\rm cen}(y)$, is given by

$$T_{\rm cen}(y) = T_{\rm tr} - (T_{\rm tr} - T_0)\left(1 - \left|\frac{y}{\delta}\right|^{\gamma_2}\right), \qquad \text{for} \qquad |y| \le \delta. \tag{3}$$

Here T_0 is the (minimum) central temperature and the exponent γ_2 is chosen to describe the steep temperature gradient across the field lines.

In the formulation of the MHS equilibrium and for the temperature profiles, we used the column-mass coordinate m instead of x which makes the equilibrium equations independent of the assumed temperature profile. The transformation to the x coordinate requires the following integration

$$x = \int_{M(y)/2}^{m} \frac{1}{\rho} \mathrm{d}m' \tag{4}$$

at each value of the coordinate y, where ρ is the density. The relation between p and ρ is given by the equation of state (Heinzel & Anzer 2001) and depends on the ionization-degree structure.

In order to solve the radiative transfer problem, we assume that the thread is uniformly irradiated from all sides by incident solar radiation. For solving the 2D radiative transfer we use the method based on the Accelerated Lambda Iteration (ALI) technique (Auer & Paletou 1994) with the usage of the Short Characteristics (SC) method for obtaining the formal solution along individual rays. A detailed description of the method is given in Heinzel & Anzer (2001). In order to obtain the higher members of the Lyman series we use a 12-level plus continuum hydrogen atom model. The partial redistribution for the Lyman-α and Lyman-β lines is treated as in Heinzel et al. (1987) and in Paletou (1995).

4. Comparison of observed and synthetic spectra

The two-dimensional prominence fine-structure thread models provide us with the possibility to see the thread from different directions and thus with different orientations of the magnetic field (and corresponding PCTRs) with respect to the line-of-sight. As suggested by Heinzel et al. (2001) and shown by Heinzel et al. (2005), synthetic Lyman-line profiles exhibit the self-reversal shape even for higher members of the Lyman series when seen across the field lines. On the other hand, the profiles of the Lyman lines higher than Lyman-α usually have unreversed emission shapes when seen along the field. This is caused by quite different structures of the PCTRs formed across and along the magnetic field. Our observed Lyman spectra show the reversed shapes even for higher lines and therefore we focus our study only on the line-of-sight perpendicular to the magnetic field.

4.1. Resulting fine-structure thread models

Given that we concentrate our investigation on the direction of the line-of-sight perpendicular to the magnetic field we see the prominence thread along its width (in our models the width is 1000 km along the y-direction) with two narrow PCTR regions with very steep gradients of the temperature. As was shown in Heinzel et al. (2005), the Lyman-line profiles show rather significant shape and intensity variations at different positions along the length of the prominence thread. Figure 5 shows the variation of the Lyman-α profiles (half of each line profile is displayed) emerging from different positions along the length of the thread (the position number is indicated on the x-axis, half of the thread is displayed where position 42 corresponds to the centre of the thread). Each of the line profiles is the average profile over three positions with the centre at the position of the resulting profile. Note that the distance between each of the positions is approximately 350 km and the pixel-size of the SUMER is roughly

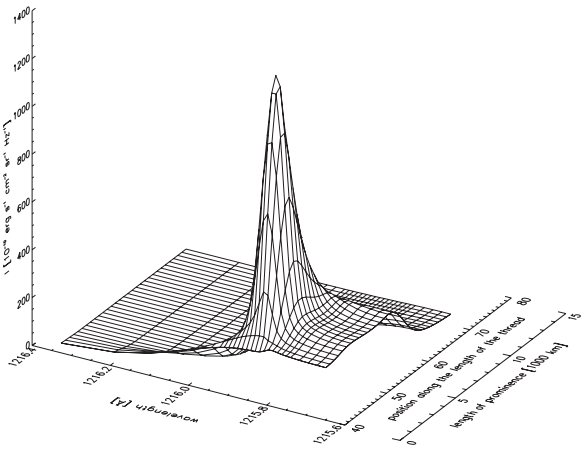

Fig. 5. Emergent Lyman-α intensity variation along the length of the prominence thread. The surface plot shows the half of the Lyman-α profile in different positions along the length of the half of the thread from its centre (centre corresponds to the position 42). Numbers on the x-axis indicate the position along the thread. The second x-axis shows the length of the prominence thread from its centre in 10^3 km.

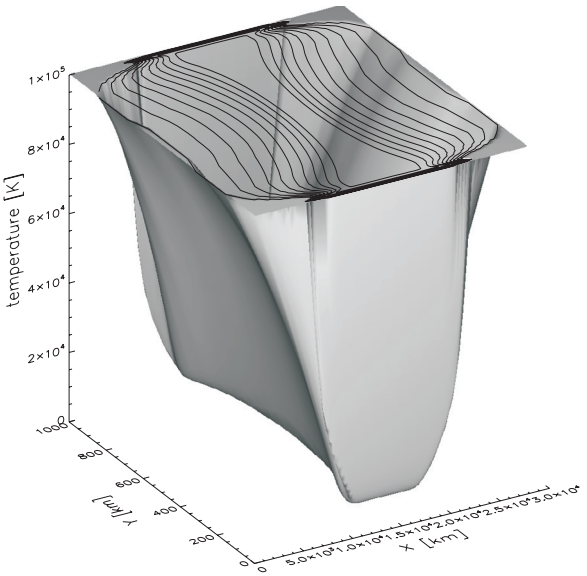

Fig. 6. Variation of the temperature for the resulting prominence thread model. Iso-contours of the temperature range from 10 000 to 100 000 K with steps of 10 000 K.

twice that size. The second x-axis in Fig. 5 shows the geometrical length of the thread from its centre. Thus the x-dimension of the thread is approximately 30 000 km while the y-dimension is 1000 km.

To obtain the model with the best agreement between the observed and synthetic Lyman-line profiles we used a trial-and-error method beginning with the grid of 18 models of Heinzel et al. (2005). By varying the input parameters (i.e. central temperature, central column mass, magnetic field intensity and boundary pressure), and comparing the synthetic profiles emerging from different positions along the length of the thread with the observed line profiles, we identified a model, which is, as far as we can say, unique in the sense that one cannot find any other model in the parameter space which will not lead to a similar agreement between observed and synthetic Lyman-α to Lyman-δ lines. However, it is possible to find a slightly better fit by small variations (in the order of few a percent) of the input parameters

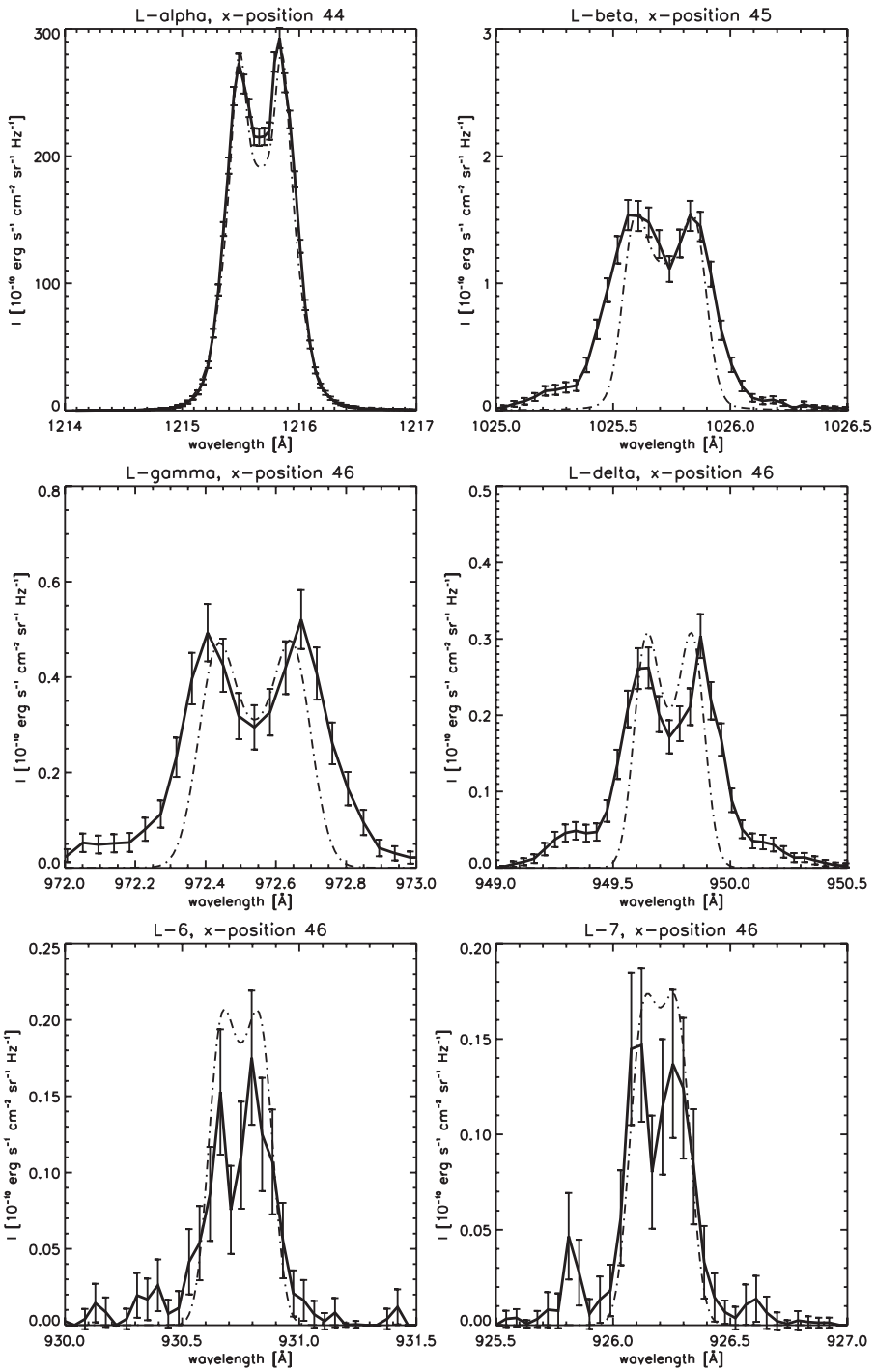

Fig. 7. Comparison between synthetic and observed spectral lines from Lyman-α to Lyman-7. Full lines with overplotted error bars represent the observed data. Dot-dashed lines represent the single-thread model synthetic profiles emerging from the indicated position along the thread.

around the values of the resulting model but such small differences in the shape of the line profiles do not have any influence on our conclusions.

The input parameter values of the resulting model are the central (minimum) temperature $T_0 = 7000$ K, maximum column mass in the centre of the thread $M_0 = 1.1 \times 10^{-4}$ g cm^{-2}, horizontal field strength in the middle of the thread $B_x(0) = 6$ Gauss and the boundary pressure $p_0 = 0.015$ dyn cm^{-2}.

Figure 6 represents the variation of the temperature for the resulting prominence fine-structure thread. The iso-contours of the temperature (ranging from 10 000 to 100 000 K with steps of 10 000 K) show the very steep gradient of the temperature in the y-direction (across the magnetic field) and gradually increasing temperature along the x-direction (along the magnetic field). Note that in Fig. 6 the x-dimension of the thread is approximately 30 000 km while the y-dimension is 1000 km.

4.2. Comparison of single-thread model spectra with observed profiles

The comparison of the observed and synthetic Lyman-α to Lyman-7 lines is shown in Fig. 7, where the full lines with overplotted error bars represent the observed data and the dot-dashed lines represent the synthetic profiles emerging from the indicated positions along the length of the thread. The observed Lyman-α line matches with the synthetic profile emerging from posi-

tion 44, Lyman-β with the profile from position 45 and Lyman-γ and Lyman-δ with the profiles from position 46. Lyman-6 and Lyman-7 are not in agreement with any of the synthetic profiles, however the profiles emerging from position 46 have the closest similarity.

The shift in the positions along the thread from which the profiles are emerging with the best agreement with the observed ones cannot be explained by the time difference between the particular observations (approximately 2 min) and it seems rather nonphysical. A possible explanation of this effect could be the introduction of an inclination between the line-of-sight and the surface of the thread. This has a minor effect on the Lyman-α line profile which, due to its large optical thickness, originates very close to the surface of the thread. However, the importance of this effect is rising with decreasing optical thickness and thus the higher members of the Lyman series are more affected. This can, in general, shift the emerging position of synthetic profiles back to the emerging position of the Lyman-α line. A more detailed description of this effect would need a very extended investigation which is not the purpose of the present study.

Another problem is the width of the synthetic spectral lines which is too small in comparison with the observed ones while the central parts of the lines are in good agreement. Better results can be obtained using the multi-thread modelling described below.

4.3. Multi-thread modelling

Our multi-thread modelling consists of a set of the 2D prominence fine-structure threads placed perpendicularly to the line-of-sight in random positions (Fig. 8). These threads are assumed to be identical. We do not consider any radiative interaction between the threads and thus the distance between them is not important for the results. The total multi-thread model intensity for a given wavelength at any position along the length of the first thread can be described by the formula

$$I_{\rm total} = I_{\rm P_1} + \exp(-\tau_{\rm P_1}) \times I_{\rm P_2} + ... + \exp\left(-\sum_{1}^{N-1} \tau_{\rm P_i}\right) \times I_{\rm P_N} \qquad (5)$$

where $I_{\rm P_1}$ represents the intensity from the given position on the first thread. The thread i ($i > 1$) is randomly shifted with respect to the first thread, $\rm P_i$ represents the position along the length of the thread i which is on the same line-of-sight as the given position on the first thread and $I_{\rm P_i}$ represents the intensity emerging from position $\rm P_i$. $\tau_{\rm P_1}$ is the optical depth at the given position along the first thread and $\tau_{\rm P_i}$ ($i > 1$) represents the optical depth at the position $\rm P_i$ along the thread i. N represents the total number of the threads. Note that in the 1D case the multi-thread fine structure is modeled by a series of parallel planes which are uniform along the length and thus have the same properties at every position ($\rm P_i$) (e.g. Fontenla et al. 1996).

For our study we have considered the first plus 9 additional randomly placed threads each representing the same basic model which has been described previously. The random distributions of the threads produce different emerging profiles for different arrangements of the threads. Figure 9 shows the results of the multi-thread modelling for Lyman-α to Lyman-7 (except Lyman-5). The full lines with overplotted error bars represent the observed profiles. The gray full lines show the one hundred randomly arranged multi-thread models and the dot-dashed lines are the profiles emerging from the first thread only. The position along the first thread is marked in the title of each plot. The area within the gray profiles covers the range of all emerging profiles.

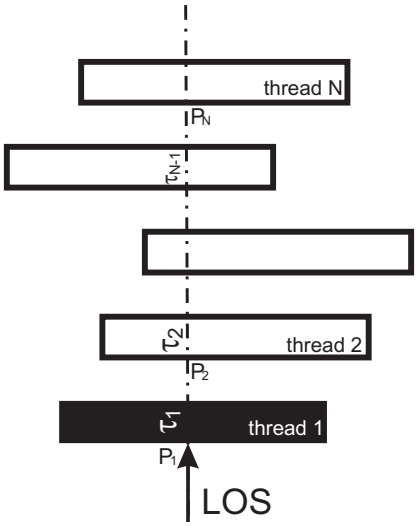

Fig. 8. Scheme of the model with randomly arranged threads. LOS is the line-of-sight. For other quantities see the text.

The Lyman-α line is not strongly affected by the multi-thread modelling and the line profile has almost the same shape as the profile obtained by the single-thread model (except for the slightly wider far wings). The same effect takes place for each position close to the centre of the thread (at position 42).

The shape of the Lyman-β line is however significantly changing with different arrangements of the threads. Here we plot the profiles emerging from position 44 instead of position 45 which was shown in Fig. 7, because at position 44 the observed profile is within the probability region of the multi-thread model profiles. At position 45 the observed profile is on the lower edge of the probability area. The line-wings are significantly wider than the line-wings of the single-thread model. On the left side of the Lyman-β line there is a blending line of He II (1025.27 Å).

The effect of the multi-thread modelling on Lyman-γ and Lyman-δ line profiles is the same as on the Lyman-β line. It means that the profiles are significantly different from the single-thread profile with higher peaks and wider wings. The observed profiles are within the probability area at position 45. The far wings are again blended by He II (972.12 Å and 949.36 Å) on the left side of the Lyman lines and by O I (973.24 Å and 950.11 Å) on the right side.

The Lyman-6 and Lyman-7 lines at position 44 show much better agreement for the multi-thread probability area than with the single-thread profiles emerging from position 46.

5. Discussion and conclusions

The present study shows that prominence Lyman lines observed by the SUMER spectrograph can be better reproduced using multi-thread modelling than with single-thread models. As shown in Fig. 9 the width of the synthetic profiles is significantly larger and thus in better agreement than the width of the single-thread model. With multi-thread modelling we are able to reproduce even higher lines of the Lyman series which is not possible considering only a single prominence fine-structure thread. In addition, the shift of the emerging positions of the synthetic profiles with the best agreement with the observed ones is not as large as it is for the single-thread model. The modelling can be further improved by the introduction of the angle between the line-of-sight and the thread surface which can be different from

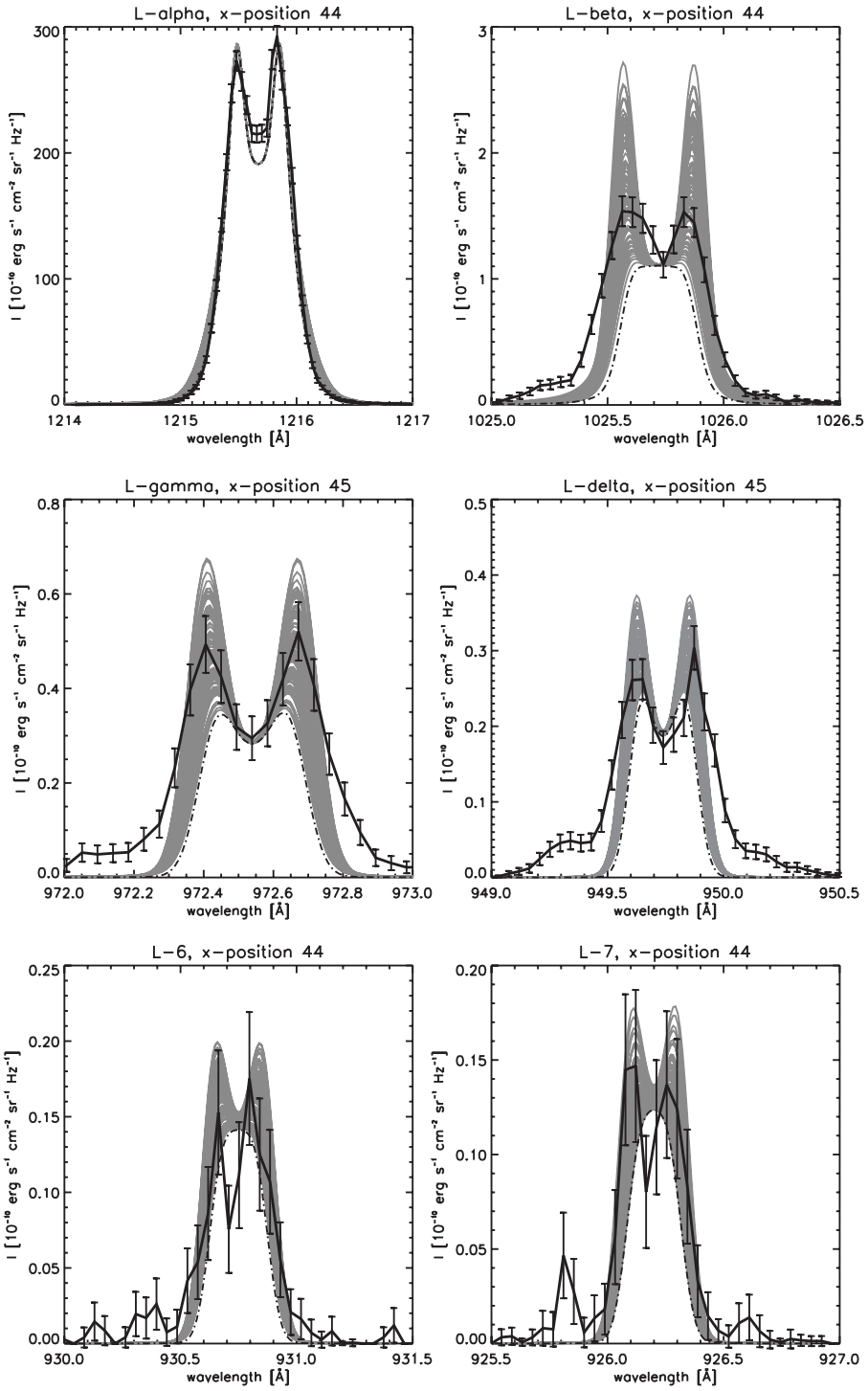

Fig. 9. Comparison between the synthetic and the observed spectral lines Lyman-α to Lyman-7. Full lines with overplotted error bars represent the observed profiles. Gray full lines belong to the one hundred randomly arranged multi-thread models and the dot-dashed lines are the profiles emerging from the first thread from the position which is marked in the title of each plot.

the perpendicular direction. The observations of the filaments on the disk show a number of the fine-structure thread-like features which are on the limb projected along the line-of-sight and thus further support the importance of the multi-thread modelling.

The multi-thread modelling with randomly arranged threads allows us to see the probable shape of the synthetic profiles and thus we are able to deduce the position along the thread with the emerging profile which gives the best agreement with the observations. In order to find the particular arrangement of the threads with the best match with the observed line profiles one has to perform an extensive investigation of all of the possible thread arrangements with different total numbers of threads. The total number of threads can be estimated by the value of the summed column mass of these threads along the line-of-sight. The total column mass of ten threads we have used in our study is of the order of 1.0×10^{-4} g cm^{-2} which is in agreement with the values determined from observations by Anzer & Heinzel (1998).

The Lyman-α line profile is not affected by multi-thread modelling (the resulting emerging profiles from multi-thread models are practically identical with the single-thread profile) and thus it is suitable for search for the best prominence fine-structure thread model, which is afterwards used in the multi-thread modelling.

The possibility to reproduce simultaneously all of the Lyman-α to Lyman-7 lines gives us good opportunity to determine in detail the physical properties of the prominence fine structure.

A more precise determination of the arrangements and the total number of the fine-structure threads requires an extended study of all possibilities of the arrangements of the threads in the multi-thread modelling as well as the inclusion of the radiative interaction between individual threads. We shall investigate this complex behaviour in our next paper.

Acknowledgements. S.G. and P.H. acknowledge the support from the MPA Garching; U.A. thanks for support from the Ondřejov Observatory. This work was done during S.G.'s stay at the MPA Garching supported by the EARA-EST programme and ESA-PECS project No. 98030. S.G. and P.S. acknowledge the support from the grant GA ČR 205/07/1100. SOHO is a space mission of international cooperation between ESA and NASA.

References

Anzer, U., & Heinzel, P. 1998, Sol. Phys., 179, 75
Auer, L. H., & Paletou, F. 1994, A&A, 285, 675
Fontenla, J. M., Rovira, M., Vial, J.-C., & Gouttebroze, P. 1996, ApJ, 466, 496
Bommier, V., Landi degl'Innocenti, E., Leroy, J.-L., & Sahal-Brechot, S. 1994, Sol. Phys., 154, 231
Gunár, S., Teriaca, L., Heinzel, P., & Schuehle, U. 2006, in SOHO 17 – 10 Years of SOHO and Beyond, ed. H. Lacoste, ESA SP-617
Gunár, S., Heinzel, P., & Anzer, U. 2007a, A&A, 463, 737
Gunár, S., Heinzel, P., Schmieder, B., & Anzer, U. 2007b, in The Physics of Chromospheric Plasmas, ed. P. Heinzel, I. Dorotovic, & R. J. Rutten, ASP, 368, 317
Hansteen, V. H., Betta, R., & Carlsson, M. 2000, A&A, 360, 742
Harrison, R. A., Sawyer, E. C., Carter, M. K., et al. 1995, Sol. Phys., 162, 233
Heasley, J. N., & Mihalas, D. 1976, ApJ, 205, 273
Heinzel, P. 2007, in The Physics of Chromospheric Plasmas, ed. P. Heinzel, I. Dorotovic, & R. J. Rutten, ASP, 368, 271
Heinzel, P., & Anzer, U. 2001, A&A, 375, 1082
Heinzel, P., & Anzer, U. 2005, in Solar Magnetic Phenomena, ed. A. Hanslmeier, A. Veronig, & M. Messerotti, Astron. Astrophys. Space Sci. Lib. 320 (Dordrecht: Springer), 115
Heinzel, P., Gouttebroze, P., & Vial, J.-C. 1987, A&A, 183, 351
Heinzel, P., Anzer, U., & Gunár, S. 2005, A&A, 442, 331
Heinzel, P., Schmieder, B., & Vial, J. C. 2006, in SOHO 17 – 10 Years of SOHO and Beyond, ed. H. Lacoste, ESA SP-617
Heinzel, P., Schmieder, B., Vial, J. C., & Kotrč, P. 2001, A&A, 370, 281
Kippenhahn, R., & Schlüter, A. 1957, Z. Astrophys., 43, 36
Labrosse, N., & Gouttebroze, P. 2004, ApJ, 617, 614
Paletou, F. 1995, A&A, 302, 587
Patsourakos, S., & Vial, J.-C. 2002, Sol. Phys., 208, 253
Schmieder, B., Tziotziou, K., & Heinzel, P. 2003, A&A, 401, 361
Schmieder, S., Gunár, S., Heinzel, P., & Anzer, U. 2007, Sol. Phys., 241, 53
Schmieder, B., Heinzel, P., Kucera, T., & Vial, J.-C. 1998, Sol. Phys., 181, 309
Schmieder, B., Heinzel, P., Vial, J.-C., & Rudawy, P. 1999, Sol. Phys., 189, 109
Wilhelm, K., Lemaire, P., Curdt, W., et al. 1995, Sol. Phys., 170, 75
Wilhelm, K., Woods, T. N., Schuehle, U., et al. 1999, A&A, 352, 321